-IEE-

# Conférence Internationale sur l'Ingénierie de l'Environnement et l'Ecologie

## Proceedings of Engineering & Technology -PET-

**Editor : Dr. Ahmed Rhif (Tunisia)**

# CNPSI

Centre National de la Promotion Scientifique et de L'innovation

## Conférence Internationale sur l'Ingénierie de l'Environnement et l'Ecologie

### Proceedings of Engineering & Technology -PET-

Editor : Dr. Ahmed Rhif (Tunisia)

# Committees

## Scientific Committees

Atanas Lazarov

Ahmed Rhif

Ali Akbar Jalali

Anna Belyaeva

Anna Ólafsdóttir

Arnaud Bournel

A. Sargolzaei

Abhilasha Gaur

Abdul Kadir Ozcan

Anand Rajavat

Ankit Chaudhary

Belkacem Sait

Belgin Emre Turkay

Barbara Bis

Baharesh Safaei K

Brajesh Kumar Kaushik

Chang-Hua Lien

Caroline Desa

Djamila Rekioua Ziani

Esin Can

G. Darmani

H. Ramezanpour

H.V. Ramakrishnan

Ille Gebeshuber

Jin-Cherng Lin

Jian Yuan

Khaled Sailan

Massato Oguchi

Madeleine Du Toit

Marwa Ezzat

Mohammad H.Sobhani

Moon Ho Lee

Rita Cucchiara

Rajni Garg

Said Grouni

Silaiman Khalifa Yakhlef

Xu Chen

# Summary

# Effective removal of cytostatic drugs paclitaxel (PCX) from wastewater using clays-based geopolymer : synthesis, characterization and batch adsorption study

Assia Ben Amor[1,2]*, Julia Martín[5] , Marina Arenas[5], Abdelkader Ouakouak[3,4], Wafa Najar[2],Imen Amri[1], Abir Taher [1,2],Noureddine Hamdi[1,2]

[1]*Higher Institute of Water Sciences and Techniques, University of Gabès, Zrig 6072, Tunisia.*

[2]*Laboratory of Composite Materials and Clay Minerals, CNRSM, Technopole Borj Cedria, PO box 73, Soliman 8027, Tunisia.*

[3] *Hydraulic and Civil Engineering Department, University of El-Oued, PO Box 789, El Oued, 39000, Algeria.*

[4]*Research Laboratory in Subterranean and Surface Hydraulics, University of Biskra, PO Box 145, Biskra, 07000, Algeria.*

[5]*Departamento de Química Analítica, Escuela Politécnica Superior, Universidad de 13 Sevilla. E-41011 Seville, Spain.*

*assia.benamor123@gmail.com (*Corresponding author)*

## Introduction :

- The use of cytostatic drugs in chemotherapy has been steadily increasing, raising significant environmental concerns (Heath et al., 2020; Zhang et al., 2013).

- The current levels of these compounds in water do not pose an immediate danger, long-term exposure to PCX can result in toxic effects by interfering with DNA function (Elersek et al., 2016; Isidori et al., 2016).

-  Addressing the removal of these hazardous pollutant from hospital and effluent wastewater before they enter aquatic ecosystems is a pressing and complex challenge.

- Adsorption has emerged as a highly effective method for treating contaminated water due to the widespread availability and selective nature of adsorbents, as well as its simplicity and cost-effectiveness.

- This research explores the potential of a geopolymer developed from illito-kaolinitic clay sourced from the Douiret region of Tunisia, combined with industrial waste materials such as silica fume and phosphogypsum, for decontaminating water samples containing the cytostatic drug paclitaxel (PCX).

- The geopolymer is thoroughly characterized before and after the adsorption process using techniques such as X-ray diffraction, Fourier transform infrared analysis, scanning electron microscopy, and surface area (BET).

## Résultats :

- Adsorption batch assays were conducted, varying PCX concentrations, contact times, and environmental conditions.

- The geopolymer demonstrated exceptional removal efficiency, achieving nearly 100% PCX removal with 20 mg of adsorbent and a drug concentration of 2.5 mg/L.

- Notably, the geopolymer exhibited a specific surface area of 82.23 m2/g and a pore volume of 0.19 cm3/g.

-The adsorption study revealed that the PSO kinetic model and Freundlich isotherm model offered the most accurate description of the adsorption behavior

- In addition to its cost-effective attributes, the geopolymer exhibited outstanding effectiveness in decontaminating various natural water samples, including influent, effluent wastewater, and surface water.
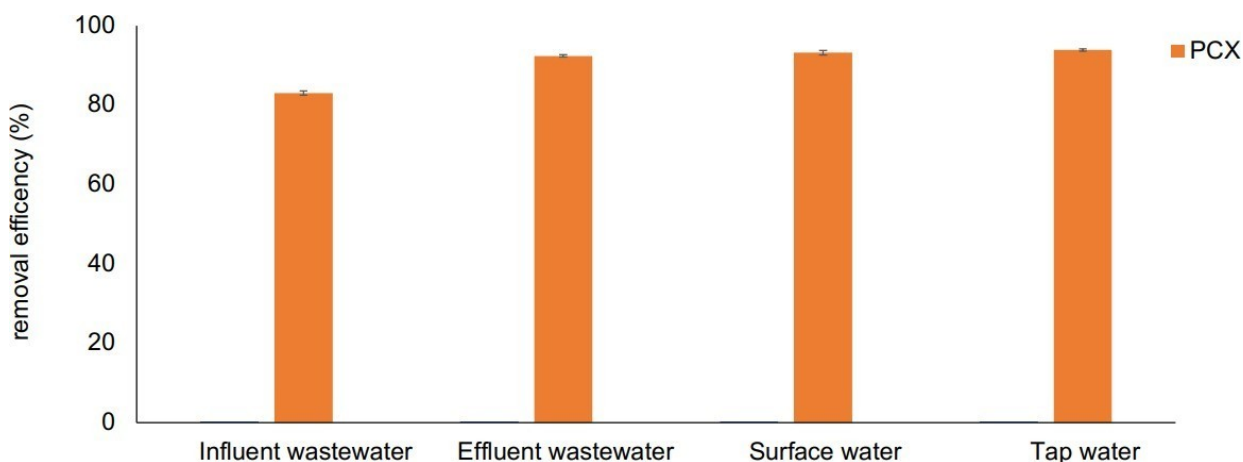


**Figure.** Adsorption percentage (%)PCX by geopolymer in real environmental aquatic samples.

## Conclusion :

- The geopolymer derived from illito-kaolinitic clay shows significant potential in decontaminating water containing the cytostatic drug paclitaxel.

-Its features, including its affordable cost, high specific surface area, and effectiveness across different types of water samples, make it a sustainable solution for purifying water contaminated with cytostatic drugs.

-This approach provides promising prospects for mitigating the environmental impact of cytostatic drugs in aquatic ecosystems.

## References:

-Elersek, T., Milavec, S., Korosec, M., Brezovsek, P., Negreira, N., Zonja, B., de Alda, M.L., Barceló, D., Heath, E., Scancar, J., Filipic, M., 2016. Toxicity of the mixture of selected antineoplastic drugs against aquatic primary producers. Environ. Sci. Pollut. Res 23(15), 14780–14790.

-Heath, E., Isidori, M., Kosjek, T., Filipic, M., (Eds.). *Fate and Effects of Anticancer Drugs in the Environment.* © Springer Nature Switzerland AG 2020.

-Isidori, M., Lavorgna, M., Russo, C., Kundi, M., Zegura, B., Novak, M., Filipic, M., Misik, M., Knasmueller, S., de Alda, M.L., Barcelo, D., Zonja, B., Cesen, M., Scancar, J., Kosjek, T., Heath, E., 2016. Chemical and toxicological characterisation of anticancer drugs in hospital and municipal wastewaters from Slovenia and Spain. Environ. Pollut. 219, 275–287.

-Zhang, J., Chang, V.W.C., Giannis, A., Wang, J.Y., 2013. Removal of cytostatic drugs from aquatic environment: a review. Sci. Total Environ. 445–446, 281–298.

# Use low-cost bio-adsorbents to remove colorants, pharmaceuticals and heavy metals

Djellouli Amir[1,3,4], Berredjem Yamina[2], Hattab Zhour[2,] Guesmia Hadjer[3], Mehenni mokthar[3]

[1]*Université mohammed chérif mesaadia de Souk-Ahras, Algeria*

[2]*Badji Mokhtar-Annaba University, Algeria.*

[3]*Center for Scientific and Technical Research on Arid regions CRSTRA, Biskra, 07000, Algeria*

[4]*Laboratory of Physics of Matter and Radiation (LPMR)*

a.djellouli@univ-soukahras.dz
ORCID :0000-0001-5092-2212

*Abstract*— **The synthesis and production of biomaterials of the cationic and anionic types was the main goal of this investigation. These substances were employed as adsorbents in waters contaminated by various adsorbates that were probably found in the surrounding area. Several approaches (IRTF, DRX, MEB, BET, and ATG/DTA) will be used to characterize the various materials. The adsorption tests using these materials will be conducted by adjusting several parameters, including pH, mass, concentration, and temperature.**

**Elimination of effluents in aqueous media, with a focus on the adsorption technique, which appears to be particularly well-suited to remove pollutants due to its shown effectiveness and cost-effectiveness in using inexpensive adsorbents like industrial and agricultural wastes.**

*Keywords*— **Adsorption, bio adsorbents, water treatment, various materials, and characterization**

I.   INTRODUCTION

One of the biggest issues facing our environment today is the degradation of aquatic ecosystems by different organic and inorganic pollutants. The primary techniques for treating water rely on physical techniques for transferring materials, such as condensation, adsorption, and absorption. The textile business releases a lot of colours, heavy metals, and prescription drugs into the environment. Adsorption of organic and inorganic micropollutants. Because adsorption uses inexpensive adsorbents like industrial and agricultural waste, it is a technology that has been shown to be successful in removing pollutants. It is also a financially sound choice.

Unlock the potential of biochar, a carbon-rich material produced through the pyrolysis process. Learn how it enhances soil fertility and mitigates climate change. Explore various biomass sources, such as wood chips or agricultural waste, to find the ideal material for biochar production. Explore the critical need for efficient plant waste management. Discover how turning waste into biochar can reduce greenhouse gas emissions and promote sustainability.

**Pyrolysis Process**
Uncover the science behind pyrolysis, the thermal decomposition process used to transform plant biomass into biochar.

**Types of Plant Waste**
Explore the diverse range of plant waste, such as agricultural residues and wood chips, that can be transformed into high-quality biochar.



| Textural properties | Unit | Value |
|---|---|---|
| $S_{BET}$ | $m^2/g$ | 727.5 |
| $S_{Micropore}$ | $m^2/g$ | 510.20 |
| $S_{External}$ | $m^2/g$ | 217.3 |
| $V_{Total}$ | $cm^3/g$ | 0.358 |
| $V_{micropore}$ | $cm^3/g$ | 0.156 |
| $V_{Mesopore}$ | % | 56.4 |
| Average pore diameter | nm | 1.97 |
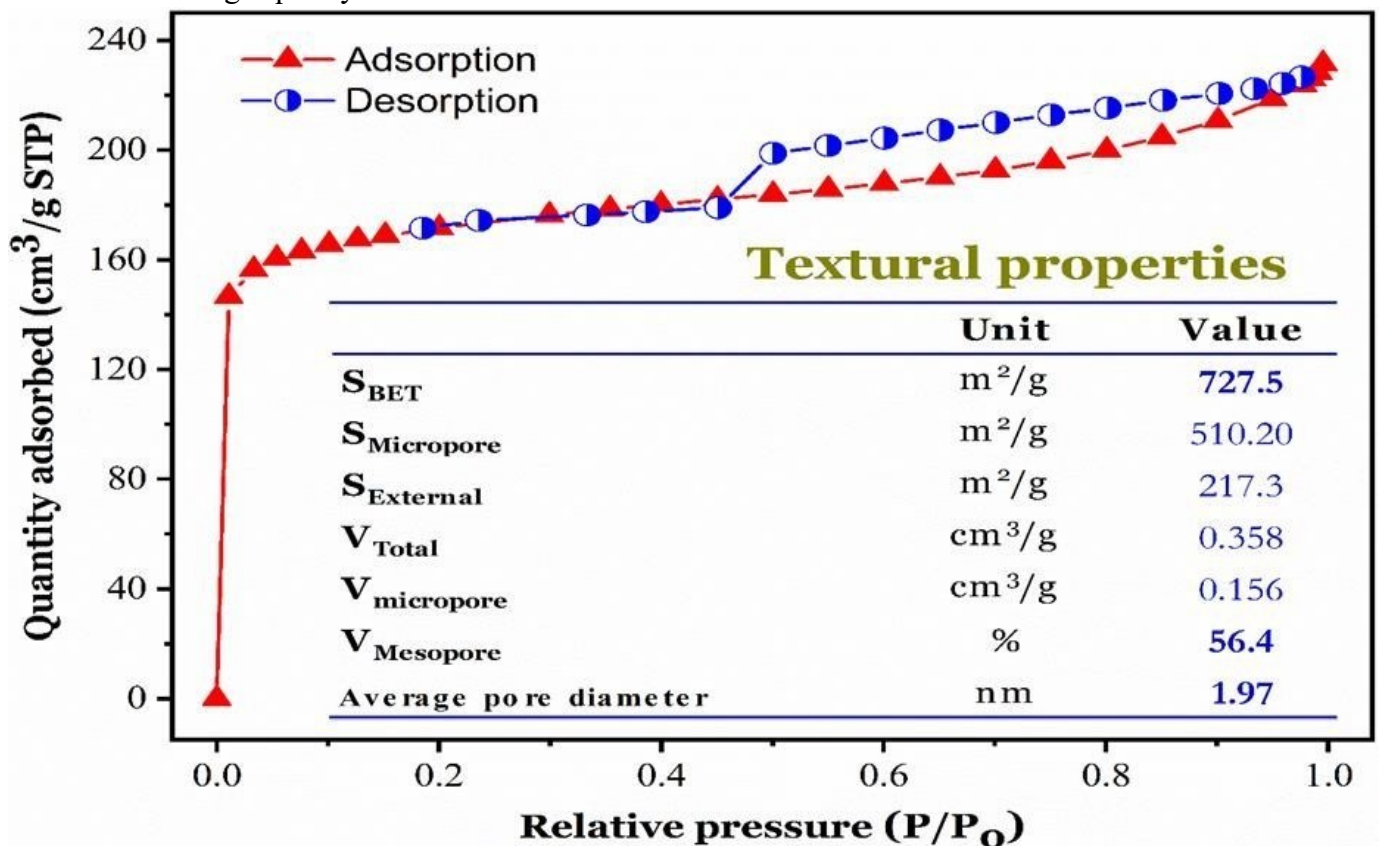
**Figure 1: N2 adsorption/desorption isotherm of B692 adsorbent at 77 K and its textural characteristics**

## II.  CONCLUSIONS

To recover crystal violet dye from water, B-692 BIOCHARAS EFFECTIVE ADSORBENTS WERE PRODUCED USING COQUILLES D'ARACHIDE. The highest sorption performance was demonstrated by B 692, which had a Langmuir sorption capacity of 209 MG/G at 45°C. It was concluded that the adoption process was exothermic and spontaneous. THE ADSORPTION PROCESS'S MAIN MECHANISMS WERE FOUND TO INCLUDE PORE FILLING, VAN DER WAALS FORCES, AND ELECTROSTATIC ATTRACTION. The prepared additives demonstrated remarkable reusability, retaining their efficacy for as long as four cycles without necessitating further intervention. The potential of using several types of biochar derived from coquilles d'arachide as affordable and effective materials for the environmentally friendly remediation of colored wastewaters is highlighted in this study.

### Acknowledgments

### REFERENCES

[1] Mittal A, Mittal J, Malviya A, et al. Adsorption of hazardous dye crystal violet from wastewater by waste materials. J Colloid Interface Sci. 2010;343(2):463–473. Doi: 10.1016/j.jcis.2009.11.060

[2] Saeed A, Sharif M, Iqbal M. Application potential of grapefruit peel as dye sorbent: Kinetics, equilibrium and mechanism of crystal violet adsorption. J Hazard Mater. 2010;179(1–3):564–572. Doi: 10.1016/j.jhazmat. 2010.03.041.

[3] Maley AM, Arbiser JL. Gentian violet: A 19th century drug re-emerges in the 21st century. Exp Dermatol. 2013;22(12):775–780. Doi: 10.1111/exd.12257

[4] Abu Elella MH, Sabaa MW, ElHafeez EA, et al. Crystal violet dye removal using crosslinked grafted xanthan gum. Int j biol macromol. 2019; 137:1086–1101. doi: 10. 1016/j.ijbiomac.2019.06.243

[5] Tran HN, Wang YF, You SJ, et al. Insights into the mechanism of cationic dye adsorption on activated charcoal: The importance of Π–Π interactions. Process SafEnviron Prot. 2017; 107:168–180. doi: 10. 1016/j.psep.2017.02.010

[6] Tran HN, Tomul F, Thi Hoang Ha N, et al. Innovative spherical biochar for pharmaceutical removal from water: Insight into adsorption mechanism. J Hazard Mater. 2020;394(January):122255. doi: 10.1016/j.jhaz mat.2020.122255

[7] Aichour A, Zaghouane-Boudiaf H, Mohamed Zuki FB, et al. Low-cost, biodegradable and highly effective adsorbents for batch and column fixed bed adsorption processes of methylene blue. J Environ Chem Eng. 2019 ;7(5) :103409. doi: 10.1016/j.jece.2019.103409

[8] Chahinez H-O, Abdelkader O, Leila Y, et al. One-stage preparation of palm petiole-derived biochar: Characterization and application for adsorption of crystal violet dye in water. Environ Technol Innov. 2020 ;19 :100872. doi: 10.1016/j.eti.2020.100872

[9] Zulfajri M, Kao YT, Huang GG. Retrieve of residual waste of carbon dots derived from straw mushroom as a hydrochar for the removal of organic dyes from aqueous solutions. Sustainable Chem Pharm. 2021;22 (March):100469. doi: 10.1016/j.scp.2021.100469.

[10] Hadj-Otmane C, Ouakouak A, Touahra F, et al. Date palm petiole–derived biochar: effect of pyrolysis temperature and adsorption properties of hazardous cationic dye from water. Biomass Convers Biorefin. 2022. doi:10.1007/s13399-022-03127-3.

[11] Salem DB, Ouakouak A, Touahra F, et al. Easy separ able, floatable, and recyclable magnetic-biochar/algi nate bead as super-adsorbent for adsorbing copper ions in water media. Biores Technol. 2023; 383:129225. doi: 10.1016/j.biortech.2023.129225

[12] Fazlzadeh M, Khosravi R, Zarei A. Green synthesis of zinc oxide nanoparticles using Peganum harmala seed extract, and loaded on Peganum harmala seed powdered activated carbon as new adsorbent for removal of Cr (VI) from aqueous solution. Ecol Eng. 2017; 103:180–190. doi: 10.1016/j.ecoleng.2017.02.052

# Design, performance analysis, and modeling of Permanent Magnet Linear Generator for wave energy applications

Amal NASRI [#1], Iskander BOULAABI[#2], Mansour HAJJI[*3], Anis SELLAMI[#4], Fayçal BEN HMIDA[#5]

First Author[#1], Second Author[*2], Third Author[#3]

[#]*LISIER, National High School of Engineers of Tunis ENSIT, University of Tunis, Tunisia*
[*]*UR16ES03, Higher Institute of Applied Sciences and Technology of Kasserine, Kairouan University, Tunisia*

Email 1 – nasryamal1@gmail.com

## Introduction:

Renewable energy resources emerged due to the exhaustion of carbon-based fuels. They can sufficiently satisfy human needs for electricity. Recently, many researchers have been devoted to exploiting oceanic wave energy which could prove to be a long-time solution for the forthcoming energy shortages (Oprea, 2011) and has developed rapidly (Arkadan, 2015) and (Taguchi, Farrok, 2018). In addition, Wave Energy Converter (WEC) systems conceivably have the highest power density among all renewable energy systems. Usually, these systems are composed of a mechanical converter, an electrical generator that converts sea waves into electricity, and a power electronics section dedicated to the conversion, transmission, and storage of the generated electrical power (Trapanese, 2018).

In fact, and according to the principle of hydro-mechanical conversion by Falcao et al. (Antonio, 2010), WEC systems are classified into various methods amongst them the Archimedes Wave Swing (AWS). This technology uses a tubular or a flat permanent magnet linear generator (Polinder, 2004). According to (Lopez, 2013) and (Hamim, 2013), the flat generator is more efficient than the rotational generator since the flat form is inexpensive and simple to construct. They discuss the advantages of a flat type over a tubular type in (Li, 2009) and (Prado, 2011). The efficiency, output power, current, and voltage have all improved with the flat-type structure. Furthermore, this generator enables performance with a high-power factor and satisfactory efficiency which makes it applicable to electrical power generation systems (Ackermann, 2005). So, it can be used in AWS technology.

The generator system was described for the first time in (Polinder, 2000). Figure 1 depicts the basic model of the AWS system. It is divided into two parts. The first component is attached to the seabed, while the second part is a floating component, which can be moved. The AWS is a cylinder-shaped chamber that is filled with air. The pressure quantity created by water leads the floater component to descend lower in the presence of waves. When the wave recedes, the pressure decreases, and the air in the chamber pushes the top section back to its original position, serving as a spring. The main concept of power generation is the linear motion generator. The

AWS technology was employed in the construction of a linear generator for marine application, according to (Polinder, 2004), (Da, 2003) and (Polinder, 2005). Many problems related to using linear generators are addressed in (Polinder, 2004linear). They provide a significant contribution to the solution of this problem in (Vermaak, 2010).

## Résultats :
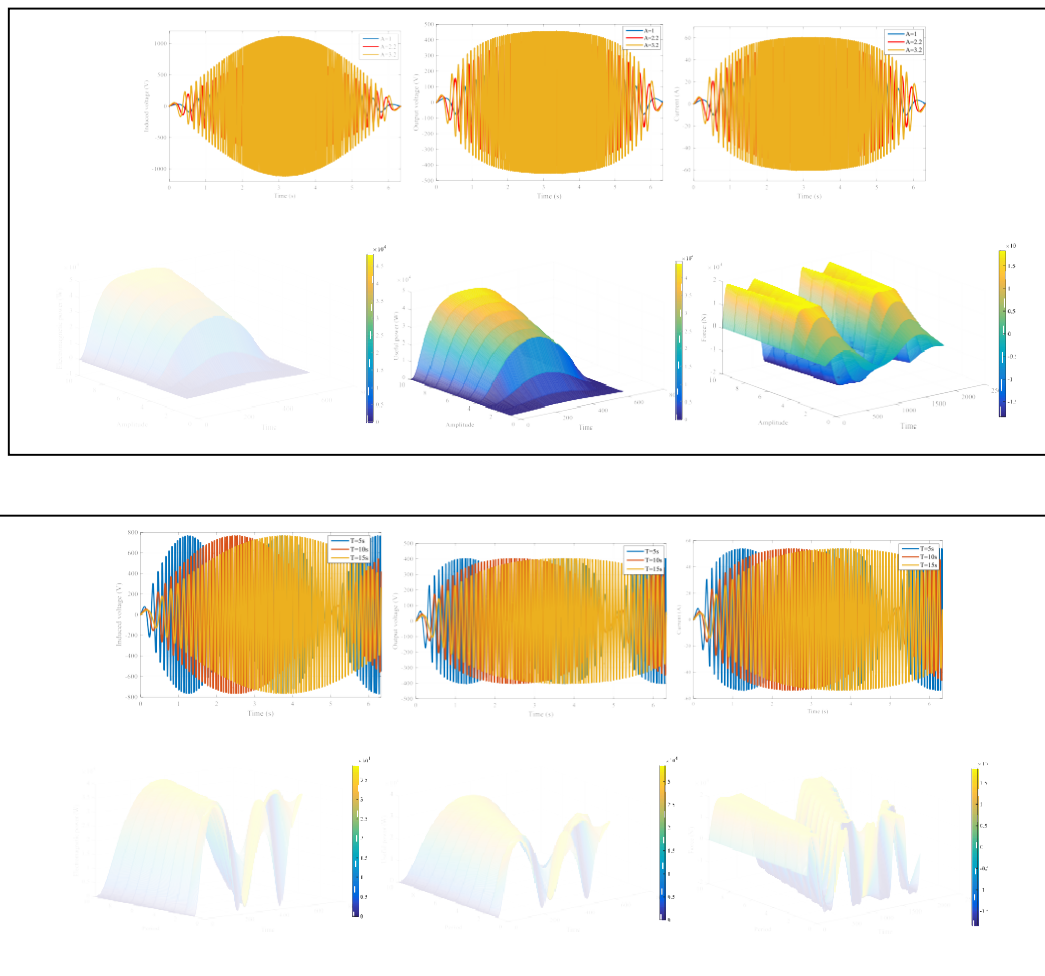




## Conclusion:

The permanent magnet linear generator design, adapted to wave energy conversion, was the subject of this paper. Using analytic forms and generator specifications, the geometrical parameters are calculated. Then, the dynamic model of PMLG was established in the d-q reference frame using Park transformation. Finally, the model was simulated using MATLAB software to investigate the influence of wave parameters on generator efficiency. We can find that increased energy efficiency is possible with a high frequency or amplitude.

## Références :

*Oprea, 2011:* C.A. Oprea, C. S. Martis, F. N. Jurca, D. Fodorean, and L. Szabó, "Permanent Magnet Linear Generator for Renewable Energy Applications: Tubular vs. Four-Sided Structures", International Conference on Clean Electrical Power (ICCEP), 2011.

*Arkadan, 2015:* A. R. Arkadan, N. Al-Aawar, and A. O. Hariri, "EM-Taguchi module for characterization of WAD", IEEE Transactions on Magnetics, 2015.

*Farrok, 2018*: O. Farrok, R. Islam, R. Islam Sheikh, Y. Guo, J. Zhu and G. Lei, "Oceanic Wave Energy Conversion by a Novel Permanent Magnet Linear Generator Capable of Preventing Demagnetization", IEEE Transactions on Industry Applications, 2018.

*Trapanese, 2018*: M. Trapanese, V. Boscaino, G. Cipriani, D. Curto, D. Vincenzo and V. Franzitta, "A Permanent Magnet Linear Generator for the Enhancement of the Reliability of a Wave Energy Conversion system", IEEE Transactions on Industrial Electronics, May 2018.

*Antonio, 2010:* F. António and O.Falcão, "Wave energy utilization: A review of the technologies", Renewable and Sustainable Energy Reviews, 2010.

*Polinder, 2004*: H. Polinder, M.E.C. Damen, and F. Gardner, "Linear PM Generator system for wave energy conversion in the AWS. Energy Conversion", IEEE Transactions on Energy Conversion, 2004.

*Lopez, 2013*: L. Iraide, J. Andreua, S. Ceballosb, M. Iñigo, and K.Iñigo, "Review of wave energy technologies and the necessary power-equipment", Renewable and Sustainable Energy Reviews, 2013.

*Hamim, 2014*: M. A. F. M. Hamim, T Ibrahim, and N.M. Nor, "Design of Portable Pico Linear Permanent Magnet Generator for Wave Energy Conversion", International Conference on Information Technology and Electrical Engineering (ICITEE), 2014.

*Li, 2009:* Q. f. Li, J. Xiao, and Z. Huang, "Flat-type permanent magnet linear alternator: A suitable device for a free piston linear alternator", Journal of Zhejiang University SCIENCE A, 2009.

*Prado, 2011*: M. Prado and H. Polinder, "Direct drive in wave energy conversion AWS full scale prototype case study", IEEE Power and Energy Society General Meeting, 2011.

*Ackermann, 2005:* A. Thomas, "Wind Power in Power Systems", Book, Royal Institute of Technology Stockholm, 2005.

*Polinder 2000:* Polinder H, Gardner F, Vriesema B, "Linear PM generator for wave energy conversion in the AWS", Proceedings of the Eighth International Conference on Electrical Machines, Helsinki, 2000.

*Da, 2003*: J. Sa da Costa, P. Pinto, A. Sarmento, F. Gardner., "Modeling of an ocean waves power device AWS", IEEE Conference on Control Applications, 2003.

*Polinder, 2005*: H. Polinder et al., "Conventional and TFPM linear generators for direct-drive wave energy conversion", IEEE Transactions on Energy Conversion, 2005.

*Vermaak, 2010*: R. Vermaak and M. J. Kamper, "Novel permanent magnet linear generator topology for wave energy conversion", 5th IET International Conference on Power Electronics, Machines and Drives (PEMD), 2010.

*Polinder, 2005*: H. Polinder, M. E. C. Damen and F. Gardner: "Design, modelling and test results of the AWS PM linear generator", European Transactions on Electrical Power, 2005.

*Polinder, 2005:* H. Polinder and M. Scuotto, "Wave energy converters and their impact on power systems", In Proceedings of the International Conference on Future power systems, 2005.

*Ivanova, 2005:* I. A. Ivanova, H. Bernhoff, O. Agren, M. Leijon, "Simulated generator for wave energy extraction in deep water", Ocean Engineering 2005;

*Danielsson, 2004:* O. Danielsson, ES. Sjostedt, T. Thorburn, M. Leijon, "Simulated response of a linear generator wave energy converter", ISOPE paper 2004.

*Maddugari, 2019:* S. K. Maddugari, V. B. Borghate, S. Sabyasachi and R. R. Karasani, "A Linear-Generator-Based Wave Power Plant Model Using Reliable Multilevel Inverter", IEEE Transactions on Industry Applications, 2019.

*Colli, 2005:* V. DelliColli, R. Di Stefano and M. Scarano, "A tubular generator for marine energy direct drive applications", IEEE International Conference on Electric Machines and Drives, 2005.

*Simoes, 2014*: M. G. Simões and F. A. Farret, Modeling and analysis with induction generators. CRC Press, 2014

*Jayalakshmi , 2012:* N. Jayalakshmi, D. Gaonkar, and K. S. K. Kumar, "Dynamic modeling and performance analysis of grid connected pmsg based variablespeed wind turbines with simple power conditioning system," in 2012 IEEE international conference on power electronics, drives and energy systems (PEDES). IEEE, 2012, pp. 1–5.

*Mouni, 2008:* E. Mouni, S. Tnani, G. Champenois, "Synchronous generator modelling and parameters estimation using least squares method", Simulation Modelling Practice and Theory, 2008.

# Using the Fractional Order Adaptive PID Controller to improve the Performances of Aircraft pitch angle System

1. Zahir Asradj [1,2], 2. Yassine Bensafia[2], 3. Imad Merzouk [1]

l Applied Automation and Industrial Diagnostics Laboratory, Faculty of Science and Technology,
University of Djelfa, 17000, Algeria (1),

2 LISEA Laboratory, Electrical Engineering Department, Faculty of Sciences and Applied sciences,
University of Bouira, 10000 - Algeria (2),

*Abstract*. Fractional calculus, which deals with derivatives and integrals of non-integer order, has seen a resurgence of interest in recent years. It has found applications in various fields such as control theory, signal processing, physics, and engineering. The use of fractional calculus in control theory has led to the development of new control algorithms and methods that offer advantages in dealing with complex and non-linear systems. The current research work presents the use the fractional adaptive PID controller approach optimized by genetic algorithm to improve the performances (rise time, setting time , overshoot and mean absolute error) for Aircraft by introducing fractional order integrator and differentiator in the classical feedback adaptive PID controller. To validate the arguments, effectiveness and performances analysis of the proposed fractional order adaptive PID controller optimized by genetic algorithm have been studied in comparison to the classical adaptive PID controller. Numerical simulation and analysis are presented to verify the **best** controller. The Fractional order adaptive PID gives the **best** results in terms of settling time, rise time, overshoot and mean absolute error. This approach can also be generalized to others fractional and integer systems in order to improve their performances and noise rejection.

*Keywords*. Fractional systems, Control theory, fractional Adaptive PID controller, Robustness analysis, Aircraft System.

## I. INTRODUCTION

Fractional calculus emerged as a mathematical discipline subsequent to the initial discussion of a fractional-order (FO) derivative, involving speculation between L'Hospital and Leibniz [1,2].

The practical applications of fractional order differentiation have captured the interest of researchers across a wide range of scientific disciplines, particularly in the realm of applied sciences [3,4].

In 1997, Podlubny proposed the concept of FOPID controllers. He also demonstrated how this type of controller exhibits faster response when used for controlling fractional order systems, in comparison to conventional PID controllers [3,5,21].

It is widely recognized that adaptive control methods are among the most effective techniques for addressing parametric uncertainty in both linear and nonlinear systems. However, the emphasis has mainly been on utilizing integer order systems to implement adaptive control methods [6,7]. Monje et al [3] have documented the utilization of fractional calculus in conventional systems and control. Additionally, they have reported on adaptive functional projective and feedback control schemes for the synchronization of chaotic systems with fractional order, as well as the development of an adaptive sliding-mode controller for such systems [8]. The impact of uncertain fractional order in chaotic systems can be managed by employing various practical methods, including an adaptive fractional-

order switching control method, an adaptive fuzzy sliding-mode control method, and a synchronization control method [9].

A genetic algorithm is a critical technique in computing for finding precise or approximate solutions to optimization and search problems. The design of the genetic algorithm's fitness function is vital as it greatly influences the desired output. The fitness value of each individual is calculated by applying the fitness function to it [10,11].

The primary contribution of this study lies in employing a fractional adaptive PID controller approach optimized by a genetic algorithm to enhance the performance (rise time, settling time, and overshoot) of the aircraft system. This is achieved by introducing fractional order integrator and differentiator in the traditional feedback adaptive PID controller. The optimization parameters are obtained using the fitness function.

The manuscript is structured as follows: we first explore the fundamentals of fractional order systems, followed by an examination of algorithms for both integer and fractional adaptive PID controllers. Subsequently, we present the results obtained from performance analysis through simulations applied to the aircraft system using both integer and fractional adaptive PID controllers. Finally, we conclude and outline future prospects for the study.

## II. Fractional Order Systems

Fractional calculus, a subfield of calculus, is widely recognized for its use of non-integer orders to generalize derivatives or integrals of functions [12,13]. Fractional approximation techniques enable the application of fractional order systems in various areas such as control theory [14,15,20], renewable energy [21], economic systems [22],..etc.

Several factors determine the relative advantages of any approximation, including differentiation order, frequency behavior, and time responses. This discussion includes various approximations and their comparative analysis with others [16,17].

The existing approximations fall into two distinct domains: the frequency domain, specified as the s-domain, and the time domain, specified as the z-domain. These approximations in the frequency and time domains are also referred to as continuous and discrete approximations [18,19].

The Oustaloup method is based on the function approximation as follows:

$$G_f(s) = S^\alpha \qquad , \alpha \in R^+$$

By taking into account the rational function:

$$G_f(s) = K\,G \prod_{k=1}^{N} \frac{s + w_k^{'}}{s + w_k}$$

However, the poles, zeros, and gain can be evaluated as;

$$w_k^{'} = w_b\,w_u^{(2k-1-\gamma)/N} \qquad , w_k = w_b\,w_u^{(2k-1+\gamma)/N} , K = w_h^{\gamma}$$

Where $w_u$ represents the unity gain in frequency and the central frequency in a geometrically distributed frequency band. Let $w_u = \sqrt{w_h w_b}$, where, $w_h$ and $w_b$ represent the upper and lower frequencies, respectively. $\gamma$ and N are the orders of derivative and filter, respectively.

## III. Genetic Algorithm Optimization

A genetic algorithm is a method for finding precise or approximate solutions to optimization problems [25]. The essential steps in the genetic algorithm process are encoding, evaluation, crossover,

mutation, and decoding. The initial population is chosen at random, and each individual's fitness is then calculated. The design of the fitness function is particularly important in genetic algorithms because the desired output significantly depends on the design of the fitness function.

The steps of the algorithm of GA given in [25] are:

1. Choose the initial population

2. Each individual in the population should have their fitness evaluated.

3. Repeat

Choose the most qualified people to reproduce

Create a new generation through hybridization and mutation, then produce children.

evaluation of the fitness of the progeny.

Children should be used to replace the least desirable population.

4. Until termination

IV. INTEGER ADAPTIVE PID CONTROLLER

The integer adaptive feedback control law is represented by the equation 3.[10]

u(t) = −k$_c$[k$_1$(t)e(t) + I{k$_2$(t)e(t)} + D(k$_3$(t)e(t))] (3)

With:

$k_1(t) = k_p(t) + \alpha_1 k_i(t) + \alpha_3 k_d(t)$

$k_2(t) = \alpha_2 k_i(t) , k_3(t) = \alpha_4 k_i(t), k_p(t) = e^2(t)$

$k_i(t) = I\{e^2(t)\}$ and $k_d(t) = D\{e^2(t)\}$

$e(t) = y(t) - r(t)$

Where $k_c$, $\alpha_1$ and $\alpha_2$ are positive constants.
The standard schematic depiction of the entire system is illustrated in figure 1, highlighting the remarkable simplicity of the control system.
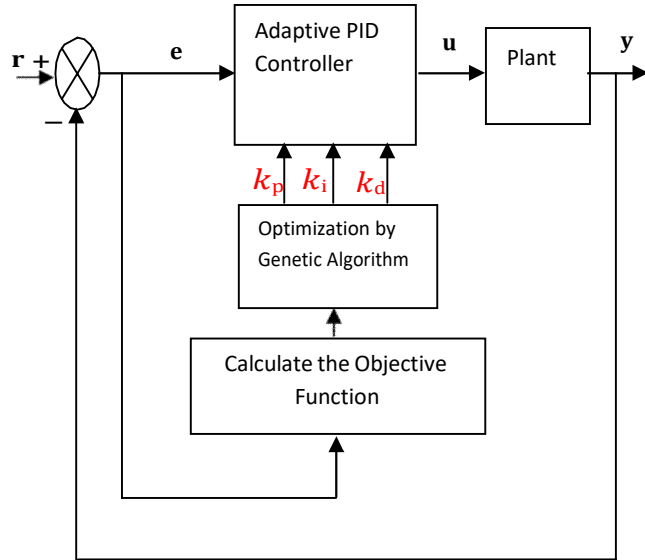
Fig. 1. Classical Adaptive PID Control System.

## V. FRACTIONAL ADAPTIVE $PI^\Lambda D^M$ CONTROLLER

The fractional adaptive feedback control law is expressed by equation (4):

$$u(t) = -k_c[k_1(t)e(t) + I^\lambda\{k_2(t)e(t)\} + D^\mu(k_3(t)e(t))]\ (4)$$

With:

$$k_1(t) = k_p(t) + \alpha_1 k_i(t) + \alpha_3 k_d(t)\ ,k_2(t) = \alpha_2 k_i(t)\ ,\ k_3(t) = \alpha_4 k_i(t)$$

and $k_p(t) = e^2(t)$ , $k_i(t) = I^\lambda\{e^2(t)\}$ ,$k_d(t) = D^\mu\{e^2(t)\}$

$$e(t) = y(t) - r(t)$$
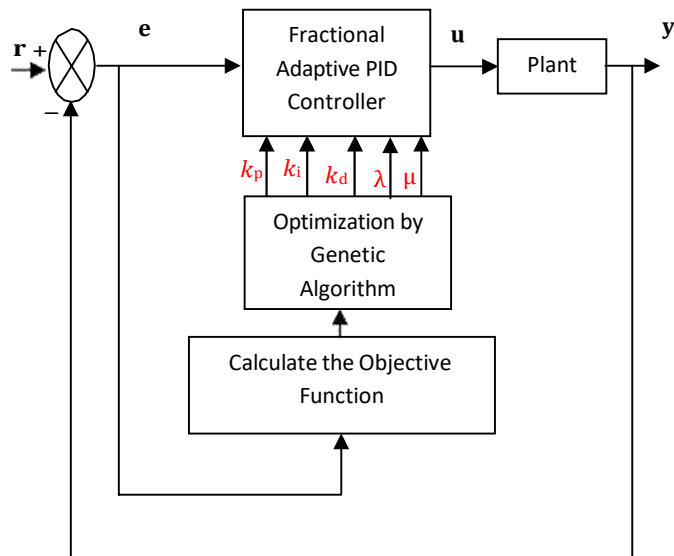


Fig. 2. Fractional Adaptive PID Control System

### VI. Results and Discussion

The error between the computed and measured output is utilized to establish the fitness function F, which will be employed for minimization. It is defined by the Mean Absolute Error (MAE) as follows[27]:

$$MAE = \frac{\sum_{i=1}^{N} y(i) - r(i)}{N} \quad (5)$$

were y is the measured output system and r is the desired output.

During flight, the aircraft can be manipulated into three rotational axes. Rotation along the vertical axis is called "yaw," along the longitudinal axis is called "roll," and along the lateral axis is called "pitch." These axes intersect at the center of gravity of the aircraft.

The mathematical model for the pitch angle is depicted in Figure 3 [26,27].
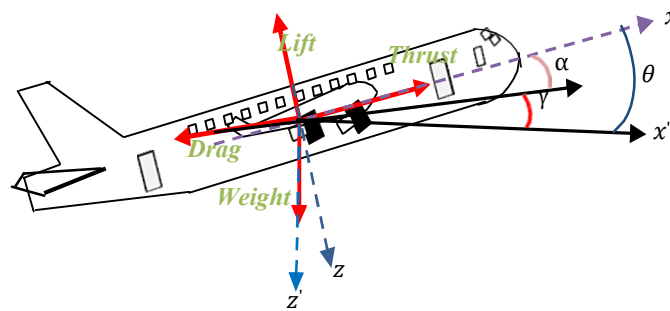


Fig.3. Pitch control description

The aircraft's dynamic behavior is described by the following set of relations:

$$\frac{d\alpha}{dt} = \mu\Omega\sigma \left[ -(C_L + C_D)\alpha + \frac{1}{\mu - C_L} q - (C_M \sin\gamma)\theta + C_L \right] \quad (6)$$

$$\frac{dq}{dt} = \frac{\mu\Omega}{2i_{yy}} [(C_M - \eta(C_L + C_D))\alpha + (C_m + \sigma(1 - \mu C_L))q + (\eta C_W \sin\gamma)\delta] \quad (7)$$

$$\frac{d\theta}{dt} = \Omega q \quad (8)$$

Where

$\alpha, \theta, \gamma, \delta$: Attack, pitch, flight path and elevator deflection angles respectively.

$C_T, C_D, C_L, C_W, C_M$ Thrust, drag, lift, weight and pitch moment coefficients respectively.

$\sigma, 5$: Constants

$q$: Pitch rate

$\rho$: Air density

$S$: Wing platform area

m: Mass of the aircraft

$i_{yy}$: Inertia normalized moment

The transfer function for the aircraft's pitch angle is provided in Equation (9).

$$G_P(s) = \frac{\theta(s)}{\Delta(s)}$$

$$G_P(s) = \frac{1.151\,s + 0.1774}{s^3 + 0.739\,s^2 + 0.921s} \tag{9}$$

Where:  $\Delta(s)$ : is the elevator deflection

$\theta(s)$ : is the pitch angle

Figure 4 shows the pitch angle of the aircraft using the Integer adaptive PID Controller with the following optimized parameter values: k_p=114.8231, k_i=4.4575, k_d=49.0933.



Fig. 4. Pitch angle of the Aircraft using the Integer adaptive PID Controller

Figure 5 illustrates the aircraft's pitch angle using the Fractional adaptive PID Controller with the following optimized parameter values: k_p=6.5582, k_i=0.15435, k_d=673.5805, λ=0.20115, μ=0.99731.
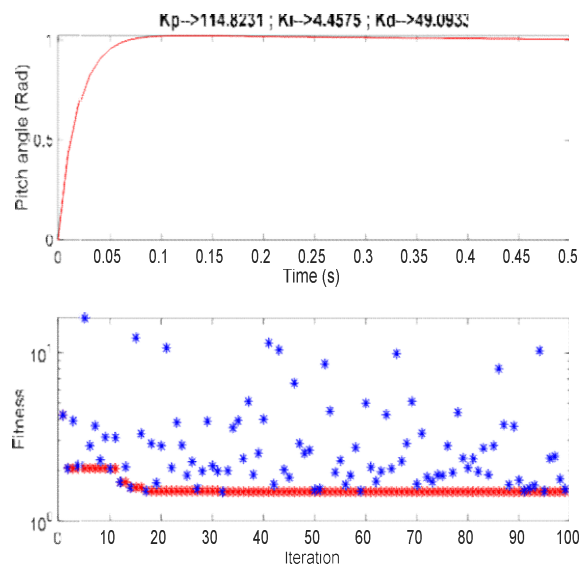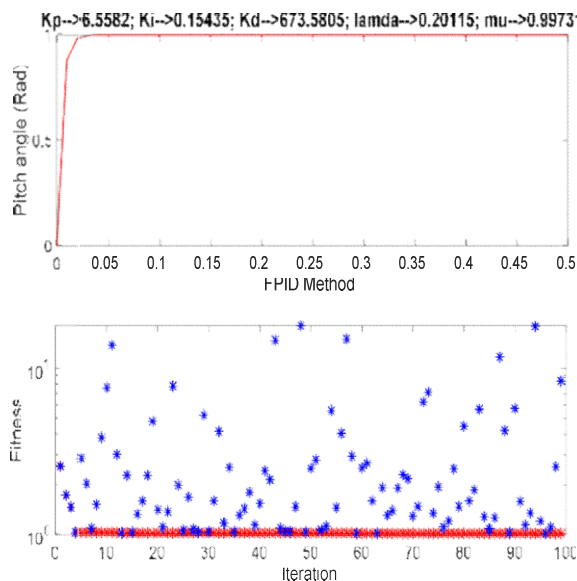
Fig. 5. Pitch angle of the Aircraft using the Fractional adaptive PID Controller.

The performance evaluation of the proposed fractional order adaptive PID controller and the classical adaptive PID controller is presented in the table below.

Table 1. Transient Response Stability Parameters of Aircraft System

| Controllers | Overshoot [%] | Setting time [s] | Rise time [s] | Mean Absolute Error (Rad) |
|---|---|---|---|---|
| APID | 1.7242 | 0.0595 | 0.0373 | 0.0012 |
| FAPID | 0.0533 | 0.0193 | 0.0106 | 0.0005 |

We observe that the fractional adaptive PID controller for the aircraft system provides significant improvements in overshoot, settling time, rise time, and mean absolute error compared to the results obtained with the integer adaptive PID controller.

## VII. CONCLUSION

In this paper, we investigate the performance analysis of the integer adaptive PID controller and the fractional adaptive PID controller optimized by genetic algorithm for the aircraft system. The fractional approach enables significant improvements in overshoot, settling time, rise time, and mean absolute error compared to the results obtained with the integer adaptive PID controller. The simulation studies demonstrate the strong performance of the proposed approach and confirm its superiority over the integer adaptive PID controller. In future work, we will explore the extension of the fractional adaptive control approach to other fractional systems to enhance their robustness and noise rejection.

## REFERENCES

[1] Monje.C. A., "Fractional-order systems and controls: fundamentals and applications," Springer, (2010).

[2] Chen. Y., Vinagre. B. M., and Podlubny .I, "Continued fraction expansion approaches to discretizing fractional order derivatives an expository review," in Nonlinear Dynamics, vol. 38, no.1–4, (2004), 155-170.

[3] Bhatt. R., Parmar .G , Gupta .R, Sikander. A, "Application of stochastic fractal search in approximation and control of LTI systems," In: Microsyst. Technol. Vol.25,( 2019), 105-114.

[4] Srinivasan .S, Karunanithi T., " Design of PI controller for bio-reactors for maximum production rate", International Journal of Chem-Tech Research, Vol.2, No.3, (2010), 1679-1685.

[5] Wang .F. S, Juang. W. S, Chan. C. T, " Optimal tuning of PID controllers for single and cascade control loops", Chemical Engineering Communications, 132 , (1995),15-34.

[6] Ladaci . S, Loiseau. J.J, Charef .A, " Adaptive Internal Model Control with fractional order Parameter ", Int. J. Adaptive Control and Signal Processing, nr 24,(2010), 944-960.

[7] Maciej . S, " Another Approach to the Fractional Order Derivatives, *Przegląd Elektrotechniczny,* 91 (2015),nr. 2, 153-156.

[8] Khettab . K , Ladaci . S, Bensafi . Y., "Fuzzy adaptive control of fractional order chaotic systems with unknown control gain sign using a fractional order Nussbaum gain ", In: IEEE/CAA Journal of Automatica Sinica, vol. 4(2), (2019), 1-8.

[9] ULLAH . Nasim , WANG . S , KHATTAK .M. I "Fractional Order Fuzzy Backstepping Torque Control of Electrical Load Simulator", *Przegląd Elektrotechniczny,* 89 (2013),nr. 5, 237-240.

[10] Haneet . K, Parul S , Pawanesh . A , " Analysis of fitness function in genetic algorithms. Journal of Scientific and Technical Advancements", V 1, No. 3,(2015) , 87-89.

[11] Djouambi . A, Charef . A , Voda Besançon . A , " Fractional Order Robust Control Based on Bodes Ideal Transfer Function", RS-JESA, vol. 42, Fractional order systems, (2008), 999-1014.

[12] Oustaloup . A, Levron .F, Mathieu . B and Nanot . F, " Frequency-Band Complex Non integer Differentiator: Characterization and Synthesis", IEEE Transactions on Circuits and Systems I, vol.47, n°1, (2000), 25-39.

[13] Oustaloup. A, Sabatier . J, Lanusse .P, " From fractal robustness to CRONE control", Fractionnal Calculus and applied Analysis, (1999), 1-30.

[14] Oustaloup . A, "La Dérivation Non Entière : Théorie, Synthèse et applications ", Hermès: Paris, (1995).

[15] Oustaloup . A, Mathieu. B , " La commande CRONE : du scalaire au multivariable ", HERMES, Paris,(1999).

[16] Axtell . M, Bise . M.E, " Fractional calculus applications in control systems ", the IEEE National Aerospace and Electronics Conference, New York, USA, (1990), 563-566.

[17] Calderon . A. J., Vinagre. B.M. and Feliu . V , " Fractional order control strategies for power electronic buck converters ", Signal Processing, vol. 86, (2006), 2803-2819.

[18] Bensafia .Y, Ladaci .S, Khettab .K, " Using a Fractionalized Integrator for Control Performance Enhancement ", International Journal of Innovative Computing, Information and Control,( 2015).

[19] Y. Bensafia, K. Khettab, H .Idir, " An Improved Robust Fractionalized PID Controller for a Class of Fractional-Order Systems with Measurement Noise ", International Journal of Intelligent Engineering and Systems, DOI: 10.22266/ijies2018.0430.22 ,V 11, No.2, (2018).

[20]   Sabatier . J , Oustaloup .A, Iturricha . A.G , Levron F. , ''CRONE control of continuous linear time periodic systems: Application to a testing bench '',  ISA Transactions, ( 2003),421-436.

[21] Neçaibia . A, Ladaci S., Charef . A, Loiseau. J.J, ''Fractional order extremum seeking approach for maximum power point tracking of Photo-Voltaic panels'',    Frontiers in Energy ; V 9, No.1, (2015), 43–53.

 [22]  Dadras . S, Momeni H.R., '' Control of a fractional-order economical system '',       *Physica* 389,( 2010),2434–2442.

 [23]  Wang . W., Lu . Y, '' Analysis of the Mean Absolute Error (MAE) and the Root Mean Square Error (RMSE) in Assessing Rounding Model'', IOP Conf. Series: Materials Science and Engineering 324, (2018).

[24]   Tenreiro Machado . J. A., " Calculation of Fractional Derivatives of Noisy Data with Genetic Algorithms", Nonlinear Dynamics, Springer, 57(1-2), (2009), 253-260.

[25]    Antonina MALYUSHEVSKAYA, Anna YUSHCHISHINA, Olena MITRYASOVA, Volodymyr POHREBENNYK , Ivan SALAMON, " Optimization of Extraction Processes of Water-Soluble Polysaccharides under the Electric Field Action", *Przegląd Elektrotechniczny*, 97(2021), nr. 12, 73-76.

[26]   Kaçti . V, Ekinci .S, İzci .D., " Efficient Controller Design for Aircraft Pitch Control System Using Henry Gas Solubility Optimization ", DUJE, vol. 11, No.3, (2020), 953-964.

[27] Asradj. Z, Bensafia.Y,  Merzouk.I , "Performances Improvement of Fractional order Systems using the Fractional Order Adaptive PID Controller", *Przegląd Elektrotechniczny*, ISSN 0033-2097, R. 99 NR 8 (2023).

# Numerical study of heat transfer on 3D cavity filled with MWCNT/Water nanofluid: Effect of type of surfactant

Nessrin Manaa [#1], Abidi Awatef[#2], Patrice Estellé*[3], Borjini Mohamed Naceur [#4]

[#]*Research Laboratory of Metrology and Energy System, Monastir University*
*Monatir, Tunisia*

[1]manaa_nessrin@outlook.com

[2]abidiawatef@yahoo.fr

[4]borjininaceur@gmail.com

[*]*LGCM Rennes University*

*F-35000, Rennes, France*

[3]patrice.estelle@univ-rennes1.fr

*Abstract*—**A numerical analysis has been investigated in this work to solve three-dimensional double-diffusive natural convection in a differentially heated cubical enclosure filled with MWCNT-water nanofluid stabilized by lignin and sodium polycarboxylate as surfactants. The study is carried out for different governing parameters as Rayleigh number and nanoparticles's volume fraction. It is obtained that the use of lignin as a surfactant increases heat and mass transfer rate and nanofluid flow better than the use of sodium polycarboxylate as a surfactant. The heat rate and fluid flow increase when nanoparticle volume fraction is less than the critical value, and is deteriorated when it exceed this value.**

*Keywords*— **Natural convection, three-dimensional, nanofluid, surfactant**

## I. INTRODUCTION

Over the last years, the demand on energy is become more intensive due to the extensive growth of industry and population. In fact, energy is considered as essential element for human being because her daily activities which need energy. It exist many applications in industrial and research where the phenomena of natural convection is present such as the crystal growth for the manufacture of semiconductors and electronics equipments cooling, solar collectors, home ventilation and heat exchangers. Moreover, utilizing nanofluid it one of the new method to conservation energy during natural convection. These fluids are manufactured by the dispersion of nanoparticles (size: $10^{-9}$-$10^{-11}$ m) in simple fluids. It exists many types of nanoparticles used in nanofluids that differ nature, such as metallic (Al, Cu, Ag...), oxide ($Al_2O_3$, $TiO_2$, CuO…) and carbon-based materials. Among all nanoparticles available for producing nanofluids, carbon nanotubes (CNT) are more recommending than other traditional nanoparticles because of their relatively low density and very high thermal conductivity. Wen and Ding [1] studied the effective thermal conductivity of aqueous suspensions of MWCNTs. They used the sodium polycarboxylate as surfactant to stabilize the nanofluids. They obtained an enhancement of thermal conductivity when the nanoparticles volume concentration increases. Estellé et al. [2] investigated the thermal conductivity of carbon nanotube water-based nanofluids. They studied the effect of the volume fraction of nanoparticles, temperature, nanoparticles aspect ratio and different types of surfactant. They observed an enhancement of thermal conductivity of nanofluid at low volume fraction. However, this enhancement is weakly affected by the carbon nanotubes aspect ratio and the type of surfactant used. A study of the effect of lignin as surfactant on viscosity and thermal conductivity of CNT/water-based nanofluids was investigated by Estellé et al. [3]. They compared the effect of lignin on the viscosity and thermal conductivity of CNT/water nanofluid with the effect of sodium polycarboxylate. They noticed that the thermal conductivity of nanofluid increase with the nanoparticles volume concentration. Rahman et al. [4] investigated a numerically the natural convective heat transfer and fluid flow in a square cavity filled with CNT–water nanofluid with non-isothermal heating. They founded that there is an optimum value for nanoparticles volume fraction to control heat transfer, temperature distribution and flow field. Job and Gunakala [5] investigated the unsteady MHD natural convection flows of two types of nanofluid $Al_2O_3$/water and SWCNT/water within a symmetrical wavy trapezoidal enclosure with viscous and Joule dissipation effects. They obtained that the SWCNT/water nanofluid has a higher heat transfer rate at the wavy bottom wall than the $Al_2O_3$/water nanofluid.

Estellé et al. [6] investigated theoretically the natural convection in a square cavity partially heated filled with CNT water-based nanofluids. They analyzed the effect of the average temperature and the nanoparticles volume fraction, driving temperature between hot and cold walls and role of surfactant. They founded that the Nusselt number of nanofluids is decreased with the increase of the volume fraction of nanofluid.

Minea and Estellé [7] carried out a numerical study of the heat transfer behavior of carbon nanotubes nanofluids under laminar forced flow in horizontal pipe. They obtained that the convective heat transfer coefficient of nanofluid is better for low Re number and higher nanoparticules volume fraction. Kolsi et al. [8] performed a computational analysis on a CNT-water nanofluid filled in open cubic cavity. This work is solved for different governing parameters as Rayleigh number, nanoparticles volume fraction, Hartmann number and inclination angle of the fin. It is concluded that heat transfer rate and fluid flow depend of these parameters. Al-Rashed et al. [9] carried out a numerical study of entropy generation inside an inclined cubical cavity differentially heated filled with CNT/water nanofluid. They analyzed the effects of several parameters such as Rayleigh number, nanoparticles volume fraction, inclination angle of cavity and thermal conductivity ratio on entropy generation. Rahimi et al. [10] conducted a numerical and experimental analysis on heat transfer performance of 3D natural convection in a cubic cavity filled with DWCNTs-water nanofluid at different temperature differences between side hot and cold walls. In this work, the thermo-physical properties such us the thermal conductivity and the dynamic viscosity, of the DWCNTs-water nanofluid are experimentally evaluated. Also, they demonstrated that it exist an optimum value of solid volume fraction for highest value of average heat transfer coefficient and Nusselt number. Over this optimum, both parameters are deteriorated.

Manaa et al. [11] investigated the thermo-solutal natural convection of a micropolar nanofluid filled 3D enclosure with different types of nanoparticles (Al$_2$O$_3$, TiO$_2$, Cu and Ag) considering the effect of relevant parameters on heat and mass transfer characteristics. They obtained that both heat and mass transfer rates and the three-dimensional character of the flow for the micropolar nanofluid model are smaller compared with that of a pure nanofluid model. Their results show that the rates of heat and mass transfer decrease with an enhancement in nanoparticles volume fractions. Additionally, they concluded that the type of nanoparticles significantly influences heat and mass transfer rates. Manaa et al. [12] realized a numerical work about three-dimensional double-diffusive natural convection in a cubic cavity filled with Cu-Al$_2$O$_3$/water micropolar hybrid nanofluid. They compared the performance enhancement of Cu-Al$_2$O$_3$/water micropolar hybrid nanofluid with the Cu/water simple nanofluid. Besides, the influences of pertinent parameters such as concentration of nanoparticles, Rayleigh number, buoyancy ratio, and micropolar parameter on the flow field and heat and mass transfer rates are analyzed.

The main aim of this work is to perform a computational analysis on the three-dimensional double diffusion natural convection in CNT/water nanofluid stabilized with two types of surfactants lignin and sodium polycarboxylate. The current work can be used to control and monitor heat and mass transfer and fluid flow in a cubic enclosure.

## II. ANALYSIS

A simple schematic view of the thermo-solutal natural convection problem under study is described in Fig. 1. The cube is filled with a CNT water-based nanofluid stabilized with two types of surfactants lignin and sodium polycarboxylate respectively. The two vertical walls parallel to the plane (y-z) are subject to constant temperatures ($T_H>T_C$) and constant concentrations ($C_H>C_L$). The other walls are supposed to be impermeable and adiabatic. The dynamic and thermal slips between nanoparticles and the base fluid are negligible. During the process of the natural convection, all the properties of the base fluid and nanoparticles are unchangeable except the density in the buoyancy term in momentum equation, its variations being modeled using Boussinesq approximation. The effects of Soret and Dufour are assumed to be negligible.
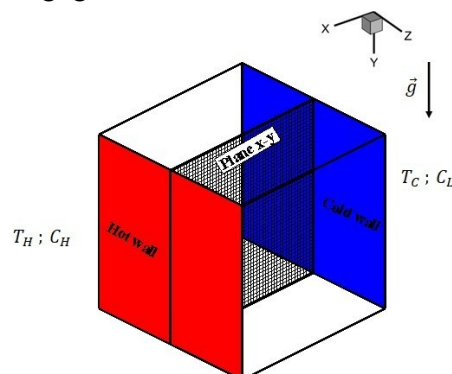


Fig. 1 Schematic of consider problem

### A. Thermophysical properties of carbon nanotubes

For comparison purpose with nanofluids, water which is the base fluid of nanofluids was taken as a reference. The density, the heat capacity, the thermal conductivity, the thermal expansion coefficient and the dynamic viscosity of water are respectively equal to 998.205 kg m$^{-1}$, 4182 J kg$^{-1}$K$^{-1}$, 0.6 W m$^{-1}$K$^{-1}$, 0.00021 K$^{-1}$ and 1.003 mPa s.

In this study, it is considered carbon nanotubes with density of 1800 kg m$^{-3}$ and purity of 90% and 9.2 nm and 1.5 μm in average diameter and length, respectively, dispersed in a mixture of water and surfactant. To improve the dispersion and stability of CNT within water and to reduce clogging and the sedimentation with time, it was used two types of surfactants lignin and sodium polycarboxylate. The volume fraction of carbon nanotubes under consideration ranges from 0.0055 to 0.557%. Density, thermal conductivity and viscosity at 20°C were experimentally determined from well-designed procedures in [2, 3, 6]. All these results are shown in Figure. 2 and they used in the present numerical simulations.

In the following, nanofluids produced with lignin are labeled N2. N3 is used for nanofluids obtained with sodium polycarboxylate as a surfactant.
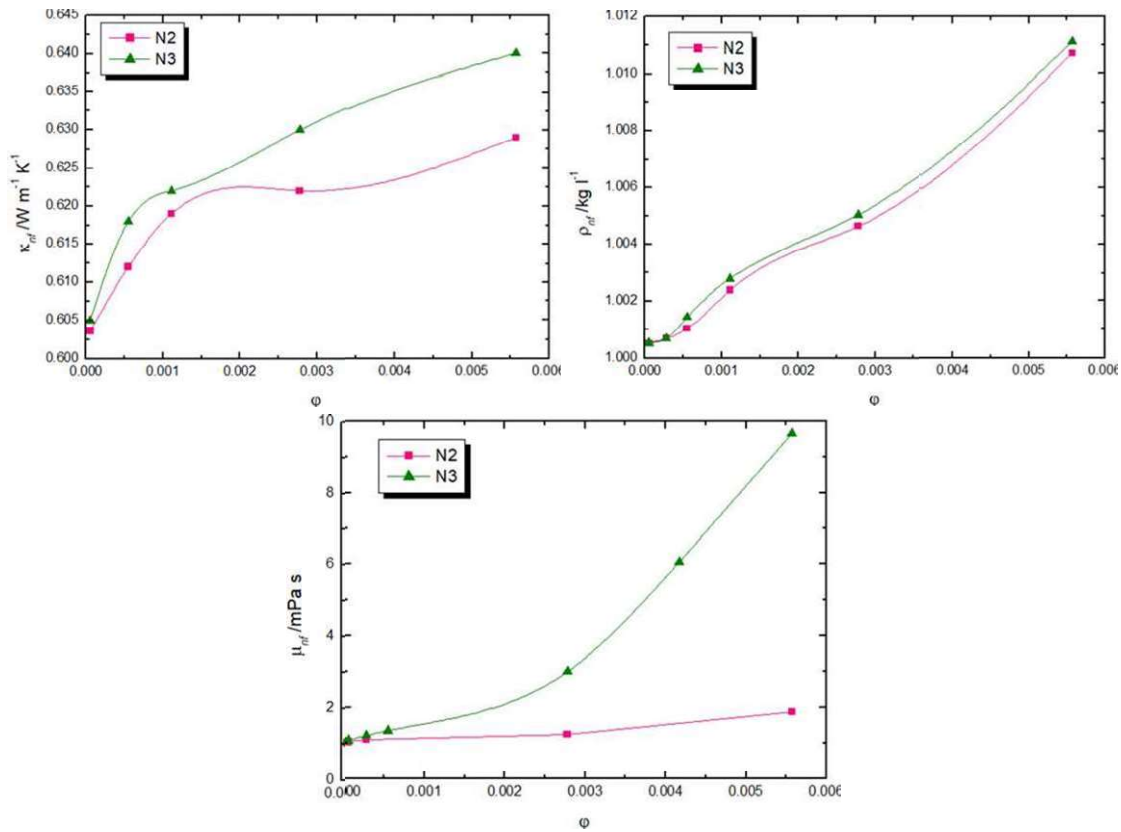


Fig. 1 Thermophysical properties of CNT nanofluids at 20°C with two types of surfactants: thermal conductivity, density and dynamic viscosity

To make easier the implementation of thermophysical data of nanofluids in the numerical simulation and program, the following formulas of thermophysical properties of nanofluids have been adjusted on experimental data.

TABLE I
THERMOPHYSICAL PROPERTIES OF NANOFLUID AT T=20°C

|  | N2 | N3 |
|---|---|---|
| **Density/ kg m$^{-3}$** | $\rho_{nf} = 1\text{?}.4\varphi + 1000$ | $\rho_{nf} = 1\varphi + 1000$ |
| **Thermal conductivity/ W m$^{-1}$ K$^{-1}$** | $k_{nf} = 0.007\text{?}Ln(\varphi) + 0.63$ | $k_{nf} = 0.0072Ln(\varphi) + 0.64$ |
| **Dynamic viscosity/ mPa s** | $\mu_{nf} = 27849.4516\varphi^2 - 9.2088\varphi + 1.05074$ | $\mu_{nf} = 28480\varphi^2 - 82.18\varphi + 1.176$ |

### B. Governing equations

$$\nabla \bar{U} = 0 \qquad (1)$$

$$\frac{\partial \vec{U}}{\partial t} + \left(\vec{U}.\vec{\nabla}\right)\vec{U} = \frac{1}{\rho_{nf}}\vec{\nabla}P + Pr\left(\frac{\mu_{nf}}{\mu_f}\right)\left(\frac{\rho_f}{\rho_{nf}}\right)\nabla\times\vec{U} + RaPr\left(\frac{(\rho\beta_T)_{nf}}{(\rho\beta_T)_f}\right)\left(\frac{\rho_f}{\rho_{nf}}\right)(T - NC) \quad \text{................} \quad (2)$$

$$\frac{\partial T}{\partial t} + \left(\vec{U}.\vec{\nabla}\right)T = \left(\frac{(\rho C_P)_f}{(\rho C_P)_{nf}}\right)\left(\frac{k_{nf}}{k_f}\right)\nabla^2 T \qquad (2)$$

$$\frac{\partial C}{\partial t} + \left(\vec{U}.\vec{\nabla}\right)C = \frac{1}{Le}\left(\frac{(\rho C_P)_{nf}}{(\rho C_P)_f}\right)\left(\frac{k_f}{k_{nf}}\right)\nabla^2 C \qquad (4)$$

In these equations, the dimensionless *Pr*, *Le*, *Ra*, *N* and *K* numbers are respectively defined as

$$Pr = \frac{\nu_f}{\alpha_f}, Le = \frac{\alpha}{D}, Ra = \frac{g\beta_{Tf}(T_H - T_C)L^3}{\nu_f\alpha_f}, N = \frac{\beta_{Cf}(C_H - C_L)}{\beta_{Tf}(T_H - T_C)}$$

The vorticity–vector potential formulation is used in the present study to eliminate the pressure term which is difficult for numerical treatment. The vorticity and vector potential are respectively defined by the following two relations: $\vec{U} = \vec{\nabla}\times\vec{\psi}$ and $\vec{\omega} = \vec{\nabla}\times\vec{U}$

The system of governing equations of the phenomenon is

$$\nabla^2\vec{\psi} = -\vec{\omega} \qquad (5)$$

$$\frac{\partial\vec{\omega}}{\partial t} + \left(\vec{U}.\vec{\nabla}\right)\vec{\omega} - \left(\vec{\omega}.\vec{\nabla}\right)\vec{U} = Pr\left(\frac{\mu_{nf}}{\mu_f}\right)\left(\frac{\rho_f}{\rho_{nf}}\right)\nabla^2\vec{\omega} + RaPr\left(\frac{(\rho\beta_T)_{nf}}{(\rho\beta_T)_f}\right)\left(\frac{\rho_f}{\rho_{nf}}\right)\left(\left[\frac{\partial T}{\partial z},0,-\frac{\partial T}{\partial x}\right] - N\left[\frac{\partial C}{\partial z},0,-\frac{\partial C}{\partial x}\right]\right) \quad (6)$$

$$\frac{\partial T}{\partial t} + \left(\vec{U}.\vec{\nabla}\right)T = \left(\frac{(\rho C_P)_f}{(\rho C_P)_{nf}}\right)\left(\frac{k_{nf}}{k_f}\right)\nabla^2 T \qquad (7)$$

$$\frac{\partial C}{\partial t} + \left(\vec{U}.\vec{\nabla}\right)C = \frac{1}{Le}\left(\frac{(\rho C_P)_{nf}}{(\rho C_P)_f}\right)\left(\frac{k_f}{k_{nf}}\right)\nabla^2 C \qquad (8)$$

*C. Numerical procedure*

The FORTRAN language was used to write the numerical program and solve the mathematical model described above. The governing equations ((5)–(8)) were discretized using the finite volume method based on the central-difference scheme and solved using the successive relaxation iteration scheme. The grids are uniform in all directions, and additional nodes are added on boundaries. A time-step of $10^{-4}$ and spatial mesh of 51×51×51 was used during the numerical simulations We used an Intel core i5 microprocessor for the numerical simulation, with the time of execution was about 7 h for Ra= $10^5$.Hence, the (51×51×51) grid was estimated to be appropriate for the present study at least for Ra $10^5$ since it permits a good compromise between the computational cost (a significant reduction of the execution time) and the accuracy of the obtained results.

## III. RESULTS AND DISCUSSION

Figure 3 shows the variations of average Nusselt number $\overline{Nu}$ and Sherwood number with $\overline{Sh}$ nanoparticles' volume fraction for nanofluid stabilized with Lignin (N2) and sodium polycarboxylate (N3). It is noticed that for the two types of surfactants used, the average Nusselt and Sherwood numbers increase in the area where the value of the volume fraction of nanoparticles is less than its critical value. This is because the thermal performance of water solution is improved by the addition of nanoparticles. Afterwards, the heat and mass transfer rates decrease in the area where the value of the nanoparticles volume fraction is greater than its critical value due to the predominant influence of viscosity over thermal properties. It can be seen also from Figure 3, for the case where the surfactant lignin is used, the average Nusselt and Sherwood numbers are greater than that in the case of the surfactant sodium polycarboxylate employed.
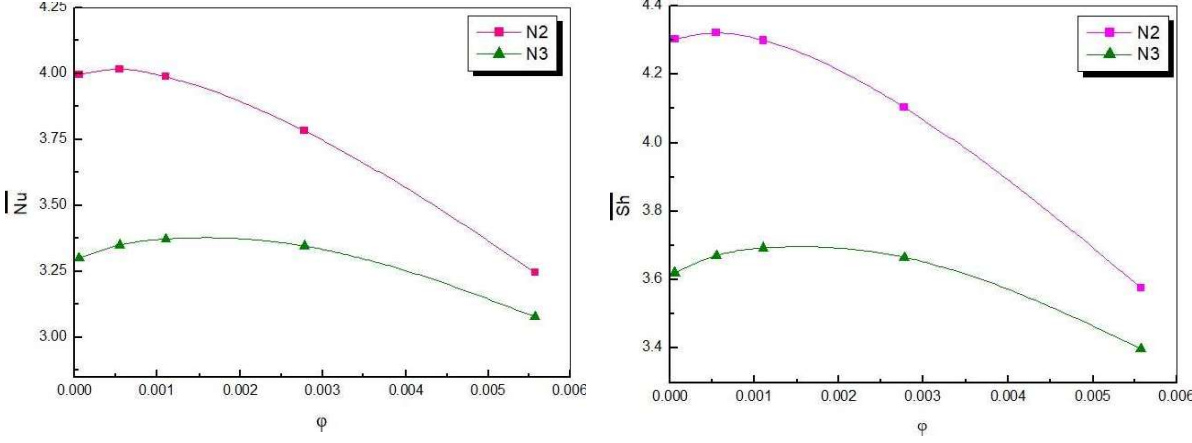


Fig. 3 Variation of Nu and Sh on the hot wall with nanoparticles volume fraction for both N2/N3 nanofluid models for *Ra=10⁵ and N=-0.2*

Figure 4 shows the variations of maximum transverse velocity with the nanoparticle's volume fraction for for nanofluid stabilized with Lignin (N2) and sodium polycarboxylate (N3). Thus, the effects of nanoparticles' volume fraction on the three-dimensional flow are explored. This figure shows, irrespective of the surfactant used, that the maximum transverse velocity improves by increasing φ to the critical value then the velocity tends to decrease. Also, it is clearly noted that N2 have higher transverse velocity compared to N3. For example, for $\varphi=0.0055\%$ it exists a 27.63 % difference between the two cases.
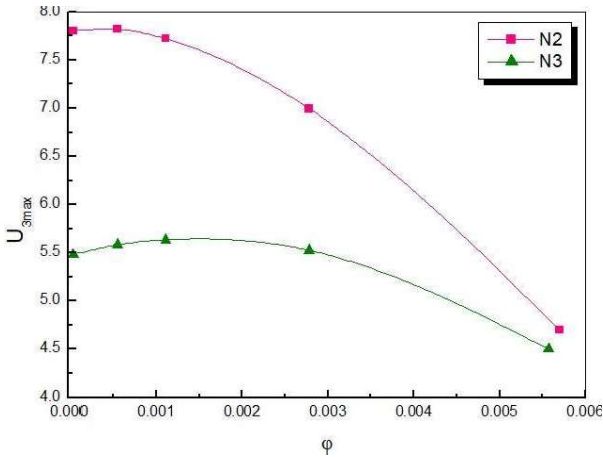


Fig. 4  Variation of maximum of transversal velocity $U_{3max}$ according to the nanoparticles volume fraction for N2 and N3 nanofluid for $Ra=10^5$ and $N=-0.2$

The isocontours of the local Nusselt number determined on the hot wall of the cavity are shown in Figure. 5 for different volume fraction of nanoparticles for stabilized with Lignin (N2) and sodium polycarboxylate (N3). It is clearly noted that the heat transfer decreases from bottom to top. This figure shows that the local Nusselt number varies in the vertical direction (y). Furthermore, in the horizontal direction (z) the isocontours of the local Nusselt number are quite uniform in the central area of the hot wall. It is also noted that the heat transfer increase with the enhancement of nanoparticles volume fraction.
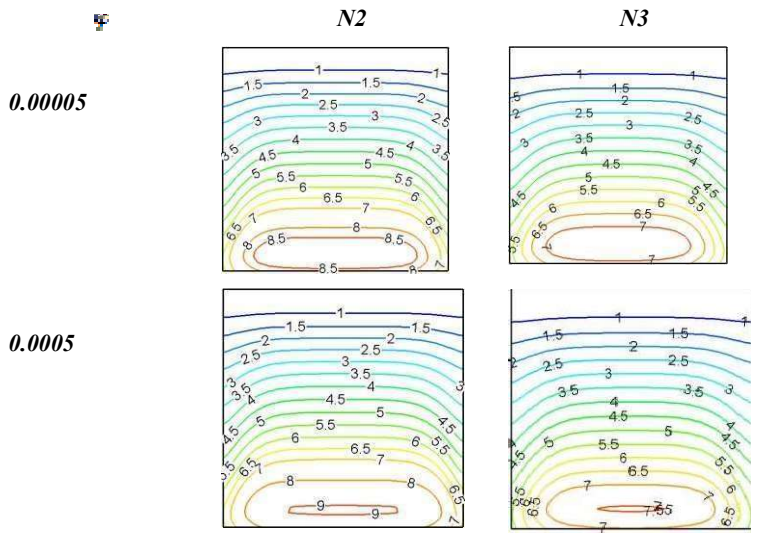


Fig. 5  Distributions of local Nusselt number on the hot wall for some values of nanoparticles volume fraction for both N2 and N3

## IV. CONCLUSIONS

Three-dimensional computational analysis has been performed to investigate the double diffusive natural convection of CNT-water nanofluid stabilized with two types of surfactants lignin and sodium polycarboxylate in a differentially heated cubical enclosure for different governing parameters This numerical work has been performed considering real experimental data for thermophysical properties of nanofluids.        The main findings can be summarized as follow:

- The CNT-water nanofluid stabilized with lignin exhibits more heat and mass transfer rates when compared with CNT-water nanofluid stabilized with sodium polycarboxylate. So using lignin as a surfactant is better than using sodium polycarboxylate.

- The flow strength and the three-dimensional effect of the flow are ameliorated when the nanoparticle volume concentration is less than the critical value and then are deteriorated when it exceed this value for both two types of nanofluids.
- Employing a nanofluid stabilized with Lignin (N2) ameliorates the average Nusselt and Sherwood numbers more than that of sodium polycarboxylate (N3).

REFERENCES

[1] Wen D, Ding Y. Effective thermal conductivity of aqueous suspensions of carbon nanotubes (carbon nanotube nanofluids). J Thermal Heat Transf. 2004; 18: 481-485.

[2] Estellé P, Halelfadl S, Maré T. Thermal conductivity of CNT water based nanofluids: Experimental trends and models overview. Conf Int Ener Tech (Entech'14) At: Istanbul, Turkey. 2014; http://doi.org/10.13140/2.1.4418.5924

[3] Estellé P, Halelfadl S, Maré T. Lignin as dispersant for water-based carbon nanotubes nanofluids:Impact on viscosity and thermal conductivity. Int Com Heat Mass Transf. 2014; 57: 8-12.

[4] Rahman MM, Öztop HF, Steele M, Naim A.G, Al-Salem K, Ibrahim TA. Unsteady natural convection and statistical analysis in a CNT–water filled cavity with non-isothermal heating. Int Com Heat Mass Transf. 2015; 64: 50–60.

[5] Job VM, Gunakala SR, Unsteady MHD Free Convection Nanofluid Flows Within A Wavy Trapezoidal Enclosure With Viscous And Joule Dissipation Effects. Num Heat Transf, Part A. 2015; 59: 1–23.

[6] Estellé P, Mahian O, Maré T, Öztop HF. Natural convection of CNT water-based nanofluids in a differentially heated square cavity. J Thermal Anal Calorim. 2017; 28: 1765–1770.

[7] Minea AA, Estellé P. Numerical study on CNT nanofluids behavior in laminar pipe flow. J Mol Liq. 2018; 271: 281-289.

[8] Kolsi L, Alrashed AAAA, Al-Salem K, Oztop HF, Borjini MN, Control of natural convection via inclined plate of CNT-water nanofluid in an open sided cubical enclosure under magnetic field. Int J Heat Mass Transf. 2017; 111: 1007–1018.

[9] Al-Rashed AAAA, Kolsi L, Kalidasan K, Malekshah EH, Borjini MN, Kanna PR, Second law analysis of natural convection in a CNT-Water nanofluid filled inclined 3D Cavity with incorporated Ahmed Body. Int J Mech Sci. 2017; 130: 399–415.

[10] Rahimi A, Kasaeipoor A, Malekshah EH, Kolsi L. Experimental and numerical study on heat transfer performance of three-dimensional natural convection in an enclosure filled with DWCNTs-water nanofluid. Powd Tech. 2017; 322: 340–352.

[11] Manaa N, Abidi A, Saleel CA, Al Makwash SM, Borjini MN. On Simulation of Double-Diffusive Natural Convection in a Micropolar Nanofluid Filled Cubic Cavity. Heat Transf Eng. 2020; https://doi.org/10.1080/01457632.2020.1756074.

[12] Manaa N, Abidi A, Ahamed SC, Madiouli J, Borjini MN. Three-Dimensional Numerical Analysis on Performance Enhancement of Micropolar Hybrid Nanofluid in Comparison with Simple Nanofluid. Heat Transf Eng. 2020; https://doi.org/10.1080/01457632.2020.1807106

# Assessment of Airborne Particle Pollution from Road Traffic in a High Mobility Urban Site Within the Sousse City Center

Ahmed Komti [#1], Abdessalem Jbara [#*2], Najah Kechiche [*3], Khalifa Slimi [#4]

[#] LESTE Laboratory, National Engineering School of Monastir, University of Monastir, Monastir, Tunisia

[*] Higher Institute of Transportation and Logistics of Sousse, University of Sousse, Sousse, Tunisia

```
Email 1 - ahmedkomti568@gmail.com
Email 2 - j.abdesslem@yahoo.fr
Email 3 - kechiche2000@gmail.com
Email 4 - khalifa_slimi@yahoo.fr
```

*Abstract*— **Despite the implementation of regulatory guidelines across different regions, outdoor air pollution from traffic remains a significant negative externality in transportation. This research focuses on simulating the dispersion of road traffic pollutants in a high-traffic zone situated at the Sousse city. The estimation of road emissions (based on vehicle counts) was conducted using COPEERT Software. The simulations were done using the nested mesoscale meteorology and micro-scale dispersion model system, GRAMM–GRAL V22.03. Buildings situated along the three busiest streets face significant exposure to traffic-related $PM_{2.5}$ and $PM_{10}$ pollutants, with levels peaking at 30 and 20 μg/mt during rush hour. However, outside of peak traffic times, $PM_{2.5}$ and $PM_{10}$ concentration levels decrease, remaining below 17 and 10 μg/mt, respectively. However, the mean $PM_{2.5}/PM_{10}$ ratio exceeds 0.5, (0.58), indicating that PM emissions are primarily attributed to exhaust emissions, tire, and brake wear. Furthermore, the human health risk level is also significant.**

*Keywords*— **Gramm–Gral, Copert, outdoor air pollution, $PM_{2.5}$, $PM_{10}$.**

## I. INTRODUCTION

Air quality stands as the foremost single environmental health risk worldwide. The exposure to ultrafine particles (UFPs) raises significant concerns due to their adverse effects on human health [1]. UFPs are commonly defined as particles with a diameter less than 100 nm [2], and it is widely agreed that these particles contribute the most (approximately 80%) to the total particle number concentration (PNC) [3]; [4]; [5]; [6], while their corresponding mass comprises less than 20% of the total particle mass concentration [7]. Tunisia has reported high yearly average concentrations of $PM_{2.5}$ and $PM_{10}$, which should not exceed 10 and 20 μg/m³ respectively, according to the World Health Organization [8] in 2016. This is a cause of concern as there has been an accelerated growth in emission sources of air pollutants in major Tunisian cities like Tunis, Sousse, and Gabes [9].

Air pollution modeling is pivotal for managing and formulating policies to address air quality issues [10]; [11]. Examples of such studies include those executed by [12] and [13].

Several investigations have been conducted in Tunisia to understand the relationship between meteorology and air quality. One study conducted in Tunis by [14] highlights the significance of temperature inversions, which tend to cause high levels of pollution in the northern regions of the country. The study used multiple linear regressions to determine the statistical dependence between ozone concentrations and weather conditions. Another study by [15] found that certain sea breeze events can impact air quality. Their results indicate that the power plant located near the region of Sousse in east Central Tunisia is responsible for air quality degradation during such circumstances.

Operational Model has been used in a few studies to simulate pollutant concentrations. These models enable the understanding of phenomena, extrapolating measurements to areas without instruments and crucially evaluating operational solutions for emission control and impacts. These solutions may include changes in urban patterns, fuel composition, land use parameters, and the adoption of alternative, intermodal, or cleaner transportation systems. Several models are commonly used to study street pollution, including the Operational Street Pollution Model (OSPM) [16], AERMOD [17], CALINE4 [18], ADMS-Urban [18], SIRANE [19], and Graz Lagrangian model [20]. These models can handle both atmospheric dynamics, such as the transport of pollutants away from their emission sources, as well as complex reactive chemical and photochemical processes. However, not all reactions are systematically included, particularly at the local scale.

The primary aim of this research is to investigate the relationship between outdoor air pollution levels and human exposure, and how they are affected by fluctuations in road traffic and meteorological conditions. The methodology section will provide a detailed description of the chosen urban site and the data collection methods used for traffic and meteorological conditions. Additionally, the GRAL model used for simulating $PM_{10}$ and $PM_{2.5}$ levels at the site will be discussed. The results and discussion section will present and examine the primary findings of the study, including the distribution of outdoor air pollution levels on the roads and their impact on human health. Finally, the conclusion will summarize the key findings and offer useful recommendations.

## II. METHODOLOGY

### A. Site description

The study area falls within the governorate of Sousse, situated along the eastern coast of the country, approximately 150 kilometers north of the Tunis-Carthage International Airport. It is characterized by heavy urban traffic, with a mix of residential areas, schools, cultural centers, banks, and commercial establishments. Figure 1 illustrates the layout, highlighting three main streets: Mohamed Ali Street (M.A), facilitating access from the center of Sousse to neighboring cities such as Monastir, Mahdia, and Sfax; Mohamed V Street, serving as an entrance route to the center of Sousse (M.V); and Habib Thamer Street, connecting the urban harbor agglomeration to the city center (H.T).



| (a) | (b) |
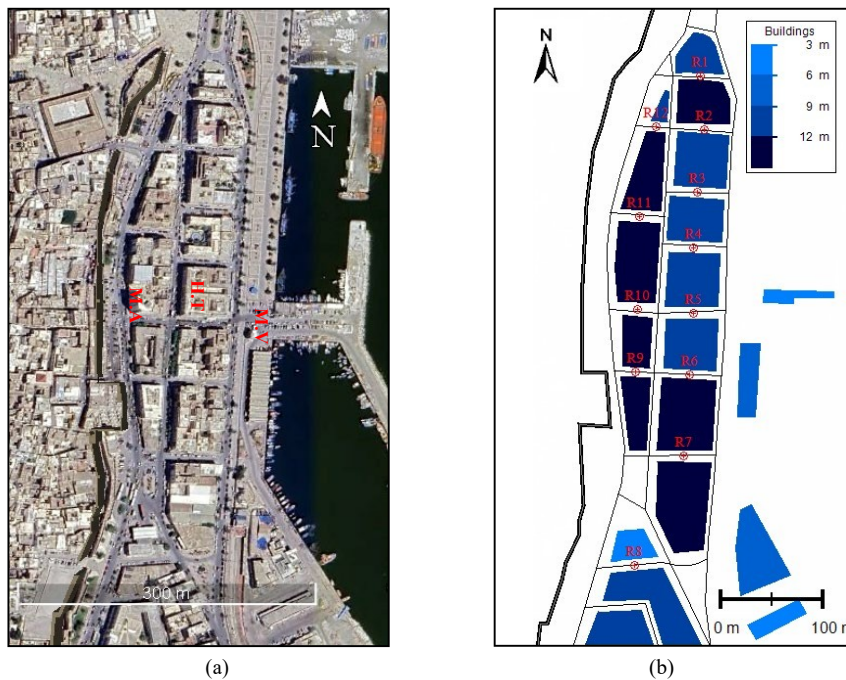
Fig.1: (a) A top view of the study area from Google Earth and (b) a sketch of the same study area with the receptor's locations.

Following the acquisition of Google Maps traffic congestion data, map images were processed to establish a database of traffic congestion around the harbor area. This database enabled the identification of flow intensity along targeted routes, particularly focusing on the busiest routes and times. Fig.2 displays the traffic intensity of the area of study during (a) rush and (b) non-rush hour. With this information, predictions regarding traffic congestion can be generated, aiding individuals in making informed decisions and assisting city planners in formulating more effective infrastructure plans.

It's worth noting that the highest levels of particulate matter (PM) were consistently observed along the three busiest streets in the city: Mohamed Ali ((M.A), Mohamed V (M.V), and Habib Thamer (H.T) streets.

(a)                                         (b)

Fig.2: Traffic intensity on the main roads within the study area during (a) rush hour and (b) non-rush hour.

## B. Study flowchart

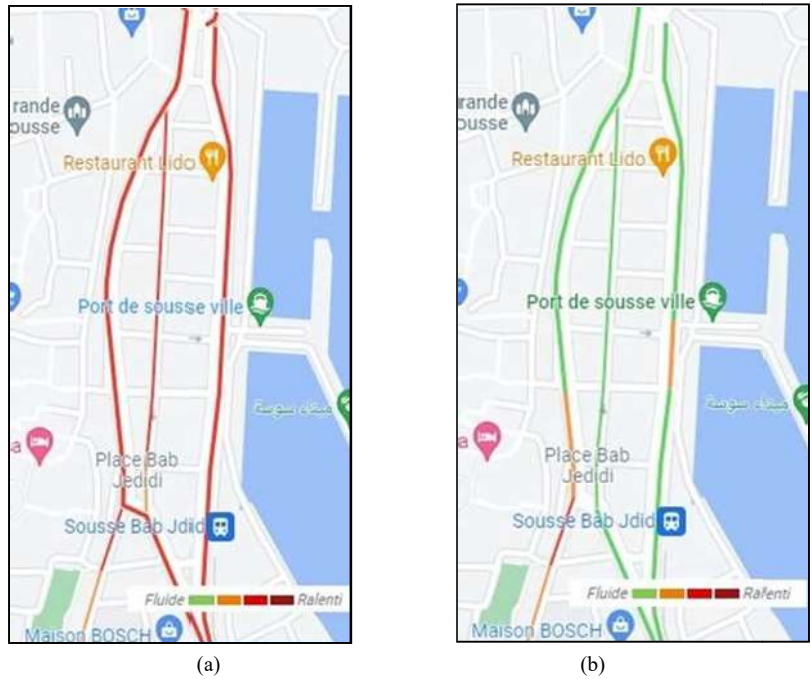Our modeling approach consists of a three-step procedure utilizing the GRAMM/GRAL V22.03. [21], [22]. Firstly, mesoscale air flow, considering topography and land-use effects, is computed by GRAMM for a larger domain centered on the city. Secondly, micro-scale air flow within the city, accounting for the influence of buildings on flow and turbulence patterns, is determined using the GRAL model, driven by GRAMM outputs. Finally, Lagrangian dispersion computations are conducted by the dispersion module of GRAL, guided by the micro-scale wind fields generated by GRAL.

Fig.3 outlines the key steps necessary for simulating the dispersion of road outdoor air pollution within the GRAMM/GRAL V22.03 environments.
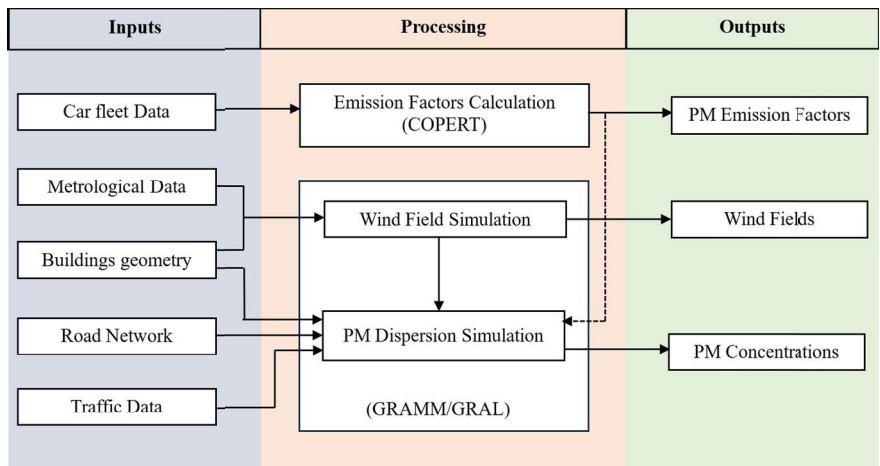


Fig.3: Study flowchart.

## C. Modelling approach

• COPERT (Computer Program to calculate Emissions from Road Transport)

The emission factors for PM2.5 and PM10 particles are calculated using the Computer Program to calculate Emissions from Road Transport (COPERT 5.6.1) [23] package according to the following equation:

$$EF_{i,j,k,l} = EF_{H,i,j,k,l} + EF_{T,i} + EF_{B,i} + EF_{R,i}$$

$EF_{i,j,k,l}$   PM total emission factor (g/km.veh),

$EF_{H,i,j,k,l}$ PM hot emission factor (g/km.veh),

$EF_{T,i}$ PM emission factors of tire (g/km.veh),

$EF_{B,i}$ PM emission factors of brake (g/km.veh),

$EF_{R,i}$ PM emission factors of road surface wear (g/km.veh).

For a heterogeneous vehicle fleet, the average PM emission factor, $EF_m$ *(g/km.veh)* is written as flows:

$$EF_m = \sum_{i,j,k,l} (p_{i,j,k,l} . EF_{i,j,k,l})$$

where, $p_{i,j,k,l}$ denotes the share of vehicles belonging to category *i*, complying with emission standard *j*, using fuel type *k,* and having an engine cylinder or a maximum permissible laden weight *l*.

The emission rate of each road $\dot{m}_r (kg/h/km)$, considered as a linear emission source, is then:

$$\dot{m}_r = \frac{EF_m \, Q_r}{1000}$$

• *GRAMM/GRAL (Graz Lagrangian Model)*

The GRAL system simulates microscale flows around obstacles (e.g., buildings) by solving the Reynolds-Averaged Navier-Stokes equations (RANS):

$$\left| \begin{array}{l} \dfrac{\partial \bar{u}_i}{\partial x_i} = 0 \\ \dfrac{\partial \bar{u}_i}{\partial t} + \bar{u}_j \dfrac{\partial \bar{u}_i}{\partial x_j} = -\dfrac{1}{\rho}\dfrac{\partial \bar{p}}{\partial x_i} + \dfrac{\partial}{\partial x_j}\left[ \mu_t \left( \dfrac{\partial \bar{u}_i}{\partial x_j} + \dfrac{\partial \bar{u}_j}{\partial x_i} \right) - \dfrac{2}{3}\delta_{ij}k \right] \end{array} \right|$$

$\bar{u}_i (i = 1, 2, 3)$ denote the mean wind speed components, ρ the air density, $\bar{P}$ the mean pressure, μt the turbulent viscosity and k the turbulent kinetic energy.

The turbulence model associated with it is (k-ε):

$$\left| \begin{array}{l} \dfrac{\partial k}{\partial t} + \dfrac{\partial (\bar{u}_j k)}{\partial x_j} = \dfrac{\partial}{\partial x_j}\left( \mu_t \dfrac{\partial k}{\partial x_j} \right) + P_m + P_b - \varepsilon \\ \dfrac{\partial \varepsilon}{\partial t} + \dfrac{\partial (\bar{u}_j \varepsilon)}{\partial x_j} = \dfrac{\partial}{\partial x_j}\left( \mu_t \dfrac{\partial \varepsilon}{\partial x_j} \right) + \dfrac{\varepsilon}{k}(1.44(P_m + P_b) - 1.92\varepsilon) \end{array} \right|$$

$P_m$ and $P_b$ are the production terms for turbulent kinetic energy due to shear stresses and buoyancy, respectively, and ε the dissipation rate of turbulent kinetic energy.

The fundamental idea of Lagrangian models is the tracking/tracing of particle trajectories within a 3D flow field. Based on this concept, the particles concentration within volume $dV=dx_1.dx_2.dx_3$ is given by:

$$C = \sum_{i=1}^{R} \frac{m_{p,i}}{dV \, t_a} di$$

$m_{p,i}$ is the mass of one particle, R is the total number of integration steps and $t_a$ is the averaging time for the concentration computation.

TABLE I

SOME PARAMETERS OF THE STUDIED AREA.

| Parameter | Value |
|---|---|
| Latitude | 35°49'31"N |
| Longitude | 10°38'27"E |
| Elevation (above sea level) | 3.51 m |
| Domain dimensions | 376 x 626 m² |
| Building heights | 3-12 m |
| Road widths | 3.5-7 m |

Table 1 presents several parameters of the study area necessary for simulating road outdoor air pollution. These include latitude (35°49'31"N) and longitude (10°38'27"E), elevation above sea level (3.51 m), domain dimensions (376 x 626 m²), building heights (ranging from 3 to 12 m), and road widths (ranging from 3.5 to 7 m). Additionally, Table 2 provides climatic parameters recorded during the two hours under study.

TABLE II

METEOROLOGICAL CONDITIONS DURING THE TWO OBSERVATION PERIODS. (APRIL 10, 2023).

| Parameter | Rush hour (10ʰ00-11ʰ00) | Non-rush hour (14ʰ00-15ʰ00) |
|---|---|---|
| Wind velocity (at 10 m) | 4 km/h | 20 km/h |
| Wind direction | 338° | 100° |
| Temperature | 19,6 °C | 21 °C |
| Atmospheric pressure | 1021,7 hPa | 1019 hPa |
| Relative humidity | 33 % | 21 % |
| Cloud cover | 0/8 oktas | 0/8 oktas |
| Precipitation | 0 mm | 0 mm |

Mesoscale simulations using GRAMM are performed with a horizontal resolution of 2 m × 2 m. The vertical concentration grid consists of 9 layers, each with a thickness of 1 m. Dispersion time is set at 3600 seconds with a maximum of 2000 iterations, while the surface roughness is maintained at 0.8 m. it's worth noting that the background concentration of $PM_{10}$ and $PM_{2.5}$ were respectively 15 and 7.5 µg/m³. Traffic parameters and road emission rates are detailed in Table 3.

TABLE III

CONFIGURATION PARAMETERS FOR GRAMM/GRAL SIMULATIONS

| Parameter | Value | |
|---|---|---|
| Horizontal concentration grid | 2 m × 2 m | |
| Vertical concentration grid | 9 layers, 1 m per layer | |
| Dispersion time | 3600s | |
| Maximum iterations | 2000 iterations | |
| Surface roughness | 0,8 m | |
| Background concentrations (µg.m⁻³) | $PM_{2.5}$ <br> 7.7 | $PM_{10}$ <br> 15 |
| Traffic volumes ranges (veh/h) | Rush hour <br> 155-2410 | Non-rush hour <br> 70-1085 |
| Road's emission rates ranges (kg/h/km) <br> $PM_{2.5}$ <br> $PM_{10}$ | Rush hour <br> 0,0070 – 0,1092 <br> 0,0094 – 0,1467 | Non-rush hour <br> 0,0031 – 0,0492 <br> 0,0042 – 0,0660 |

## III. RESULTS AND DISCUSSION

### A. Wind map analysis

GRAL is nested within GRAMM and operates in diagnostic mode with a 10 m resolution, which contrasts with the approach taken by Berchet et al. [24] where GRAL ran in prognostic mode at a 5 m resolution. In diagnostic mode, the flow field around buildings is computed by interpolating GRAMM wind fields on a fine Cartesian grid and assuming a logarithmic wind profile near walls. Mass conservation is maintained by applying a Poisson equation to establish a pressure field for velocity correction. Conversely, in prognostic mode, the flow is explicitly computed through forward integration of prognostic equations. Wind speeds and directions are measured on a height of 2 m above the ground. Figure 4 (b) depicts the wind map during non-rush hour. During this period, the highest wind speeds were also observed between buildings along Mohamed Ali, Mohamed V, and Habib Thamer streets. However, compared to rush hour, wind speeds were reduced and did not exceed 2 m/s.
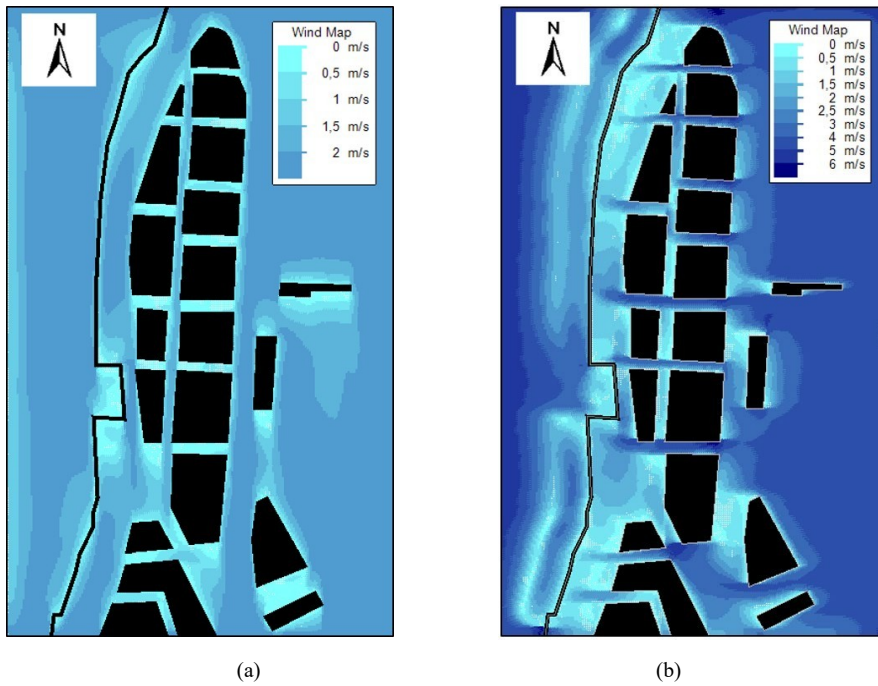
(a)                                    (b)

Fig.4: Wind maps at 2m above ground level during (a) rush hour and (b) non-rush hour.

In Figures 5 (a) and (b), we observe significant differences in spatial patterns of total $PM_{10}$ concentrations between rush and non-rush hours, with maximum levels reaching 30 and 17 ug/m3, respectively. Higher concentrations were generally noted in buildings situated along both sides of the three busiest streets. Notably, in Figure 6 (a) and (b), disparities in $PM_{2.5}$ concentrations between rush and non-rush hours were also significant, with maximum values reaching 20 and 10 ug/m3, respectively. In both scenarios, a considerable proportion of buildings were exposed to outdoor air pollution levels very close to the new EPA standard thresholds of 40 and 25 ug/m3. It's worth emphasizing that air pollution from road traffic exceeding these levels is associated with adverse health effects [25].
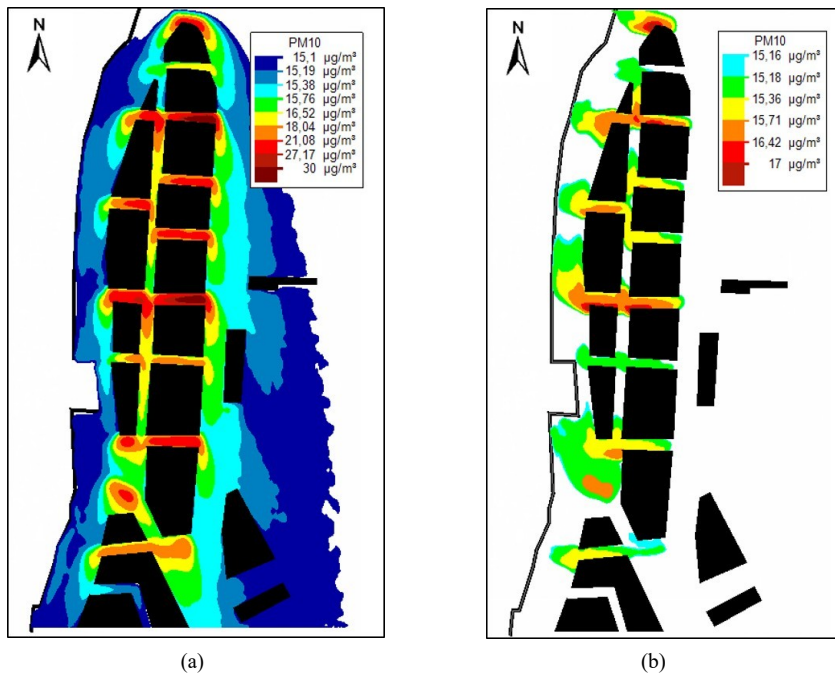


(a)                                    (b)

Figure 5: $PM_{10}$ iso-concentration maps at 2m above ground level for (a) rush hour and (b) non-rush hour.
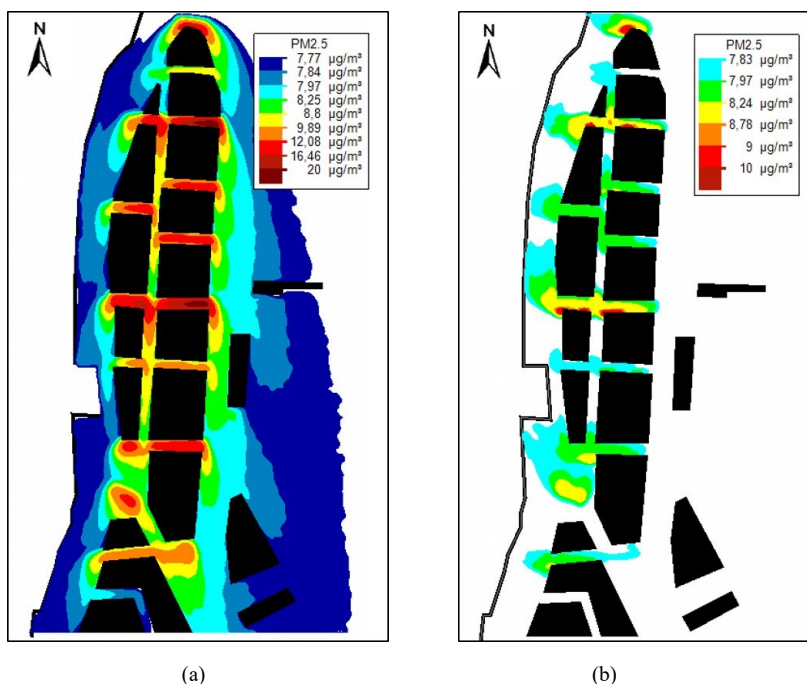
(a)                                         (b)

Figure 6: $PM_{2.5}$ iso-concentration maps at 2m above ground level for (a) rush hour and (b) non-rush hour.

Figure 7 (a) and (b) showcases histograms illustrating the levels of road air pollution exposure during rush and non-rush hours. It is apparent that the most notable disparities in concentration between rush and non-rush hours for both $PM_{10}$ and $PM_{2.5}$ were observed at receptor 2, where the maximum levels reached 17 and 13 ug/m3, respectively. Moreover, individuals residing in close proximity to receptor 2 are subjected to higher levels of road air pollution compared to other residents.
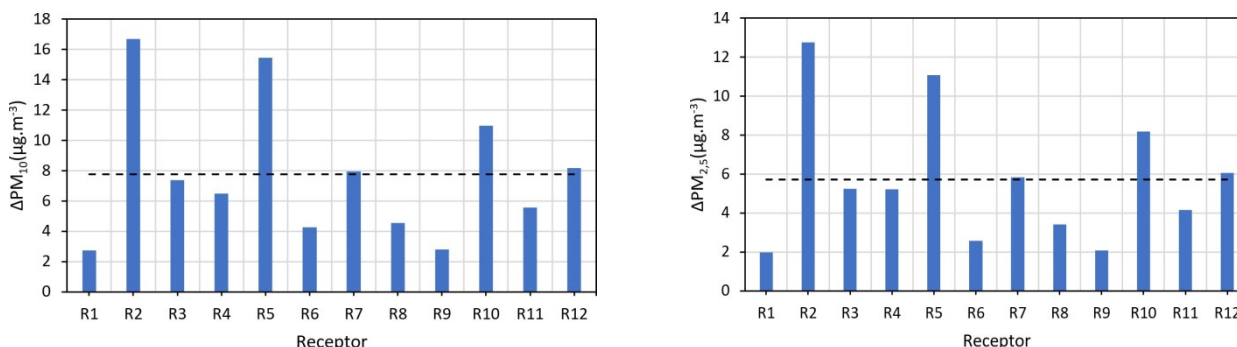


Figure 7: (a) Differences in PM10 concentrations and (b) PM2.5 concentrations between rush and non-rush hours at all receptors.

Figure 8 displays the $PM_{2.5}/PM_{10}$ ratios at 2 meters above ground level for each receptor. High $PM_{2.5}/PM_{10}$ ratio values are typically associated with vehicle-related emission sources, including exhaust emissions and tire and brake wear, while lower ratios are linked to increased resuspension of road dust due to wearing course abrasion and poor road conditions. Moreover, a high ratio between fine and coarse particulate matter indicates a heightened human health risk level, especially for children, as fine particles ($PM_{2.5}$) are considered more hazardous and can penetrate deeply into the respiratory system. In this instance, the mean $PM_{2.5}/PM_{10}$ ratio exceeds 0.5 (0.58), indicating that PM emissions are primarily attributed to exhaust emissions, tire, and brake wear. Additionally, the human health risk level is deemed significant.

Figure 8: PM$_{2.5}$/PM$_{10}$ ratio for all receptors (rush hour).

## IV. CONCLUSIONS

In this paper, we assessed the outdoor particulate pollution from road traffic in a high-mobility urban area in the Sousse city center during traffic rush and non-rush hours. Initially, we provide a description of the study site an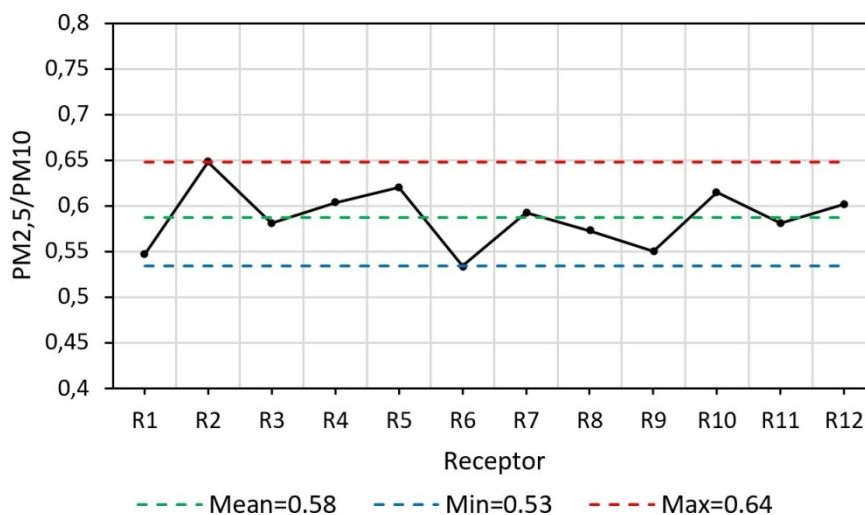d essential parameters required for simulating airborne traffic dispersion. Subsequently, emission factors for each road segment are determined using the Computer Program to Calculate Emissions from Road Transport (COPERT 5.6.1). Following this, the outputs from COPERT 5.6.1 are utilized by the Graz Lagrangian Model (GRAMM/GRAL V22.03) to simulate PM dispersion and analyze the impact of traffic volume variability on particulate matter (PM) levels. Consequently, the following conclusions are drawn:

- The spatial distributions of PM$_{10}$ and PM$_{2.5}$ concentrations are strongly related to road traffic patterns and atmospheric conditions.

- The street canyons confine pollutants, leading to the stagnation of particles around buildings.

- The average reductions in PM$_{10}$ and PM$_{2.5}$ concentrations are 7.75 µg.m-3 and 5.71 µg.m-3, respectively, when the total traffic volume is reduced by 7976 veh/h between rush and non-rush hours.

- Effective traffic management has the potential to decrease particle pollution levels, especially during rush hours.

## ACKNOWLEDGMENT

## REFERENCES

[1] Atkinson, R.W., Fuller, G.W., Anderson, H.R., Harrison, R.M., Armstrong, B., 2010.Urban ambient particle metrics and health: a time-series analysis. Epidemiology 21, 501-511.

[2] Morawska, L., Thomas, S., Bofinger, N., Wainwright, D., Neale, D., 1998. Comprehensive characterization of aerosols in a subtropical urban atmosphere: particle size distribution and correlation with gaseous pollutants. Atmos. Environ. 32,2467-2478.

[3] Heal, M.R., Kumar, P., Harrison, R.M., 2012. Particles, air quality, policy and health.Chem. Soc. Rev. 41, 6606e6630.

[4] Kumar, P., Robins, A., Vardoulakis, S., Quincey, P., 2011b. Technical challenges in tackling regulatory concerns for urban atmospheric nanoparticles. Particuology 9, 566-571.

[5] Morawska, L., Ristovski, Z., Jayaratne, E.R., Keogh, D.U., Ling, X., 2008. Ambient nano and ultrafine particles from motor vehicle emissions: characteristics, ambient processing and implications on human exposure. Atmos. Environ. 42, 8113-8138.

[6] Charron, A., Harrison, R.M., 2003. Primary particle formation from vehicle emissions during exhaust dilution in the roadside atmosphere. Atmos. Environ. 37, 4109-4119.

[7] Kittelson, D.B., 1998. Engines and nanoparticles: a review. J. Aerosol Sci. 29, 575-588.

[8] WHO (2016) "World Health Statistics - Monitoring Health for the SDGs, pp. 1-121.

[9] Bouchlaghem, K. and Nsom, B. (2012) 'Effect of AtmosphericPollutants on the Air Quality in Tunisia', The Scientific WorldJournal. https://doi.org/10.1100/2012/863528.

[10] Karaca, F., Nikov, A. and Alagha, O. (2006) 'AirPolTool - A WEB-BASED TOOL FOR ISTANBUL Air Pollution Forecasting AndControl', Int. J. Environment and Pollution, vol. 28, pp. 3-4. https://doi.org/10.1504/IJEP.2006.011214.

[11] Saffarini, G. and Odat, S. (2008) 'Time Series Analysis of Air Pollution in Al-Hashimeya Town Zarqa, Jordan', Jordan Journalof Eart and Environmental Sciences, vol. 1, pp. 63-72.

[12] Ayari, S., Nouira, K. and Trabelsi, A. (2012) 'A Hybrid ARIMA andArtificial Neural Networks Model to Forecast Air Quality in UrbanAreas: Case of Tunisia', Advanced Materials Research, vol. 518-523, pp. 2969-2979. https://doi.org/10.4028/www.scientific.net/AMR.518-523.2969

[13] Calzolai, G., Nava, S., Lucarelli, F., Chiari, M., Giannoni, M., Becagli, S., Traversi, R., Marconi, M., Frosini, D., Severi, M., Udisti,R., Di Sarra, A., Pace, G., Meloni, D., Bommarito, C., Monteleone,F., Anello, F. and Sferlazzo, D.M. (2015) 'Characterization of PM10sources in the central Mediterranean', Atmospheric Chemistryand Physics, vol. 15, pp. 13939–13955. https://doi.org/10.5194/acp-15-13939-2015

[14] Melki, T. (2007) "Inversions Thermiques Et Concentrations De Polluants Atmospheriques Dans La Basse Troposphere De Tunis", Climatologie, vol. 4. https://doi.org/10.4267/climatologie.773.

[15] Bouchlaghem, K., Nsom, B., Latrache, N. and Hadj Kacem, H. (2009) 'Impact of Saharan dust on PM 10 concentration in the Mediterranean Tunisian coasts', Atmospheric Research, vol. 92, pp. 531–539. https://doi.org/10.1016/j.atmosres.2009.02.009.

[16] E. Konstantinos Kakosimos, Ole Hertel, Matthias Ketzel, Ruwim Berkowicz, Environ. Chem. 7 (2010) 485– 503. Doi:10.1071/EN10070

[17] US EPA "User's guide for the AMS/EPA regulatory model – AERMOD", Office of Air Quality Planning and Standards, Emissions Monitoring and Analysis Division Research Triangle Park, North Carolina, 27711 (2004).

[18] P.E. Benson, CALINE 4: A dispersion model for predicting air pollutant concentrations near roadways. FHWA-CA-TL-84-15, California Department of Transportation, Sacramento, CA (USA) (1984).

[19] CERC, "Atmospheric Dispersion Modelling System (ADMS 4) User Guide version 4.0" (2007).

[20] Lionel Soulhac, Pietro Salizzoni, F.X. Cierco, Richard Perkins, Atmospheric Environment 45 (2011) 7379- 7395.

[21] Almbauer, R. A., Oettl, D., Bacher, M., and Sturm, P. J.: Simulation of the air quality during a field study for the city of Graz, Atmos. Environ., 34, 4581–4594, https://doi.org/10.1016/S1352- 2310(00)00264-8, 2000.

[22] Oettl, D.: Quality assurance of the prognostic, microscale wind□field model GRAL 14.8 using wind-tunnel data provided by the German VDI guideline 3783-9, J. Wind Eng. Ind. Aerod., 142, 104–110, https://doi.org/10.1016/j.jweia.2015.03.014, 2015b.

[23] COPERT 5 Computer programme to calculate emissions from road transport, www.copert 116 versions 5.6.1.org, EMISIA / EEA COPERT 5, (2021).

[24] Berchet, A., Zink, K., Muller, C., Oettl, D., Brunner, J., Emmenegger, L., and Brunner, D.: A cost-effective method for simulating city-wide air flow and pollutant dispersion at building resolving scale, Atmos. Environ., 158, 181–189, https://doi.org/10.1016/j.atmosenv.2017.03.030, 2017b.

[25] Victoria, Environment Protection Authority. PM2.5 Particles in the Air | Environment Protection Authority Victoria. https://www.epa.vic.gov.au/for-community/environmental-information/air-quality/pm25-particles-in-the-air.

# Determination of anisotropic elastic parameters of rock used in the underground radioactive nuclear storage from biaxial testing of hollow cores using the CSIRO Hi cell.

Abdelmonem Ben Ouanas, Yann Gunzburger, Franz Lahaie,

*ENAU Ecole Nationale d'Architecture et d'Urbanisme – Université de Carthage – Tunis, Tunisia.*

*Université de Lorraine, GeoRessources UMR 7359, Campus Artem, CS 14234, F-54042 Nancy, France.*

*INERIS National Institute for Industrial and Environmental Safety, Nancy, France.*

abdelmonem.benouanas@enau.ucar.tn

yann.gunzburger@univ-lorraine.fr

franz.lahaie@ineris.fr

*Abstract*—**The determination of the elastic parameters of transversely isotropic rocks is typically performed in the laboratory, using uniaxial or triaxial tests on small cylindrical samples prepared with different orientations relative to the plane of transverse isotropy. As shown in this study, a possible alternative is the in situ biaxial testing of hollow rock cylinders. This method has already been applied for many years in the case of isotropic rocks, to determine the elastic parameters necessary for calculating the in situ stress tensor from an overcoring test. It consists of placing the instrumented hollow rock cylinder recovered after overcoring in a Hoek-Franklin pressure chamber and submitting the core to biaxial loading-unloading cycles. Based on the recorded stress-strain curves, the Young's modulus and Poisson's ratio of the rock core may then be easily determined from the elastic solution for a thick pipe under uniform external pressure. In the case of a transversely isotropic rock, various analytical or semi-analytical solutions have also been proposed and are briefly reviewed in this paper. However, these solutions are not fully satisfactory since they rely on various ▢ occasionally major ▢ simplifications. Hereafter, we present two alternative approaches for determining the elastic parameters of a transversely isotropic rock core equipped with a CSIRO Hi strain cell, based on a biaxial test. The first one is based on the numerical modelling of the test. The second one relies on an analytical calculation. These methods are both illustrated trough the interpretation of biaxial tests performed on argillite rock samples from the Tournemire experimental station (France). The anisotropy ratio of the investigated argillite was found to be particularly weak compared to the ratio determined from laboratory tests and a possible origin of this difference is discussed.**

**Keywords— Biaxial test, Elastic parameters, Transverse isotropy, CSIRO Hi cell, Hoek-Franklin pressure chamber, Numerical modelling.**

## I. INTRODUCTION

Simple stress and strain calculations under the assumption of linear elasticity are very often the first step of any surface or underground excavation design in rock. They require the knowledge of the elastic parameters of the rock, which are 2 for an isotropic material and 5 for a transversely isotropic one. In the second case, the determination of the elastic parameters classically relies on uniaxial or triaxial tests performed on small rock cylinders prepared with different orientations relative to the plane of transverse isotropy. This technique requires sample preparation and thus is submitted to size effects and sampling artefacts. It must also be performed in the laboratory, i.e. in conditions different from those of the site (e.g., hygrometry, stress history). A possible alternative technique is the in situ biaxial testing of larger hollow rock cylinders. This method has been applied for many years to determine the elastic parameters required for estimating the in-situ stresses from an overcoring test, but mostly in the case of isotropic rocks.

The overcoring test is one of the most popular methods for in situ rock stress determination (Amadei & Stephansson, 1997). It consists of measuring the strains that develop at the wall of a small-diameter borehole (pilot hole) when this hole it is relieved from the surrounding stress field by overcoring, using a larger-diameter drill bit

(Fig.1). The pilot hole may be instrumented with various types of strain cells, such as the triaxial CSIRO Hi cell (see Worotnicki, 1993 and Fig.2) that will be considered in this study. Assuming a linear elastic behaviour for the rock, in situ stresses may then be determined from the strains measured during the overcoring process. This inversion requires the values of the rock elastic parameters, which are usually determined from biaxial testing of the retrieved hollow rock core.
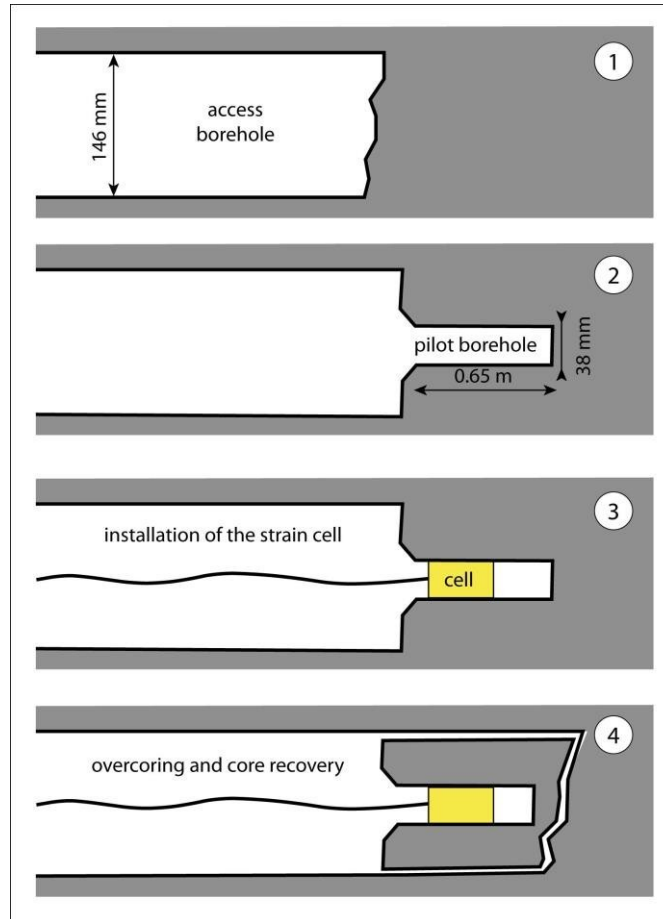


Fig. 1 Scheme of the overcoring protocol. Here the diameter of the overcoring bit is 146 mm and the diameter of the pilot hole is 38 mm, which is the suited diameter for the CSIRO cell.
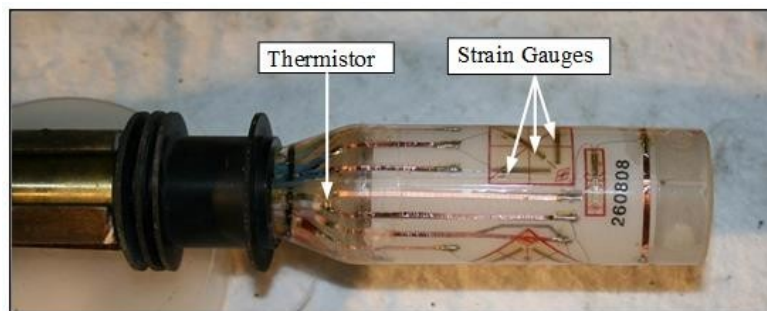


Fig. 2. CSIRO Hi cell. The CSIRO Hi cell is a hollow epoxy cylindrical inclusion of 0.5 mm thickness, at the inner surface of which are laid 12 strain gauges with different orientations: 2 axial, 5 orthoradial and 5 inclined at 45° or 135° with respect to the cell axis. The cell is settled in a 38 mm diameter borehole and coupled to the borehole wall by extrusion of an epoxy glue in the 1 mm annular space between the cell and the rock. Once the glue has hardened, it normally has the same mechanical properties as the CSIRO cell epoxy shell. This way the glue and the shell may be modelled as a single epoxy layer of 1.5 mm.

The biaxial test consists of placing the instrumented hollow rock cylinder retrieved after overcoring in a Hoek-Franklin pressure chamber (Fig. 3) and submitting it to uniform external pressure through several loading-unloading cycles. In the case of isotropic rock, the elastic parameters of the rock core (its Young's modulus and Poisson's ratio) can be easily derived from the recorded pressure-strain curves by using the analytical solution for an elastic thick pipe, eventually modified to take into account the stiffness of the CSIRO Hi 12 cell placed into the core. In the case of transversely isotropic rock, several analytical or semi-analytical solutions for determining the 5 elastic parameters from a biaxial test have been proposed. These solutions are not fully satisfactory since they rely on various ☐ occasionally major ☐ simplifications.



Fig. 3. (a) Hoek-Franklin pressure chamber. (b) Biaxial loading/unloading cycle with external pressure P. The green layer between the strain cell and the rock core represents the bounding glue.
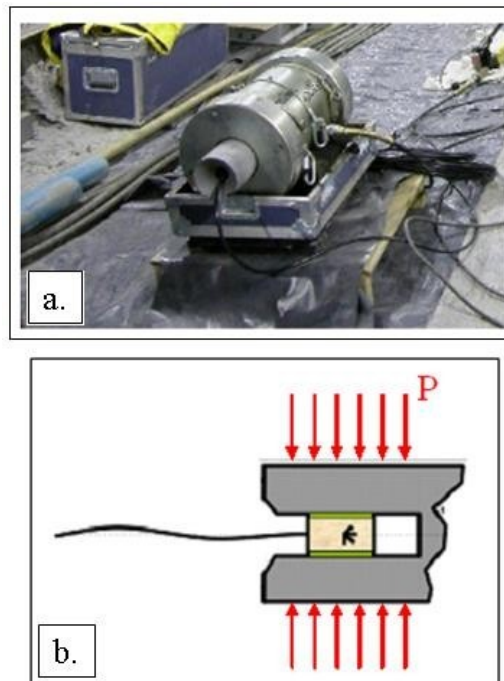
In this paper, we first provide the reader with a brief state of the art regarding biaxial test interpretation as well as the issue of stress and strain that develop within the hollow rock core during such a test, in the case of both isotropic and anisotropic rocks. Then, we present two new methods for the determination of the elastic parameters of transversely isotropic rocks from biaxial tests performed with a CSIRO Hi cell. The first method is based on the 3D numerical modelling of a biaxial test. The second relies on an analytical solution developed *ad hoc*. Both methods are theoretically applicable for any orientation of the rock core with respect to the plane of transverse isotropy even though, for simplicity, we only present hereafter the case where the core axis is parallel to the plane of isotropy. These methods are then illustrated through tests performed on argillite from the Tournemire experimental station, France. The anisotropy ratio of the investigated rock was found to be particularly weak compared to the ratio determined from laboratory tests. A possible origin of this difference is discussed.

## II.    STATE OF THE ART ON THE INVERSION METHODS FOR BIAXIAL TESTS

Among available methods for the inversion of biaxial tests, one may distinguish between those applicable only for isotropic rocks only and those that may also be used for transversely isotropic rocks. To our knowledge, only two of theses methods are commonly used in practice: the one proposed by Duncan-Fama & Pender (1980) and Worotnicki (1993) for isotropic rocks and the one developed by Nunes (1997) for transversely isotropic rocks.

*A* METHODS APPLICABLE ONLY TO ISOTROPIC ROCKS.

In the case of a hollow core of isotropic rock, the elastic parameters of the material (namely its Young's modulus $E$ and Poisson's ratio $\nu$) can easily be derived from the strains measured at the inner wall of the core when a uniform pressure is applied on its outer surface. For this purpose, the classical analytical solution for an elastic thick pipe (Timoshenko & Goodier, 1951) is used.

Worotnicki & Walton (1976) and Worotnicki (1993) have introduced correcting factors to take into account the stiffness of the CSIRO Hi 12 cell placed into the core, as well as that of the epoxy (glue) layer that couples the cell to the borehole wall. The cell and the glue are generally assumed to have the same mechanical properties and are designated as "the inclusion". An analytical formulation is available, that relates the deformations $\varepsilon_\theta$, $\varepsilon_z$ and $\varepsilon_{\theta z}$ recorded respectively on the orthoradial, axial and inclined strain gauges of the CSIRO cell, to the far field stress state $\sigma_0$ at the infinite:

$$E\varepsilon_\theta = \left( \sigma_{x0} + \sigma_{y0} \right) \left( K_1 \right) - \nu \left( \sigma_{y0} \right) \left( K_2 \right) - \left( 2\nu - 1 \right)\rho^2 \left[ \left( \sigma_{x0} - \sigma_{y0} \right)\cos 2\theta + 2\sigma_{xy0} \sin 2\theta \right] K_4 \left( \rho \right)$$

$$E\varepsilon_z = \sigma_{x0} - \nu \left( \sigma_{x0} + \sigma_{y0} \right)$$

$$E\varepsilon_{\theta z} = 4\left(1+\nu\right)\left[ \sigma_{yz0} \cos \theta - 2\sigma_{xz0} \sin \theta \right] K_3 \left( \rho \right)$$

where $\rho$ stands for the ratio between the radial position of strain gauges and the radius of the pilot hole (inner radius of the core). $K_1(\rho)$, $K_2(\rho)$, $K_3(\rho)$ and $K_4(\rho)$ represent the four correction factors, that depend on the external and internal radii of the inclusion and on the elastic properties of the rock and the inclusion. The expressions of these correction factors are given by Duncan-Fama & Pender (1980) in the case when the external radius of the core is considered as much larger than the inner radius. Less restrictive expressions are given by Worotnicki (1993) when no assumption is made on the external radius and are the most commonly used. For a biaxial test, $\sigma_0$ corresponds to the external pressure $P$ applied on the outer surface of the rock core.

*B* METHODS THAT MAY BE USED ALSO FOR TRANSVERSELY ISOTROPIC ROCKS.

When the rock is transversely isotropic, several analytical or semi-analytical relationships between the strains measured inside the hollow core and the external pressure applied on it may be found in literature. They differ from each other in the simplifying hypotheses that are used:
- The effect of the inclusion may neglected, which is ,
- the external radius of the core may be assumed to be much larger than the inner radius,
- strains may me considered to be measured at the inner borehole wall and not within the inclusion, which implies the ignorance of the epoxy (glue) layer coupling the strain cell to the core inner wall of the core,
- the core axis may be considered to be parallel or perpendicular to plane of transverse isotropy of the rock,
- the stress distribution within the rock core may be assumed to be identical to the one calculated for an isotropic rock (Nunes, 2002; Hakala & Sjöberg, 2006).

These relationships may be used for determining the 5 elastic parameters of the material (namely its two Young's moduli E and E, its two Poisson's ratios ν and ν , and its shear modulus G) from a biaxial test. For a moderate anisotropy, the procedure presented in the previous section may nevertheless allow to approach the transverse isotropic properties of the rock, as discussed in section IV.

Hereafter, we provide a brief review of the available relationships, that are also summarized in table 1.

Nunes (1997, 2002) presents a new analytical method for determining the elastic constants and orientation of anisotropy from a biaxial test on a hollow core equipped with a CSIR cell. Unlike the CSIRO cell gauges, the CSIR cell gauges are directly bonded to the inner wall of the core. The analytical formulation is based on the following assumptions: (a) the core is assumed to be continuous, statistically homogeneous, isotropic or transverse isotropic (b) the portion of the rock under the CSIR rosettes is assumed to be continuous, statistically homogeneous, isotropic or transverse isotropic (c) the anisotropy plane of the core may have any orientation, (d) the elastic constants are represented by the elastic modulii $E_1$ and $E_2$ (respectively, normal and parallel to the bedding plane) and two

Poisson's ratios $\square_{12}$ and $\square_{23}$. The shear modulus of the anisotropy plane $G_{12}$ is supposed to follow the empirical expression of Saint-Venant (1863): $G_{12} = E_1E_2 / (E_1 + (1+2\square_{12})E_2)$, (e) the distribution of stresses in the anisotropic core is determined from isotropic linear elasticity (i.e. the traditional Lamé's solution of the hollow cylinder). According to the author, and based on the theoretical work of Lekhnitskii (1968) and numerical modelling of biaxial tests by finite elements approach, this assumption is reasonable in the case of stiff materials (f) the measured strains are assumed to be punctual, i.e. the length of the gauge is neglected.

The orientation of the anisotropy and the remaining four elastic properties ($E_1$, $E_2$, $\square_{12}$ and $\square_{23}$) are determined from the extrema of sinusoidal curves (the concept has already been used by Gonano and Sharp 1983, for sandstone cores with visible planes of symmetry) of tangential, axial and shear strains expressed in terms of those measured by the three CSIR rosettes. The details of the expressions can be consulted in Nunes (2002). This methodology has been implemented in an inversion software by Hakala and Sjöberg (2006). This software is, to our knowledge, the only operational tool, aimed to the inversion of biaxial tests carried out on anisotropic (transverse isotropic) cores. In our inversion program (section 4.2), we use the methodology proposed by Nunes (2002) to obtain a first approximation of the transverse isotropic elastic constants.

According to Worotnicki, who reviewed the results of more than 200 mechanical and dynamic tests on various types of rocks, the igneous rocks (granite, sandstone, basalt, etc..) comply with the assumption of Saint-Venant. On the other hand, this is not the case of clay and pelitic rocks, such as slate or shale, as the true shear modulus $G_{12}$ can be up to 2 to 3 times lower than that estimated by Saint-Venant with an upper bound of the ratio $G_{12}/G_{StVenant}$ ranging between 0.85-0.90. Laboratory tests performed on the Tournemire argillites (Rejeb et al. 2007) yielded the following values 2.62 and 0.65 respectively for $E_2/E_1$ and $G_{12}/G_{StVenant}$.

Finally, the hypothesis of isotropy for the stress distribution around the inner wall of the core in biaxial compression can be questionable. Indeed, the general solution (in terms of stresses) of a hollow cylinder subjected to internal and/or external pressure proposed by Lekhnitskii (1968) shows that this distribution is not uniform. Similarly, the analytical solutions of stresses of an infinite cylindrical hole proposed by Berry in 1968 (reported by van Heerden 1983) also show that the state of stresses is far from isotropic. Numerical examples from the general semi-analytical solutions developed by Amadei 1983 (supported or unsupported cylindrical hole in an infinite medium subjected to an anisotropic initial stress state) indicate some sinusoidal profiles of the induced stresses. Except the case where the borehole is oriented perpendicular to the plane of stratification, the stress distribution is uniform when the initial state of stress is isotropic.

### III. STATE OF THE ART ON THE DISTRIBUTION OF STRESSES AND STRAINS WITHIN A HOLLOW CORE WITH A FINITE OR INFINITE EXTERNAL RADIUS

On the basis of the general theory of elasticity of anisotropic media developed by Lekhnitski (1963), several authors have proposed analytical solutions for simplified problems (transverse isotropic material and drill core oriented parallel or perpendicular to the plane of isotropy). These are: Berry and Fairhurst (1966) cited by Berry (1968), Van Heerden (1983) or Worotnicki (1993). Van Heerden extends the work of Berry (1968) by reformulating the relationship between stresses and strains in SIR or CSIRO cells (without glue) during an overcoring operation and when drilling is oriented parallel or perpendicular to the bedding plane. Based on the work of Lekhnitskii, Amadei (1983) gives numerical solutions (using Fourier series developments and assuming a generalized plane strain formulation) expressing the six components of the far-field in situ stress tensor with respect to the strains recorded on the borehole wall or in the inclusion.

Table 1 summarizes the main assumptions considered in the operational formulations found in the literature.

Table 1 - Distribution of stresses and/or strains around a borehole or a rock core drilled in isotropic or anisotropic rock (literature review)

| Authors | Outer radius of the core cylinder | Inclusion (glue) taken into account | Location where [σ] and/or [ε] are calculated | Mechanical behaviour of the rock | Orientation of borehole/core with respect to anisotropy[4] |
|---|---|---|---|---|---|
| Duncan-Fama 1980 | Infinire | Yes | In the inclusion (CSIRO) | Isotropic | - |
| Worotnicki 1993 | Finite | Yes | In the inclusion (CSIRO) | Isotropic | - |
| Nunes 2002 | Finite | No | Borehole wall (CSIR) | Transverse isotropic | Any |
| Berry 1968[a], Van Heerden 1983[a] | Infinite | No | Borehole wall (CSIR) | Transverse isotropic | Parallel or perpendicular to the bedding plane |
| Amadei 1983[1] [a] | Infinite | Yes | In the inclusion (CSIRO) | Isotropic, transverse isotropic or orthotropic | General (any orientation) |
| Amadei 1983[1] [a] | Infinite | No | Borehole wall | Isotropic, transverse isotropic or orthotropic | General (any orientation) |
| Worotnicki 1993[3] [a] | Infinite | Yes | Borehole wall | Transverse isotropic | Parallel or perpendicular to the bedding plane |
| Worotnicki 1993[2] [b] | Finite | Yes | Borehole wall | Transverse isotropic | Parallel to the bedding plane |
| Worotnicki 1993[b] | Finite | Yes | Borehole wall | Transverse isotropic | Perpendicular to the bedding plane |
| Ben Ouanas 2010-2011 This study | Finite | Yes | In the inclusion (CSIRO) & Borehole wall | Transverse isotropic | Any |

(1) The formulations include the presence of one to three networks of joints with one or more drillings;

(2) Relations are given with the assumption of Saint-Venant for the anisotropic shear modulus;

(3) This is a generalization of Berry's solution (1968), which allows to take into account the presence of glue;

(4) When the hole is oriented perpendicular to the bedding plane and in the case of an isotropic stress state at infinity or biaxial test, the constitutive equations depend only on three constants: the two modulii and Young Poisson's ratio in the anisotropic plane. This requires further testing to identify the anisotropic shear modulus and Poisson's ratio in the isotropic plane;

(a) No assumption on the far field state of stresses;

(b) The state of stresses follows
 the biaxial compression test.

In the following, two alternative methods to interpret biaxial tests carried out in anisotropic rocks are proposed:

a) a so-called semi-numerical method, based on numerical modelling of the biaxial tests and error minimization of the five elastic constants of the rock;

b) a program of inversion implemented in Mathematica combining the analytical solutions (Nunes 2002 or Worotnicki 1993) and the general semi-analytical solutions proposed by Amadei (1983, 2000), to determine the five elastic constants of the transversely isotropic rock using an iterative process.

**IV.** FIRST ALTERNATIVE PROPOSED TO INTERPRET BIAXIAL TESTS: SEMI-NUMERICAL METHOD

Both methods are respectful of the core geometry (finite external radius), the presence of the glue layer as well as the distribution of stresses inside the anisotropic rock.

*A* Principle

In this first approach, the biaxial test is modelled using a finite element code. The geometry of the numerical model is that of a 40 cm-long hollow cylinder composed of two concentric annuli (Fig.4). The 42 mm thick outer annulus represents the rock core of 146 mm diameter. The rock is modelled as a transversely isotropic, linearly elastic material whose behaviour is defined by a set of five parameters: the normal ($E_1$) and parallel ($E_2$) Young's moduli, the out-of-plane ($\nu_{12}$) and in-plane ($\nu_{23}$) Poisson's ratios and the shear modulus $G_{12}$. The core axis is superimposed with the axis #3 of the anisotropy coordinate system, as shown in Fig. 5 and Fig. 5. The 1.5 mm thick inner annulus of the model represents the CSIRO cell outer shell and the epoxy glue layer, modelled as a single material. This inner annulus is modelled as an isotropic, linearly elastic material with a Young's modulus $E_c$=2.6 GPa and a Poisson's ratio $\nu_c$=0.4 corresponding to that of the epoxy.
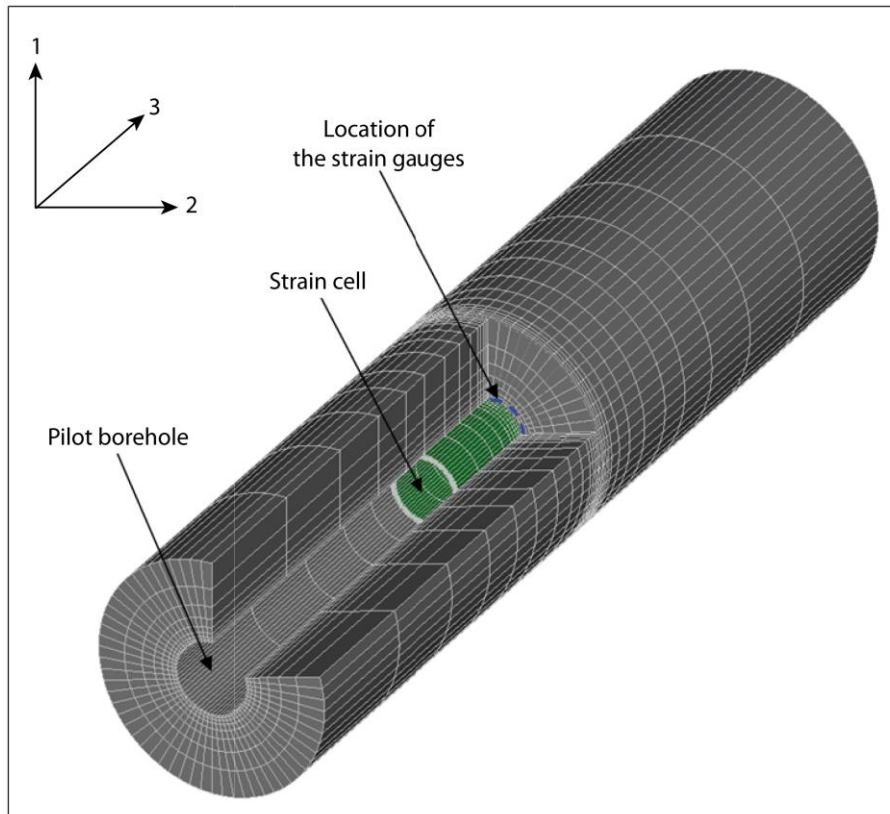


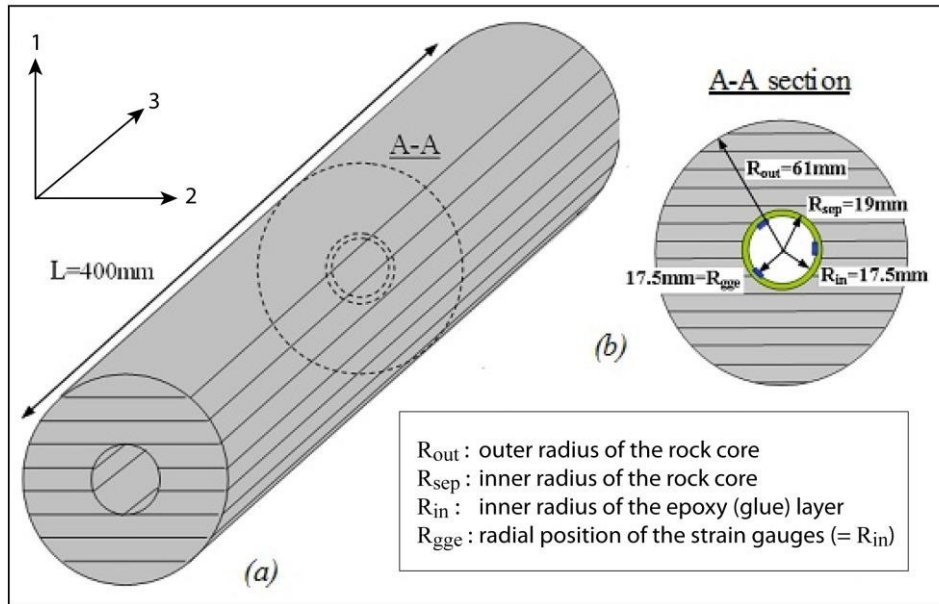Fig. 4. 3D numerical model of a biaxial test.

Fig. 5. (a) 3D view of the model: axis #1 is perpendicular to the plane of isotropy, and axis #3 is the hole axis in the plane of isotropy. (b) Cross section of model showing the two concentric annuli. The strain gauges are located on the outer surface of the cell (radius Rgge), which coincides with the inner surface of the epoxy layer (Rin).

A uniform external pressure P is applied on the outer surface of the model, the internal pressure being zero. The induced axial, orthoradial and oblique strains at the gauge locations (denoted $\varepsilon_i$, i=1...12) are calculated numerically and compared with those recorded during the actual test through the following discrepancy factor:

$$\delta = \max_{i=1...12} \left| \frac{\varepsilon_i^{model} - \varepsilon_i^{measure}}{\varepsilon_i^{measure}} \right|$$

## B    Iterative minimization of the discrepancy factor

The principle of the method (Ben Ouanas et al., 2010) is to determine the set of elastic parameters that minimises the discrepancy factor.

### 1)    First step: determination of an initial set of elastic parameters

The first step of the method consists of determining an initial set of transverse isotropic elastic parameters. For this purpose, we propose to deliberately apply to anisotropic material the formulas proposed by Worotniki (1993, p. 351) for the Young's modulus and Poisson's ratio of an isotropic rock cylinder with an inner soft layer.

The initial value of the Young's modulus in the plane of isotropy (E2) is derived by considering only the strain $\varepsilon_{\theta\theta}^{//}$ measured during the test by the orthoradial gauge whose direction is the closest to the plane of isotropy (Fig.6):

$$E_2 = 2K^{//} \frac{R_{ext}^2 \; P}{R_{ext}^2 - R_{sep}^2 \; \varepsilon_{\theta\theta}^{//}}$$

$$K^{\square} = \frac{\square n + 1 - 2\nu \square_c}{\left[ e^{\square} (1 - n)(M + 1 - 2\nu \square)_{\nu_2} (M - 1) \right] + n + 1 - 2\nu \square_c}$$

$$e^{\perp} = \frac{G_c}{G_{12}} = \frac{E_c\left[2 + (1 + \nu_{12})\right]}{E_1\left[2 + (1 + \nu_c)\right]}$$

The initial value of the Young's modulus in the direction perpendicular to plane of isotropy ($E_1$) is derived from the strain $\varepsilon_{\theta\theta}^{\perp}$ measured by the orthoradial gauge whose direction is the closest to the perpendicular to the plane of isotropy:

$$E_1 = 2K^{\perp} \frac{R_{out}^2}{R_{out}^2 - R_{sep}^2} \frac{P}{\varepsilon_{\theta\theta}^{\perp}}$$

$$K^{//} = \left[ \frac{\nu n + 1 - 2\nu_c}{e^{//}\,(1-n)(M+1-2\nu_{23})\Big/(M-1) + n + 1 - 2\nu_c} \right]$$

$$e^{//} = \frac{G_c}{G_{23}} = \frac{E_c\left[2 + (1 + \nu_{23})\right]}{E_2\left[2 + (1 + \nu_c)\right]}$$

The $K^{\perp}$ and $K^{//}$ correction factors are adapted from the expression for K given by Worotnicki (1993, p.352)

where $G_c$ is the epoxy shear modulus and

$$\nu = \frac{R_{sep}^2}{R_{gge}^2}$$

$$n = \frac{R_{in}^2}{R_{sep}^2}$$

$$M = \frac{R_{o,ut}^2}{R_{sep}^2}$$

$$G_{23} = \frac{E_2}{2\left(1 + 2\nu_{23}\right)}.$$

$R_{ext}$ and $R_{sep}$ represent the external and the internal radii of the rock core (Fig.6). $K^{\perp}$ and $K//$ are correction factors similar to the K factor proposed by Worotniki (1993), that account for the presence of the inclusion (see Appendix 1 for there values).

The initial estimates of the Poisson's ratios $\nu_{12}$ and $\nu_{23}$ are obtained as:

$$\nu_{12} = -K^{\perp} \frac{\varepsilon_{zz}}{\varepsilon_{\theta\theta}^{//}}$$

$$\nu_{23} = -K^{//} \frac{\varepsilon_{zz}}{\varepsilon_{\theta\theta}^{\perp}}.$$

where $\varepsilon_{zz}$ denotes the axial strain measured during the test.

An initial estimate of the shear modulus $G_{12}$ is then obtained according to Saint-Venant's hypothesis:
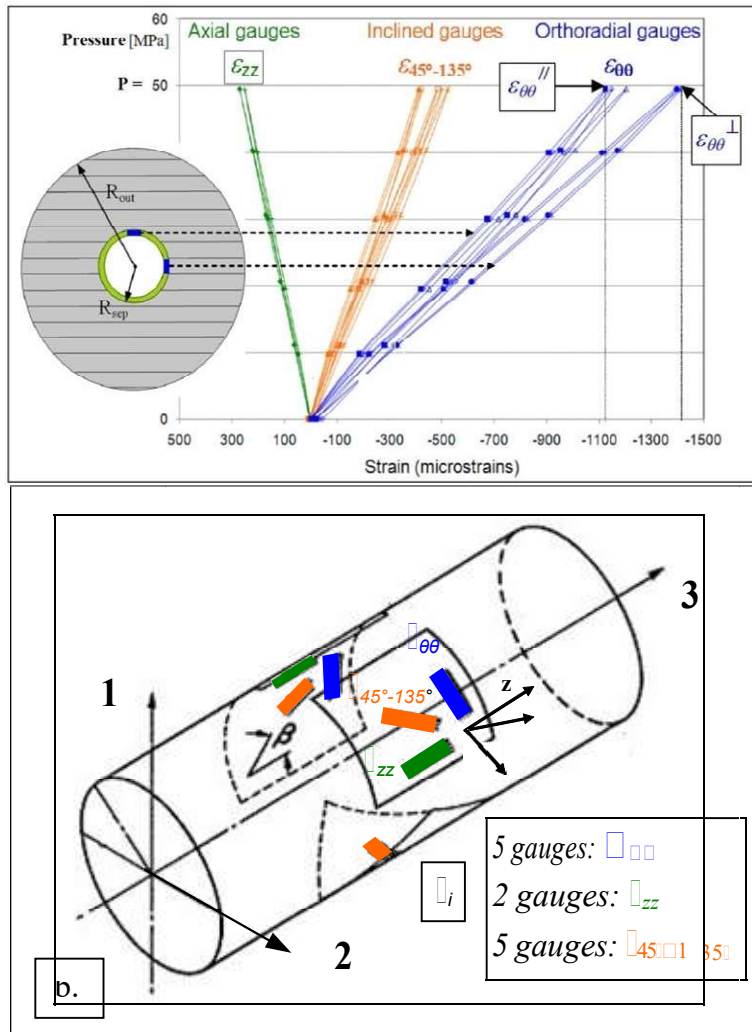
$$G_{12} = \frac{E_1 E_2}{E_1 + E_2(1 + 2\nu_{12})}$$

Fig. 6. a-b : Results of a biaxial test on Tournemire argillite displaying the values of $\varepsilon_{\theta\theta}^{//}$ and $\varepsilon_{\theta\theta}^{\perp}$. In practice, the corresponding strain gauge are generally not perfectly parallel and perpendicular to the plane of anisotropy of the rock. In such a case, the gauges closest to these positions are considered.

*2)* Second step: optimisation of elastic parameters using ad-hoc charts

A sensitivity analysis of the variations of the orthoradial strains $\varepsilon_{\theta\theta}^{//}$ and $\varepsilon_{\theta\theta}^{\perp}$ with the elastic parameters of the rock was carried by conducting a great number of numerical calculations whose results cannot be presented here in detail. It shows that $\varepsilon_{\theta\theta}^{//}$ and $\varepsilon_{\theta\theta}^{\perp}$ primarily depend on the rock's Young moduli $E_1$ and $E_2$. This property may be due to the particular geometry of the studied system, the borehole axis being parallel to the plane of isotropy. It enables us to start the optimisation process in this case by adjusting the Young's moduli, the other elastic parameters being kept constant. To do so, a chart is constructed by conducting numerous numerical calculations with different Young's moduli. An example of application is presented in §3.

In the next step, the Young's moduli are set to their adjusted optimal values and the rock's Poisson ratios are adjusted graphically using another chart, in order to lower the discrepancy factor even more. This is possible by considering the axial strain, which appears to be mainly governed by the Poisson's ratios of the rock.

Finally, having set the Young's moduli and Poisson's ratios to their optimised values, we again calculate the shear modulus of the rock $G_{12}$ using Saint-Venant's hypothesis (Eq. 6). The discrepancy factor may then be further decreased by adjusting the shear modulus of the rock, considering that Saint-Venant's hypothesis does not always apply perfectly. The objective of this last step is to obtain a discrepancy factor of less than 5-6%.

**V.** SECOND ALTERNATIVE PROPOSED TO INTERPRET BIAXIAL TESTS: SEMI-ANALYTICAL AND ITERATIVE APPROACH

*A* Stress distribution at the gauges position.

One of the major difficulties of biaxial test data inversion is the reliable estimation of the stress distribution at the cell gauges position in the presence of glue or on the inner wall of the core, since in the most general case (anisotropic , borehole oriented out of the axes of anisotropy, anisotropic initial stress state) there are no analytical solutions between stresses and strains (see Table 1), and therefore to carry out a data inversion when the deformations are assumed to be known (measured or approximated).

There is no analytical solution giving the stress distribution at the level of the gauges. So we propose an iterative method which combines analytical (Nunes, 2002) and semi-analytical solutions (prog CSIRA by Amadei, 1983, 2000).

*1)* Case of axes of the borehole is oriented parallel to the bedding plane.

In this case, two modules of inversion were written using the Mathematica code. These modules are based on the equations proposed by Worotnicki (1993) to express the strains ($\epsilon_\theta$, $\epsilon_z$, $\epsilon_{\theta z}$) in the plane of rosettes as a function of the five elastic constants of the rock, the two elastic constants of the inclusion and the four correction factors for the effect of the glue. The first module assumes that the outer radius of the core is infinite with a hydrostatic state of stress and that for the five elastic constants of the rock are independent. The second module admits a finite outer radius of the core, but that assumes the Saint Venant's relationship for the shear modulus $G_{12}$. These equations were adapted to satisfy the relationship of Duncan and Pender (1980) in the isotropic case.

*2)* General Case

In general, the deformation measured by a strain gauge inclined with an angle $\theta$ with respect to the borehole axis is given by:

$$\epsilon_\theta = \epsilon(\theta,\phi) = \epsilon_\theta \, sin^2\theta + \epsilon_z \, cos^2\theta + \epsilon_{\theta z} \, sin\theta \, cos\theta$$

This relation allows, on one hand, to express the theoretical strains at the level of a given gauge. In addition, the 9 or 12 measures of strains ($\epsilon_k$ k = 1, $N_{mes}$ where $N_{mes}$ equal to 9 for 3 rosettes or 12 if 4 rosettes are used) are

known from the biaxial test. Minimizing the difference $\sum_{k=1}^{Nmes} \left| \epsilon_k - \epsilon(\theta_k,\phi_k) \right|^2$ between the measurements and

"theoretical" strains represented by equation (14) leads to calculate the five elastic constants. The other way is to perform a non-linear regression between the measures $\{\theta_i, \phi_i, \epsilon_i\}_{i=1,Nmes}$ and the theoretical model $\{\theta_i, \phi_i, \epsilon(\theta_i, \phi_i)\}_{i=1,Nmes}$ dependent on the elastic constants $E_1$, $E_2$, $\nu_{12}$ $\nu_{23}$ and $G_{12}$. In this case, the user has access to the associated statistics of the multiple nonlinear regression.

In the more general case where the core is drilled in the direction of the anisotropy axis and the anisotropy orientation is known, we leaned on the work of Amadei (1983) based on a generalized plane strain formulation of stresses and strains around an overcoring test or drilling (uniformly supported or not) and the use of Fourier series of equations Lekhnitski (1963).

First Case : the theoretical formulation of strains that would be measured in the CSIRO cells during coring is given by Amadei (1983, 2000) and recalled in a simplified equation (18) forms. These strains are expressed in terms of Fourier coefficients, the characteristics of the glue, anisotropic characteristics of the core (assuming the outer radius as infinity) and the state of stress at the infinite ($\sigma_0$)$_{xyz}$ which is unknown in the author's formulation :

$$\epsilon_{l_i} = (0, \, sin^2\theta_i, \, cos^2\theta_i, \, sin\theta_i \, cos\theta_i, \, 0, \, 0)[T_5](\sigma_0)^t_{xyz}$$ The matrix $[T_5]$ is calculated at ($r_i/a$, $\theta_i$) where $r_i$ is the

radial position of gauge n°i, $\theta_i$ its angular position, and its components depend on: (a) the matrix transform between the orientations of anisotropy and hole with respect to the global one, (b) the elastic properties (transversely

isotropic or orthotropic) $E_i$, $\nu_{ij}$ and $G_{ij}$, (i, j=1,3) assumed to be known, (c) the elastic properties of the inclusion $E_c$, $\nu_c$ and its geometry, (d) the Fourrier coefficients computed from $E_c$, $\nu_c$, $E_i$, $\nu_{ij}$ and $G_{ij}$ and the complexes parameters of Lekhnitski.

The linear regression between the theoretical and measured strains $\left( \tilde{\varepsilon} = \left\{ \tilde{\varepsilon}_i \right\}_{i=1,Nmes} \right)$ allows to compute the state of in situ stress ($\sigma$ 0) xyz. This is what is done in software: CSIRA (Amadei 1983, 2000) written in F77; modified CSIRA (Hakala et Sjöberg 2006) in F95 and *SYTGEOstress* (developed by INERIS and GeosRessources under Mathematica environment). The theoretical expressions of strains and stresses, and the corresponding algorithm are detailed in CSIRA Amadei (2000) and Hakala and Sjöberg (2006).

Second case : in fact, relation (18) has been established at any point (r/a, $\theta$) the inclusion by Amadei (1983).

If $\overset{\circ}{T}_5$ represents the evaluation of $[T_5]$ at the interface between hole and inclusion (that is to say $r_i/a=1$, $\theta_i$) the projection of the measured strains at the core wall (these are strains that should have been measured if we had directly stuck gauges at the interface) was proposed by Amadei (1986) and takes the following form:

$$\varepsilon_{l_i}^* = \varepsilon_{l_i} + (0,\ \sin^2\theta_i\ ,\ \cos^2\theta_i\ ,\ \sin\theta_i\ \cos\theta_i\ ,\ 0,\ 0)\ [T^*]_5\ [T]_5\ (\sigma_0)_{xyz}^t$$

Assuming the continuity of strains at the interface, the relation (19) also gives the deformations in the rock (in wall) that may be related to anisotropic elasticity tensor of the core. It would suffice to have an estimation of the stress distribution in wall for the problem of minimization.

Finally, the distribution of stresses and strains around a supported drilling (subject to a uniform pressure to the wall) or not, was also proposed by Amadei 1983 (through the Fourier series). The general expressions were synthesized by relationships B-34 to B-43 in appendix B of Amadei & Stephansson (1997) or equations A-15 to A-22 in appendix A of Amadei (2000).

## B    Step-by-step methodology

At first sight, all of these three points can, in principle, to make the inversion of biaxial test strains. The difficulty lies in the fact that it is necessary to know the elastic constants, which among other things are used to compute the Fourier coefficients, while in a biaxial test, the elastic constants represent the problem unknowns. Specific methodology of inversion has been proposed.

Step 1. With the aim to obtain a first estimation of the elastic constants, we make the following assumptions (a) the measured strains in the CSIRO cells are representative of those in the wall (as if CSIR cells are used), that is to say $\varepsilon_{l_i}^* = \tilde{\varepsilon}_{l_i}$ , (b) it is assumed that the stress distribution at the core wall of the core is uniform, and (c) we finally assume that the shear modulus G12 follows the empirical relationship of Saint-Venant. These assumptions lead us to the conditions of Nunes (1997, 2002) and the resulting solution (E1, E2, v1 and v2) is then used as input data (first approximation of elastic properties) of the iterative process.

Step 2. An iterative process at each stage, the relation (19) allows to calculate the "true" wall strains, assuming uniform stresses and theoretical deformation (uniform stresses and anisotropic material). The inversion identifies the new elastic properties improving those previously obtained in step 1, since the wall strains are corrected by taking into account the inclusion and the anisotropic shear modulus is not forced to follow the principle of Saint-Venant. Finally, this solution is used for the final step.

Step 3. One of the two preceding solutions (step 1 or 2) is used as input in the last iterative process in which each stage (k), the solution obtained at (k-1) is used to calculate the complex parameters of Lekhnitski (1963) and the Fourier coefficients required to evaluate the strains which should have been measured if the strain gauges were glued at the inclusion/core interface. Thus, Hooke's law provides the theoretical strains at the wall core as a function the five elastic constants. Minimizing the gap between the theoretical strains and "measured" one allows, after convergence (unfortunately not in all cases due to a strong nonlinearity of the functional to minimize), to obtain the five independent elastic constants.

Finaly, theses three steps are implemented under Mathematica environment. As an verification of the algorithm, synthetical data strains are computed from an given elastic properties (E1=9270 MPa; E2=24190 MPa; □12=0,2; □23=0,15; G12=3940 MPa), and used to evaluate the from the proposed procedure. The input strains (□def) are : {138.879, -708.937, -285.029, -526.141, -526.141, -1221.06, 138.879, -708.937, -285.029, -285.029, -1096.63, -495.918}. Application of the proposed methodology yielded to the following results : E1=9269.75 MPa; E2=24188.8 MPa; □12=0.20001; □23=0.1499; G12=3940.25 MPa, indicating a very good estimation of the modules.

## VI. CASE-STUDY

### A  Application of the charts method

The proposed method was applied to data obtained from two biaxial tests (TC35 and TC36) performed on argillite cores recovered during an overcoring test campaign conducted in the Tournemire experimental site, France (Rejeb & Tijani, 2003, Lahaie et al., 2010). Table 2, first line, presents the initial set of parameters determined using the procedure described in § B.1. The corresponding value of □ at this stage is approximately 25%.

The chart used to adjust $E_1$ and $E_2$ is presented in Fig.7 with the Poisson's ratios and the shear modulus equal to their initial values. The optimized Young's moduli of the rock can be graphically determined from the values of $\square^{//}_{\square\square}$ and $\square^{\square}_{\square\square}$ obtained during the actual biaxial test.
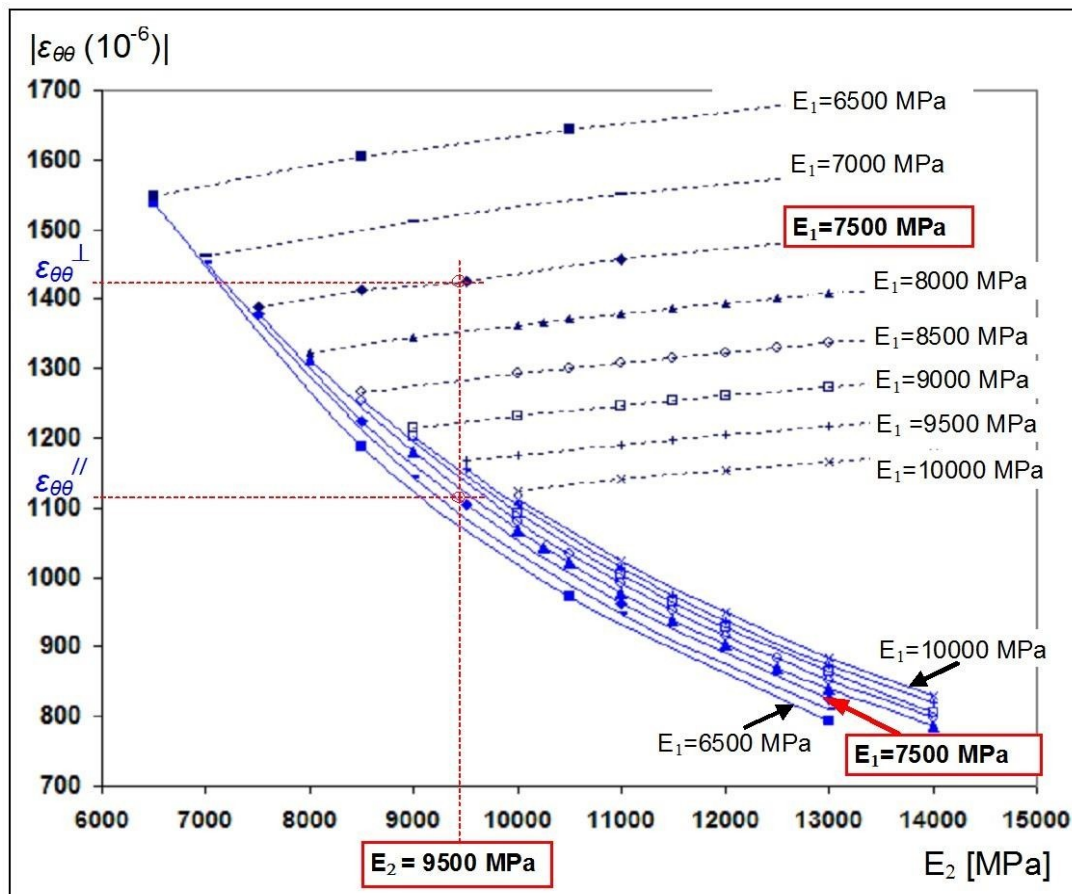


Fig. 7. Chart used for determination of the optimal Young's moduli. External pressure P=5 MPa. The calculated values of $\square^{//}_{\square\square}$ (continuous curves) and $\square^{\square}_{\square\square}$ (dotted curves) are presented for different combinations of E2 (horizontal axis) and E1 (values shown on the curves). The measured values are represented by the dotted straight lines.

The chart used to adjust $\square_{12}$ et $\square_{23}$ is presented in Fig. 8. In the particular case presented here, with the core axis being parallel to the plane of isotropy, there is not a unique pair of Poisson's ratios ($\square_{12}$, $\square_{23}$) that leads to the measured value of the axial strain. As no "best pair" can be determined, we propose to choose, from among all the possible pairs of Poisson's ratios, the pair that is the closest to the initial values.

Table 2: Elastic parameters of the Tournemire argillite obtained by different methods

| Mechanical Tests | Method/ref. | $E_1$ MPa | $E_2$ MPa | $v_{12}$ - | $v_{23}$ - | $G_{12}$ MPa | $A_E$ - |
|---|---|---|---|---|---|---|---|
| Biaxial #TC35 | Initial set (§B.1) | 8600 | 10,900 | 0.25 | 0.20 | 3757 | 1.3 |
| | Numerical (§B.2) | 7500 | 9500 | 0.22 | 0.17 | 4050 | 1.3 |
| | Analytical (§B) | 7954 | 10,199 | 0.29 | 0.18 | 3327 | 1 . 3 |
| Biaxial #TC36 | Initial set (§B.1) | 9400 | 12,800 | 0.26 | 0.19 | 4170 | 1.4 |
| | Numerical (§B.2) | 8000 | 11,000 | 0.23 | 0.18 | 4300 | 1.4 |
| | Analytical (§B) | 8893 | 12,769 | 0.29 | 0.1 8 | 3917 | 1 . 4 |
| Laboratory | Ben Ouanas (2011) | 9260 | 19,505 | 0.22 | 0.20 | 3942 | 1.9 |
| | Rejeb (1999) | 9270 | 24,190 | 0.20 | 0 . 1 5 | 3940 | 2.6 |

.
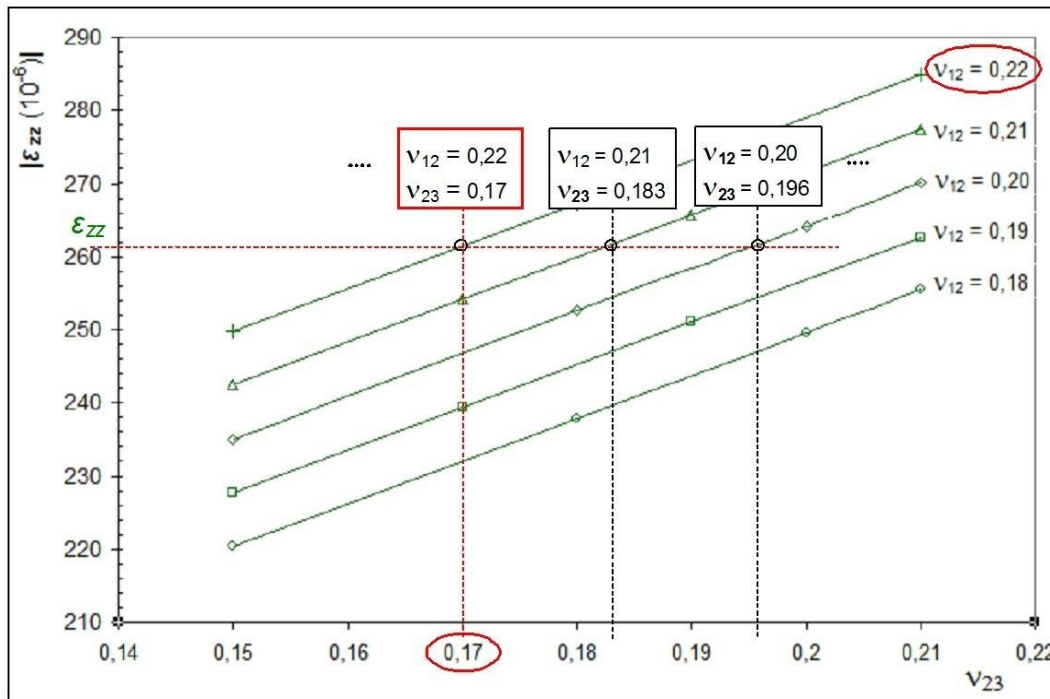


Fig. 8. Chart used for the determination of the optimal Poisson ratios.

At last, the shear modulus $G_{12}$ is determined using Saint-Venant's hypothesis and slightly adjusted in order to obtain a final value of $\square = 6\%$.

The set of elastic parameters obtained after the completion of the optimisation procedure is provided in Table 1, along with the value of the anisotropy ratio AE of the Young's moduli, defined as:

$$A_E = \frac{E_2}{E_1}$$

We note that the Young's modulus $E_2$ and the anisotropy ratio $A_E$ determined from the biaxial tests using this method have much lower values than those derived from the laboratory uniaxial and triaxial tests (see Table 1, last lines).

*B*    Comparison with the results obtained with an analytical method.

In order to check the validity of our results, we compared those with the ones obtained with another method. Souley (unpublished) developed an analytical method for the determination of the elastic parameters of transversely isotropic rock from biaxial tests.

Table 1 provides the set of elastic parameters obtained from the Tournemire TC35 and TC36 biaxial tests using proposed iterative process (§ 4.2). They are found to be similar to those obtained from the charts method. In particular, they confirm the low anisotropy ratio.

## VII.    DISCUSSION

*A*    Applicability of the chart method

The method presented in this paper provides an alternative approach for determining the elastic parameters of a transversely isotropic rock from a biaxial test. This method is based on the direct modelling of a great number of biaxial tests with different sets of parameters and the research of the set of parameters that minimizes a discrepancy factor between observed and modelled strains. The method may be compared to a Monte Carlo approach except that the exploration of the parameter space is not systematic but oriented by the choice of an initial set of parameters determined from analytical solutions (see § 2.2.1). This renders the method acceptable in terms of computation time. Another advantage of the method is that it is relatively general in that it needs very few assumptions with regard to the core geometry, direction of anisotropy, finiteness of the core radius, absence of glue layer, etc. Moreover, the graphical presentation of the calculation results in the form of charts makes it easy to assess the sensitivity of the computed strains on the elastic parameters, thus helping to take into account uncertainties affecting the strain measurements during *in situ* biaxial tests.

However the method remains relatively time-consuming. As an illustration, the construction of a chart like the one in Figs 7 and 8 requires between 50 and 100 numerical calculations. As a specific chart is needed for each biaxial test, this makes the biaxial test interpretation, and therefore stress determination, practically impossible to do immediately in the field.

*B*    Possible explanations for the low anisotropy ratio found during the case-study

The Young's moduli of the Tournemire argillite determined using various methods are shown in Table 1. In spite of small variations in the results depending on the interpretation method, all biaxial tests lead to a low value of the Young's modulus $E_2$ and of the anisotropy ratio $A_E$ with respect to the values derived from the laboratory uniaxial and triaxial tests. This difference is confirmed by the fact that, when the laboratory parameters are used in our numerical modelling, ☐ values of up to 40% are obtained. Thus, the elastic parameters determined in the laboratory tests do not satisfactorily reproduce the behaviour of the argillite rock during those biaxial tests.

Similar discrepancies between the biaxial tests and the laboratory uniaxial or triaxial tests were observed for other types of rocks, such as granite (Ask, 2005), gneiss (Clément et al., 2009), limestone, schist and sandstone (unpublished data from INERIS). For this reason, we expect this difference to originate from the biaxial test itself and not from the properties of the tested rock. Possible explanations were suspected to be linked to the presence of the epoxy cement layer. Garitty et al. (1985) and Irvin et al. (1987) already pointed out that the behaviour of the epoxy may differ from linear elasticity and observed a phenomenon of plastic yielding of the epoxy cement when it is incompletely polymerised. This phenomenon may occur, for example, when the rock temperature is too low to achieve a complete polymerisation of the cement (Irvin et al., 1987).

We noted that the Young's moduli of the overcored samples determined from biaxial test using the chart method evolve with the hardening time of the epoxy adhesive (Fig. ). This result may be interpreted as a signature of the evolution of the epoxy's mechanical properties as it hardens. This change appears to hold up to very high curing times (> 40-70 h) and indicates that the hardening time needed for the adhesive to achieve its definite mechanical properties may, in low-rock temperature conditions, be significantly longer than the time suggested by the glue manufacturer (16 h), as mentioned by Lahaie et al. (2010). In such conditions, strain cells that require less glue (e.g. the Borre probe, see Sjöberg et al., 2003) or no glue (e.g. the modified doorstopper cell, see Corthésy et al., 2003) are probably preferable.

Nonetheless we note that even for long curing times (TC 34 or TC36 tests), the value of the Young's modulus $E_2$ does not exceed 13 GPa. Consequently, the insufficient hardening of the glue does not provide a fully satisfying explanation of the discrepancy between the anisotropy ratios provided by biaxial and laboratory tests. Futher investigations are in progress to try to solve this issue.
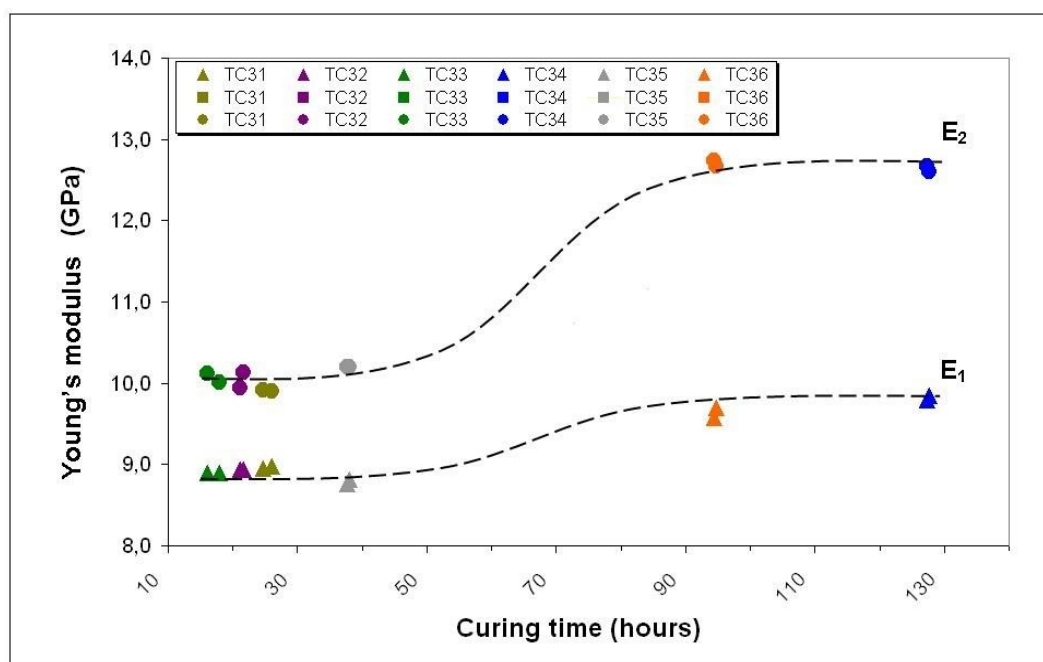


Fig. 9. Effect of the curing time of the epoxy glue on the Young's moduli determined from the biaxial test using the charts method

## VIII. CONCLUSION

The determination of the elastic parameters of transversely isotropic rocks is typically performed in the laboratory, using uniaxial or triaxial tests on small cylindrical samples prepared with different directions relative to the plane of transverse isotropy. We propose an alternative method based on *in situ* biaxial tests undertaken on rock cylinders instrumented with a triaxial CSIRO Hi cell, and on their numerical modelling. It consists in constructing charts that are used for the graphical step-by-step inversion of the strain readings obtained during the test.

One advantage of this method, in comparison with analytical or semi-analytical solutions available in literature, is that it does not require any specific assumption, excepted the elastic behaviour of the rock, which can easily be verified during the biaxial test. One drawback is that it requires the construction of charts corresponding to an initial set of anticipated elastic parameters, which is time consuming.

This method has been successfully tested for interpretation of biaxial tests performed on argillite rock samples from the Tournemire experimental station, France. The anisotropy ratio of this rock was found to be particularly weak compared to the ratio determined for this rock using laboratory tests. We show that a possible origin of this

difference is related to the incomplete polymerisation of the epoxy cement layer used in the biaxial test, resulting from an insufficient curing time or from low temperatures. This problem alters the strain measured by the strain gauges.

# References

[1] Ask D. [2006 b], Measurement-related uncertainties in overcoring data at the Äspö HRL, Sweden. Part 2: Biaxial tests of CSIRO HI overcore samples. International Journal of Rock Mechanics & Mining Sciences, Issue 1, vol. 43, pages 127–138.

[2] Amadei B. (1986). Analysis of data obtained with the CSIRO cell in anisotropic rock masses, Commnwealth Scinetific and Industrial Research Organization – Institute of Energy and Earth Ressources, Technical Report N° 141, 75p.

[3] Amadei, B. & Stephansson, O. (1997). Rock stress and its measurement. London: Chapman & Hall, 490 pp.

[4] Amadei, B. (2000). CSIRA: A computer program to determine in situ stresses by overcoring in anisotropic rock with CSIR-type triaxial strain cells. Version 3.0. Boulder: University of Colorado

[5] Ben Ouanas A. Les mesures de déformation en forage en terrain anisotrope. Utilisation de cellules CSIRO dans l'argilite de Tournemire (Aveyron, sud de la France) pour l'étude de la stabilité des stockages géologiques des déchets radioactifs. Éditions universitaires européennes, ISBN : 978-613-1-57558-7. PhD Thesis. Ecole des Mines de Nancy: Nancy–University; 2011.

[6] Ben Ouanas A, Gunzburger Y, Lahaie F, Piguet JP, Barnichon JD. Mechanical testing of hollow cores to determine elastic parameters of anisotropic rocks using the CSIRO HI cell. ISBN : 978-0-415-58654-2. Lausanne, Suisse, European Rock Mechanics Symposium: Eurock 2010; 103–106.

[7] Ben Ouanas A., Gunzburger Y., Lahaie F., Piguet J-P. et Barnichon J-D. [2010 b], Mechanical testing of hollow cores to determine elastic parameters of anisotropic rocks using the CSIRO HI cell – Application to the Tournemire argilite. Hammamet 2010, Tunisie, The Fifth International Conference on Advances in Mechanical Engineering and Mechanics (ICAMEM2010).

[8] Berry DS, Fairhurst C. (1966). Influence of rock anisotropy and time dependent deformation on the stress-relief and high-modulus inclusion techniques of in situ stress determination. Testing techniques for rock mechanics, ASTM, STP.402, Am. Soc.Testing Mats, p. 190‑206.

[9] Berry DS. (1968). The theory of stress determination by means of stress relief techniques in a transversely isotropic medium. Technical Report No. 5-68, Missouri River Division Corps of Engineers, Omaha, Nebraska, 1968, 36p.

[10] Clément C. [2008], Auscultation d'un versant rocheux soumis aux sollicitations thermiques naturelles. Cas des Rochers de Valabres (Alpes-Maritimes). Thèse de doctorat à Nancy-Université, Institut National Polytechnique de Lorraine, 220 pages.

[11] Corthésy R, Leite M.H, Gill D.E, Gaudin B, Stress Measurement in Soft Rocks. Engineering Geology 69 (2003)

[12] Duncan Fama M.E. & Pender M.J. [1980], Analysis of the Hollow Inclusion Technique for measuring in situ Rock stress. International Journal of Rock Machanics, Mining Sciences & Geomechanics Abstract, vol 17, pages 137-146.

[13] Gonano LP, Sharp JC. (1983). Critical evaluation of rock behaviour for in situ stress determination using overcoring methods. Proceedings of the Fifth International Congress ISRM, vol. 1. Melbourne, 1983. p. A241‑A251.

[14] Garitty P., Irvin R.A. et Farmer I. W. [1983], Problems associated with near surface in-situ sress measurements by the overcoring method. 26th US symposium on rock mechanics, Rapid city SD, 26-28 june 1985.

[15] Hakala M. & J. Sjöberg (2006). A methodology of interpretation of overcoring stress measurements in anisotropic rock, Working Report 2006-99, 207p.

[16] Irvin R.A., Garitty P. et Farmer I. W. [1987], The effect of boundary yiel on the result of in-situ stress measurements using overcoring techniques. Int. J of Rock Mech. Min. Sci. & Geomech. Abstr. 24, 89-93.

[17] Lahaie F, Gunzburger Y, Ben Ouanas A, Barnichon JD, Bigarré P, Piguet JP[2010]. Impact of epoxy glue curing time on the quality of overcoring stress measurements in low-temperature environments. 5th International Symposium on In-situ Rock Stress, ISBN

[18] Lekhnitskii SG. (1963). Theory of elasticity of an anisotropic elastic body. In: Brandstatter JJ, editor. Holden-day series in mathematical physics. San Francisco: Holden Day Inc., 404p.

[19] Nunes A.L.L.S. (2002). A new method for determination of transverse isotropic orientation and the associated elastic parameters for intact rock. Int. J of Rock Mech. & Min Sci, Vol. 39, 257–273

[20] Nunes A.L.LS. (1997). Nouvelle méthode de détermination de la déformabilité des roches transversalement isotropes avec la cellule triaxiale CSIR. Ph. D. thesis, Ecole Polytechnique de Montreal, University of Montreal, Canada, 490p

[21] Rejeb A., Millard A., Maleki K. (2007). Mine-By-Test experiment around the excavated 2003 gallery in the Tournemire site. NFPRO project – RTDC – WP 4.2 – Delivreable 4.2.5, report DEI/SARG/2007-40 (IRSN)

[22] Rejeb A. [1999], Mechanical characterisation of the argellious Tournemire site (France). Proceedings of ROCKSITE-99, Bangalore, India December 6-8, 1999. New Delhi, Cacutta : Oxford & IBH Publishing CO.PVT.LTD.

[23] Rejeb A. & Tijani M. [2003], Champ de contrainte dans les argilites de Tournemire – Mesures in situ et interprétation. Revue française de géotechnique N°103, pages 75-84.

[24] Sjöberg J., Christiansson R. et Hudson J.A. [2003], ISRM Suggested Methods for rock stress estimation—Part 2 : overcoring methods. International Journal of Rock Mechanics & Mining Sciences, special issue 7-8, vol. 40, pages 999–1010.

[25] Sjöberg J. & Klasson H. [2003], Stress measurements in deep boreholes using the Borre (SSPB) probe. Special Issue of the International Journal of Rock Mechanics and Mining Sciences, issue 7-8, volume 40, pages 1205–1223.

[26] SYTGEOstress☐ Version 1.0 – Logiciel d'inversion pour la caractérisation des champs de contraintes, INERIS

[27] Van Heerden WL. (1983). Stress‐strain relations applicable to overcoring techniques in transversely isotropic rocks. Int J Rock Mech Min Sci Geomech Abstr 20(6):277‐82.

[28] Worotnicki G. (1993) CSIRO triaxial stress measurement cell. In: Hudson JA, editor. Comprehensive rock engineering—principles, practice & projects, vol. 3. p. 329‐94.

# The Performance of Electro-Fenton (EF) Process in the Removal of the organic polluting load of the olivemill wastewater

YAHIA Zineb*[1], ZIATI Mounir[2]

[1*] *Faculty of chemistry university of science and technology USTHB, BP32, El Alia, Bab Ezzouar, Algeria.*

*Zineb.yahia@usthb.edu.dz*
*Zinebyahia66@gmail.com*

[2] *Laboratory of soft technologies, Physico-Chemical Valorization of Biological Materials and Biodiversity, Chemistry Department, Faculty of sciences, M'hamed bougara University, Boumerdes 35000, Algeria.*

*Abstract*— **The treatment of olive mill wastewater is one of the most important environmental problems for Mediterranean countries. This effluent contains many organic compounds like polyphenols. This study focuses on performance evaluation of the electro-Fenton process, using graphite electrodes and hydrogen peroxide ($H_2O_2$) for removal of polyphenols and chemical oxygen demand from olive mill wastewater. The experiments are carried out at different values of the potential and for different pH of the medium. The results obtained under the optimal conditions show that 81% of the chemical oxygen demand and 77% of the polyphenols were eliminated when the pH = 3 and the imposed potential is 2 Volt.**

*Keywords*— **olive mill wastewater, electro-Fenton, polyphenols, chemical oxygen demand, graphite.**
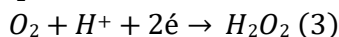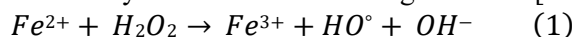
## I. INTRODUCTION

The Mediterranean countries are confronted with the problem of the elimination of olive mill wastewater (OMW) from olive oil production. The latter is generally released into the natural environment without any prior treatment, thus causing a negative environmental [1]. Indeed, this effluent has a high saline load with conductivity of about 10 mS/cm, due mainly to potassium, chloride, calcium and magnesium ions and it is very acidic (pH = 4.5 - 5.5), rich in organic matter and polyphenols with low biodegradability [2, 3]. OMW were constituted of water (83–92%), organic compounds (4–16%), and inorganic chemicals (1–2%) [4]. These effluents contain the suspended solids that may reach up to 190 g/L [5] and quite phytotoxic [6, 7].

There are several techniques for the treatment of this effluent. Advanced oxidation processes (AOP) is very effective alternative, which consists of oxidizing organic matter. Such as photocatalysis [8], ozonation [9], chlorine dioxide [10], Fenton-based process [11, 12] and other strong oxidants [13].

Electro Fenton is one of the advanced oxidation processes used in olive mill wastewater treatment technology. In this case, this method is considered as a viable alternative [14, 15]. Usually the electro-Fenton processes can classify into two categories, electro Fenton (EF) process involving $H_2O_2$ generation and EF process involving ferrous regeneration, which the efficiency of both processes can be comparable with the conventional chemical dosing methods [11; 16, 17]. Therefore, Electro Fenton is powerful for degrading most organic compounds including toxic and non-biodegradable ones. Due to the increasing species and amount of toxic and bio refractory organic pollutants in wastewater, great attention has been paid on advanced oxidation processes [18].

The reaction machanism can be described by means of the following reactions [19, 20].

$$Fe^{2+} + H_2O_2 \rightarrow Fe^{3+} + HO° + OH^- \quad (1)$$
$$Fe^{2+} + H_2O_2 + H^+ \rightarrow HO° + OH^- + H_2O \quad (2)$$
$$O_2 + H^+ + 2é \rightarrow H_2O_2 \quad (3)$$

Ferrous ions are consumed more rapidly than they are produced.

$$Fe^{2+} + HO° \rightarrow Fe^{3+} + HO^- \quad (4)$$
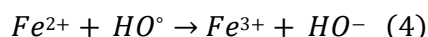
The objective of the present work is to investigate the electro-Fenton process for the removal of COD and polyphenols of olive mill wastewater by the study of the effect of several parameters, such as applied potential difference value and pH of the medium. An experimental approach was followed and completed with an analysis and global discussion of the results obtained.

# 1. MATERIALS AND METHODS
## 1.1. ORIGIN OF THE OLIVE MILL WASTEWATER

The used olive mill wastewater is taken from olive oil industry in Algeria during the olive growing season and it has been maintained in the dark at 4 °C to avoid further degradation. The unique pretreatment of OMW has consisted of filtration under buchner for avoiding excessive quantity of solids.

## PHYSICOCHEMICAL CHARACTERIZATION OF OLIVE MILL WASTEWATER

The physicochemical analysis of olive mill wastewater is devoted to the determination of some physicochemical parameters. The pH was measured using an Inolab WTW brand pH meter, the conductivity is measured by a HACH HQ40d brand conductivity meter, the turbidity is measured from a HANNA instrument optical turbidmeter, the analysis of chlorides is carried out by Mohr method [21], the determination of the concentration of total polyphenols is carried out with the official procedure by spectrophotometer (at 765 nm) [22] in which the Folin-Ciocalteu reagent was used as a selective reagent for the total polyphenols. The chemical and biological oxygen demand "COD and $BOD_5$" is achieved according to method 5220 and to the norm AFNOR NF EN 1899-2 respectively, the total organic carbon "TOC" is measured according to the norm 8245. The assay trace elements (Fe and Ni) are performed using Inductively Coupled Plasma Atomic Emission Spectrometry (ICP-AES). The suspended solids are determined by centrifugation.

## ELECTRO FENTON TREATMENT METHODOLOGY

Various electrochemical mechanisms were applied to generate $H_2O_2$ or $Fe^{+2}$ or reduce $Fe^{+3}$ to $Fe^{+2}$ in the Electro-Fenton process [23-25]. In this study, l'electro Fenton was conducted in a cylindrical reactor (Figure 1) containing 1L of the effluent, a magnetic stirrer, to homogenize the solution, and the graphite-based electrodes which are connected with potentiostat (Constanter/Netzgerat Universel PHYWE) and ammeter (PHYWE) to measure the current during the oxidation of the organic matter of the olive mill wastewater.

After the addition of the required amount of $H_2O_2$ (30g/L), the electro-fenton experiment was started (it should be noted that this concentration was chosen on the basis of a study already carried out on the effect of the $H_2O_2$ dose on the reduction of OMW pollution). During the experiments, a volume of filtrate sample was drawn after 30, 60, 90, 120, 150 and 180 minutes in order to find the optimum treatment time for the COD and polyphenols removal.

At the end of each manipulation, the graphite electrodes were cleaned with dilute hydrochloric acid (0.1 M), then rinsed with distilled water and dried at 105°C for about two hours. The reduction rate of the parameters pollution (chemical oxygen demand and polyphenols), expressed in percentage TX (%), was calculated using the following formula:

$$TX(\%) = \frac{(C_iX - C_fX)}{C_iX} \times 100 \quad (5)$$

Where: $c_ix$ and $c_fx$ are the concentrations of the element before and after electro-fenton treatment (mg/L).

In order to optimize and better understand the treatment process, the different operating parameters, such as the applied potential difference value (1, 5; 2 and 2.5) and pH of the solution (3, 4.9 and 7), have been investigated.
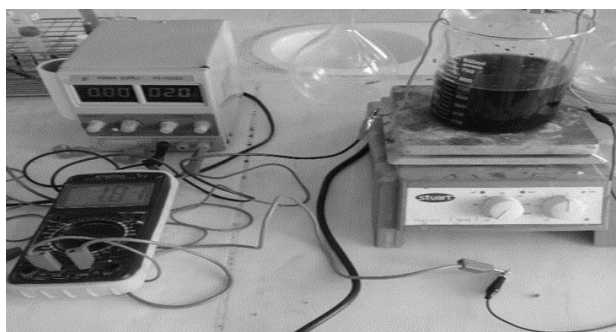
Fig1. The experimental arrangement used in the electro Fenton.

## 1. RESULTS AND DISCUSSIONS
### 1.1. PHYSICOCHEMICAL CHARACTERIZATION OF OLIVE MILL WASTEWATER

Olive mill effluents can be easily identified by their dark-brown colour and specifically their unpleasant odour. The analyses performed on this effluent (Table 1) demonstrate that it is principally characterized by a slightly acidic (pH around 4.9). The COD, BOD$_5$, TOC and polyphenols values far exceed the authorized standard limits [26]. These parameters confirm the OMW toxicity. The biodegradation of these matters causes oxygen consumption where a possible eutrophication of the receiving environment with a deterioration of the fauna and flora and the creation of harmful resistant species can take place; therefore, this effluent should be treated and removed.

TABLE I
Main physicochemical characteristics of raw OMW

| Parameter | Value | Official Journal of the Algerian Republic 2006 |
|---|---|---|
| pH | 4.9 | 6.5-8.5 |
| Conductivity (mS/cm) | 7.60 | / |
| Turbidity (NTU) | 3927 | / |
| COD (mg/L) | 14110 | 120 |
| BOD$_5$ (mg/L) | 18400 | 35 |
| TOC (mg'O$_2$/L) | 12460 | / |
| Chloride (mg/L) | 2217 | 250 |
| Oxidizable matter (mg/L) | 14730 | / |
| Iron (mg/L) | 12.45 | 3 |
| Nickel (mg/L) | 0.729 | 0.5 |
| Suspended matter (mg/L) | 76770 | 35 |
| Polyphenol (mg/L) | 5610 | 0.3 |

RESULTS OF TREATMENT OF OLIVE MILL WASTEWATER BY ELECTRO FENTON
EFFECT OF THE APPLIED POTENTIAL DIFFERENCE.

The applied voltage to the electrodes is an important operation parameter of the electron-Fenton method. As described by [27], higher applied voltage leads to the generation of higher amounts of hydroxyl radicals from Fenton's reaction (Equation 6) :

$$Fe^{2+} + H_2O_2 \rightarrow Fe^{3+} + OH^{\circ} + OH^{-} \qquad (6)$$
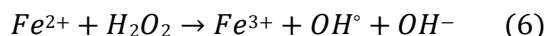
Figures 2 and 3 present the results of the removal rate of COD and polyphenols contents as a function of the applied potential difference, three values are tested (1.5, 2 and 2.5 V). At 1.5 V, the reduction rate of COD and polyphenols is 70 and 43% respectively, for a period of 90 min. The rise of the applied potential difference from 1.5 to 2 V increases the removal effectiveness of the studied parameters until 88 and 98% of COD and polyphenols respectively. For a potential difference of 2.5V, there is a decrease in the removal efficiency of the two pollutants studied (88% for COD and 98% for polyphenols). It was decided to carry out all the following experiments at a potential equal to 2 V.

In electrochemical systems, higher applied voltage causes a higher applied current density which corresponds to the electro-regeneration of ferrous ions from ferric ion (equation 7), the efficiency of Fenton chain reactions will increase [28, 29].

$$Fe^{3+} + è \rightarrow Fe^{2+} \qquad (7)$$
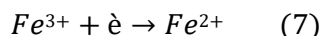
On the othor hand, when applying voltage increases, higher hydroxyl radical amount is formed. Thus increasing Fe$^{2+}$ ions and hydroxyl radical amount resulted in higher removal efficiency [30].

However, it is also noteworthy that a high potential cause a rapid oxidation of electrodes, leading to higher energy consumption. In addition, at high potential, there is a risk of loss of a large part of the heat energy in the system and the coalescence of gas bubbles, which leads to decrease the electro-fenton efficiency.
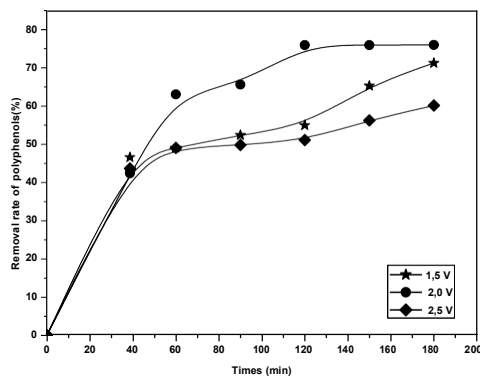
Fig 2. Removal of polyphenols v/s Contact Times, $H_2O_2$=30g/L at different of potentials applied.
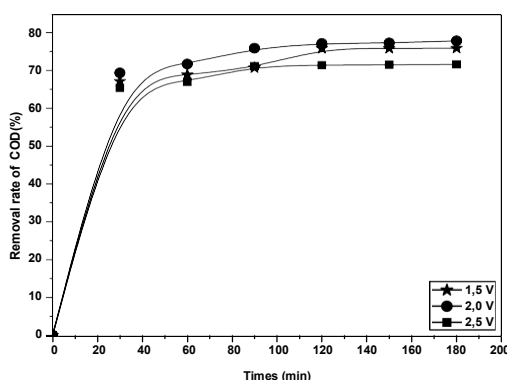


Fig 3. Removal of COD as function of times, $H_2O_2$=30g/L, at different of potentials applied.

EFFECT OF pH INITIAL

The effect of pH upon the efficiency of the electro-fenton process was carried out. Indeed, this parameter affects the iron ion solubility and the generation of OH°.

As shown in figures 4 and 5, the efficiency of the removal of COD and polyphenols from OMW had a maximum at pH = 3 (81 % for COD and 77 % for polyphenols after 120 minutes of contact time). Raising the pH of medium from 3 to 7 has decreased the removal of the sudied polltant ; for exemple, at pH= 7, the removal of polyphenols was reduced by more than half compared to pH equal to 3. Similar trends were reported for degradation of different organic compounds by classic Fenton, photo-Fenton, and electro-Fenton processes [31-36].

At higher pH non-reactive iron forms appear in wastewater: oxohydroxides or hydroxides precipitates and acts as radical scavengers. In this situation, the amount of iron available for radical generation is significantly lower than for the same dose, but in a lower pH. In addition the redox potential of OH° decreases with increasing pH [37].

On the other hand, lowering the pH below 3, results in the appearance of numerous iron aqua complexes and hydration $H_2O_2$ to $[H_3O_2]^+$, which is more stable and therefore less reactive with $Fe^{+2}$ [38]. Similar results we obtained by Peres et al [31] ; Lucas et al [34]; Bautista et al [32].
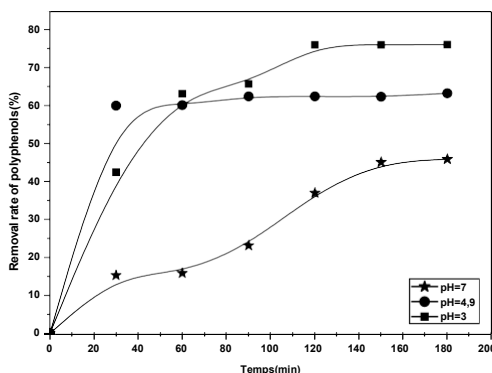
Fig 4. Removal of polyphenols as function of times.

The experimental results revealed that for a free pH (4.9) when time =60 minutes we have 60% removal of polyphenols after stabilizing as a function of time. In neutral medium (pH=7) there is a low removal of polyphenols due to the absence of $H^+$ in the reaction medium, but in acid medium after 120 minutes of contact time there is a 77% removal of polyphenols, this result can be explained by the regeneration of OH° hydroxyl radicals which are responsible for degrading polyphenols. As indicated in reaction (2), when the ferrous ion reacts with $H_2O_2$ it will generate strong oxidant hydroxyl radicals (OH°) [39].
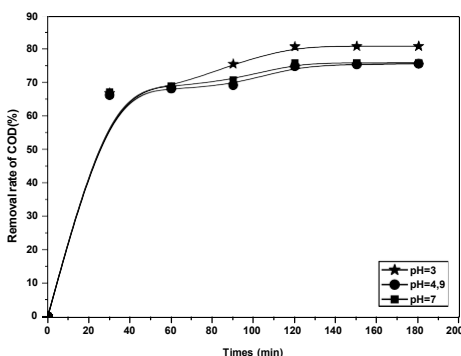


Fig 5. Removal of COD as a function of times.

IV. CONCLUSIONS

The present work studied the effectiveness of the electro-fenton process for the removal of the organic pollution of olive mill wastewater (COD and polyphenols) which far exceed the allowed standard limits.

It has been shown that the efficiency of the Electro-Fenton process depends on many operational parameters, such as : pH, and potential applied. According to the results obtained, the optimum operating conditions of the process for the elimination of organic pollution are the initial pH of 3 and applied voltage of 2 V. Under these conditions, COD and polyphenols removal efficiency of 81 and 77% respectively can be reached.

- The electro Fenton system can be a promising pretreatment process for olive mill wastewaters, because no expensive equipment is required.

- Finally, The effects and relevance of the results imply the need for the OMW to be treated before its discharge into the sewer system.

## REFERENCES

[1] A, Ruiz-Rodriguez , C, Soler-Rivas, I. Polonia and H. J. Wichers , *Effect of olive mill waste (OMW) supplementation to Oyster mushrooms substrates on the cultivation parameters and fruiting bodies quality*. International Biodeterior & Biodegr. 64(7) 638-645, 2010.

[2] G. Ait Baddi , M. Hafidi , V. Gilard and J.C evel,  *Characterization of humic acids produced during composting of olive mill wastes*, elemental and spectroscopic analyses (FTIR) and 13 C NMR), Agronomy, 23, 1-6, 2003.

[3] A. Samsunlu, O. Tunay , ALPK. *Characteristic and treatment of olive oil waste water, proceeding of the sixth control of industrial pollution symposium*, 3-5 June, Istambul, ITU, 93-99, 1998.

[4] J. Pérez, T. DeLa Rubia, O. Ben Hamman and Martinez J, *Phanerochaete flavidoalba laccase induction and modification of manganese isoenzyme pattern in decolorized olive oil mill wastewaters*. J. Applied and Environ. Microbiol. 27, 26–29, 1998.

[5]N. Zouari,  *Decolorization of olive oil mill effluent by physical and chemical treatment prior to anaerobic digestion*. J. Chem. Technol. Biotechnol. 73, 297-303, 1998.

[6]  D.P, Komilis , E. Karatzas and C.P, Halvadakis, *The effect of olive mill wastewater on seed germination after various pretreatment techniques*. J. Environ. Manage.74. 339–348, 2005.

[7]  D. Mantzavinos , N. Kalogerakis N, *Treatment of olive mill effluents. Part I: organic matter degradation by chemical and biological processes*—an overview, Environ. Int. 31, 289–295, 2005.

[8] E.J, Roseneeldt and K.G, Linden, *Degradation of endocrine disrupting chemicals bisphenol A, ethinyl estradiol, and estradiol during UV photolysis and advanced oxidation processes*. Environ. Sci. Technol. 38, 5476–5483, 2004.

[9] H. Zhang and Yamada , H. *Tsuno, Removal of endocrine-disrupting chemicals during ozonation of municipal sewage with brominated byproducts control.*Environ.Sci. Technol. 42, 3375-3380, 2008.

[10] M.R, Van den Heuvel, F.L, Leusch, S. Taylor, N. Shannon and A.B, Mckague, Assessment of the reproductive-endocrine disrupting potential of chlorine dioxide oxidation products of plant sterols. Environ. Sci. Technol. 40, 2594–2600, 2006.

[11]  B. Gözmen, M.A, Oturan, N. Oturan and O. Erbatur, *Indirect electrochemical treatment of bisphenol A in water via electrochemically generated Fenton's reagent*. Environ. Sci. Technol. 37, 3716–3723, 2003.

[12] A. Dirany, I. Sirés, N. Oturan, A. Özcan and M.A turan, *Electrochemical treatment of the antibiotic sulfachloropyriddazine: Kinetics, reaction pathways, and toxicity evolution*. Environ. Sci. Technol. 46, 4074–4082, 2012.

[13] J. Jiang ,S.Y. Pang, J. Ma and H.L, Liu, *Oxidation of phenolic endocrine disrupting chemicals by potassium permanganate in synthetic and real waters.* Environ. Sci. Technol. 46 1774–1781, 2012.

 [14] E. O, Oliveros,M. Legrini, T. Hohl and A.M, Müller Braun, *Industrial waste water treatment: large scale development of a light-enhanced Fenton reaction,* Chem. Eng. Process 36, 397–405, 1997.

[15] P. Canizares , J. Lobato, R. Paz, M.A. Rodrigo and C. Saez, *Advanced oxidation process for the treatment of olive oil mill wastewater*. Chemosphere. 67: 832–838, 2007.

[16] E. Brillas, J.C. Calpe and J. Casado, *Water Res.* 34 : 2253, 2002.

[17] Z.M, Qiang, H.J, Chang and CP, Huang, *Electrochemical generation of hydrogen peroxide from dissolved oxygen in acidic solutions.* Water Res.36, 85, 2002.

[18] S. Sharma , J.P. Ruparelia and M.P. Patel, A general review on Advanced Oxidation Processes for waste water treatment, institute of technology, nirma university. 382-481, 2011.

[19] I. Losito, A. Amorisco and F. Palmisano, *Electro-Fenton and photocatalytic oxidationof phenyl-urea herbicides: an insight by liquid chromatography-electrosprayionization tandem mass spectrometry.* Appl. Catal B: Environ 79. 224-236, 2008.

[20] M.A. Rodrigo, N. Oturan and M.A. *Oturan, Electrochemically assisted remediation of pesticides in soils and water: a review.* Chem Rev 114(17): 8720-8745, 2014.

[21] J. Rodier, *Analyse de l'eau. Eaux naturelles*, eau résiduaires, eau de mer, Dunod, Paris, 1996.

[23] S. Chou, Y.H. Huang, S.N, Lee, G.H. Huang, C. Huang, *Treatment of high strength hexamine-containing wastewater by Electro-Fenton method*. Water Res. 33, 751–759, 1999.

[24] E. Atmaca, *Treatment of landfill leachate by using Electro-Fenton method*, J. Hazard. Mater. 163:109–114, 2009.

[25]A. Ventura, G. Jacquet G, Bermond A, Camel V. *Electrochemical generation of the Fenton's reagent: application to atrazine degradation.* Water Res. 36, 3517–3522, 2002.

[26] Official Journal of the Algerian Republic. *Appendix of limit values for industrial liquid effluent discharge parameters.* JORA of, 26, 2006.

 [27] M. Panizza and G. Cerisola, *Electro-Fenton Degradation of Synthetic Dyes*, J. Water Research. 43, 339-344, 2009.

[28] P. V, Nidheesh and R, Gandhimathi, *Trends in Electro-Fenton Process for Water and Wastewater Treatment: an Overview*, Journal of Desalination. 299, 1–15, 2012.

[29] J. Cheng-Chun, J. Zhang, Progress, *Prospect in Electro-Fenton Process for Wastewater Treatment*, J.  Zhejiang University. 1118-1125, 2007.

[30] M.R. Samarghandi, A. Shabanloo, K. Shamsi, J. Mehralipour and Y. Poureshgh, *Performance of Electro-Fenton Process to Remove Cyanide from Aquatic Environments in Presence of Interfering Humic acids.* J. Health. 4. 4. 293-303, 2013.

[31] J.A.S, Peres, L. H. Melo de Carvalho, R.A.R. Boaventura, C.A.V. Costa, *Characteristics of p-hydroxybenzoic acid oxidation using Fenton's reagent*, J. Environ. Science and Health, Part A 39, 2897–2913, 2004.

 [32] P. Bautista, A.F. Mohedano, M.A. Gilarranz, J.A Casas and J.J Rodriguez, Application of Fenton oxidation to cosmetic wastewaters treatment, Journal of Hazard. Mater. 143 : 128–134, 2007.

[33]A. Luis, J.I. Lomdrana, F, Varona and A Menedez, *kinetic study and hydrogen peroxide consumption of phenolic compounds oxidation by Fenton's reagent*. Korean J. Chem, 26(1), 48-56, 2009.

[34] M.S. Lucas and J.A. Peres, *Removal of COD from olive mill wastewater by Fenton's reagent: Kinetic study*. J. Hazard Mater. 168, 1253–1259, 2009.

[35] A. Babu ponnusami and K Muthukumar, *Advanced oxidation of phenol: A comparison between Fenton, electro Fenton, sono-electron-Fentonand photo-electro-Fenton processes*. J.Chem. Eng, 183: 1-9, 2012.

[36] M. Gar Alalm, A. Tawfik and S. Okawara. *Deradation of four pharmaceutical by solar photo- Fenton process : Kinetics and costs estimation* . J. Environ. Chem. Eng. 3(1), 46-51, 2015.

[37] A. Bapu ponnusami and K Muthukumar, *A review on Fenton and improvements to the Fenton process for wastewater treatment*. J. Environ. Chem. Eng. 2. 1. 557-572, 2014.

[38] J. Bogacki, P. Marcinowski and J. Naumczyk, *Cosmetic Wastewater Treatment Using Coagulation and Fenton Processes, Challenges of Modern Technology*. 6. 4. 36-42, 2015.

[39] S. Khoufi, F. Aloui and S. Sayadi, *Treatment of olive oil mill wastewater by combined process electro-Fenton reaction and anaerobic digestion*. Water research. 40, 2006.

# Effect of envelope structure on energy consumption in Algeria

Horiya Benharchache [#1], Fouad Khaldi[*2], Morad Hanfer[#3]

[#] *Laboratory of Physics and Applied Energy (LPEA), University Batna-1-, Batna 05000, Algeria,*

*Faculty of Natural Sciences, University of Batna 2,Constantine way 53, Fesdis, Batna 05078, Algeria*

[1]*horiya.benharchache@univ-batna.dz*

[3]m.hanfer@univ-batna2.dz

[*] *Higher National School of Renewable Energy, Environment & Sustainable Development, Batna 05000, Algeria*

[2]fouadkhaldi@gmail.com

*Abstract*— **In this study we examine the case of a simple architecture building (office) occupied by 4 people, contains two identical windows and one door. The optimization of the energy consumption of our building is the result of a series of parametric simulations, conducted by the EnergyPlus software, depending on weather conditions of three cite in Algeria- Algeria has three main climatic zones: Mediterranean(Algeria), Continental (Batna) and Saharan (Tamarnasset)- . At the end of this study the relevant selection is identified on the envelope structure (material and thickness).**

*Keywords*— **Building; Energy efficiency; EnergyPlus; Algeria; Thermal Insulation**

## I. INTRODUCTION

The building sector accounts for about 2/3 of the energy consumption in the world. For example in the UK, the building sector is responsible for 47% of final domestic consumption in this country [1]. The same in France, regarding the consumption of energy, building only consumes 46% of the final energy to which is added 3.8% due to construction sites [2]. The portions of the building sector consumption is almost similar in most countries, for example in the European Union and from the key word in energy efficiency in Europe of 2007, the building sector only represents 35% of final energy consumption[3,4]. This important share of energy comes from fossil fuels which are likely to be depleted. For that reason, there is a need to develop a building in response to the up skilling in energy performance design while providing indoor comfort with low energy consumption.

In Algeria, the building sector, in addition to residential and tertiary sectors, represents on its own 41% of final energy consumption according to data provided by the APRUE [5] (Algerian National Agency for the Promotion and Rationalization of Energy Use).
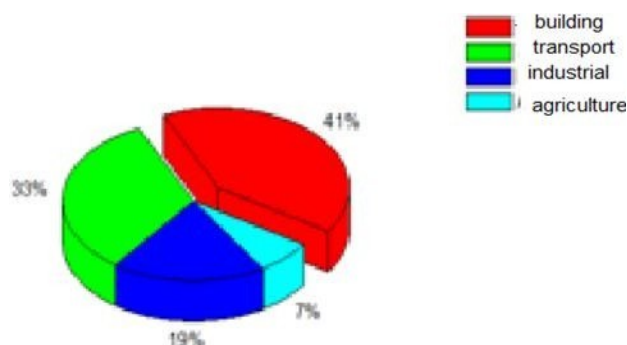


Fig 1: Energy consumption by sector

Environmental concern of the building sector has led to a variety of methods in order to meet two primary requirements: to reduce energy consumption and the impacts on the external environment and ensure healthy and comfortable indoor environments knowing that we spend 80% of our time inside the building. There are several outlines of research on improving the energy performance of buildings, the two main ones being energy efficiency measures and the use of renewable energy. Our study in this paper is about energy efficiency. The study aims to

optimize the energy consumption of a building, it is about an office for four persons, and it contains two identical windows and one door.

The optimization of the energy consumption of the said office is the result of a series of parametric simulations, conducted by the software: EnergyPlus [6] depending on weather conditions (Algiers, Batna Tamanrasset) and interior comfort. At the end of this study, we shall identify the relevant choices concerning the structure of the envelope (materials and thickness).

At the national scale, it is noted that APRUE [5] launched the ECO BAT program, its goal is the realization of lodgments which ensure an optimization of indoor comfort by reducing energy consumption mainly due to heating and air conditioning by 40% . APRUE already launched under the National Energy Management Program, PNME 2007-2011, the realization of 600 lodgments HPE "high energy performance", There is Also. The 600 lodgments program on most territory of country (1700KWh/m$^2$/year at North and 2263KWh/m$^2$/year in the South) [7] .

The energy issue is a priority in all economic and political strategies in the world, and Algeria has adapted its legislation to implement all the means and techniques for a better energy management, adding that this program, committing both sectors of Housing and Energy through APRUE, aims to encourage passive conceptual strategies of energy saving for housing.

The energy-saving initiatives such as the program "ECO Light", consist of promoting efficient lighting in households. In addition to these programs, APRUE is currently developing another project called "ALSOL" consisting of promoting solar water heater.

## II. MODEL GEOMETRY:

The study is mainly based on a single-area rectangular building. The room has an area of 6m*8m and a height of 3m. The building contains two identical windows of 3m wide and 1.5m height and a door of 2m wide and 2.5m height, the building is an office for four persons.
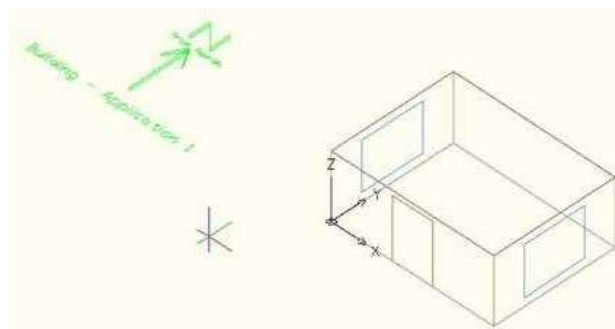


Fig 2: building geometry

The windows of the building occupy 10.71% of the total area of the exterior walls. This area contains two identical double glazed windows of clear glass with a thickness of 0.003 m and a thermal conductivity of 0.9 W/mk, which are located in the eastern and western façade as shown in Fig 2. The door (opaque timber 0.05m thick and K = 0.15W/m k) is in the south facade.
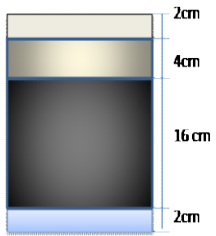
The composition of the components of the envelope -the floor is assumed adiabatic-, these dimensions and thermal characteristics of single-area model are presented in the table below:

TABLE I
THERMODYNAMIC CHARACTERISTICS OF THE WALL COMPONENTS

| Component | E | $\rho$ | K | Cp | Roof's Scheme |
|---|---|---|---|---|---|
| | (m) | (kgm$^{-3}$) | (wm$^{-1}$k$^{-1}$) | (j kg$^{-1}$ k$^{-1}$) | |
| bastard Mortar | 0.02 | 1903 | 1.15 | 1080 | |
| Solid concrete | 0.04 | 2353 | 1.75 | 1080 | |
| Compression slab | 0.16 | 1463 | 1.45 | 1080 | |
| Plaster | 0.02 | 800 | 0.35 | 9.36 | |

TABLE II
THERMODYNAMIC CHARACTERISTICS OF THE ROOF COMPONENTS



| Component | E | ρ | K | Cp | Roof's Scheme |
|---|---|---|---|---|---|
| | (m) | (kg.m⁻³) | (w.m⁻¹.k⁻¹) | (j. kg⁻¹.k⁻¹) | |
| bastard Mortar | 0,02 | 1900 | 1,15 | 1080 | |
| Solid concrete | 0,04 | 2350 | 1,75 | 1080 | |
| Compression slab | 0,16 | 1460 | 1,45 | 1080 | |
| Plaster | 0,02 | 800 | 0,35 | 936 | |

## A. Internal Gain

The building is illuminated with 1000W lamps, so the building is characterized by a light density of 20,83W/m2. The building (single area) is a working place for four persons, so the area is characterized by an occupancy rate of about 12m2/person. The human being is a heat-producing seat as he seeks to maintain constant temperature regardless of external conditions. The dynamic thermal simulation with EnergyPlus incorporates EN ISO 7730[8-10], therefore the amount of heat generated by the person working in the office is taken in consideration. All equipment used in this building and their powers are given in Table.3 the area is characterized by a density rate of the devices used 5W/m2.

TABLE III
ELECTRICAL EQUIPMENTS USED IN THE OFFICE

| EQUIPEMENT | TOTAL POWER [W] |
|---|---|
| Lighting | 1000 |
| 4 Computers | 4*50 |
| 4 Box internet | 4*10 |

## B. Heating and cooling system in the building

The level of temperatures within a habitat depends mainly on the external temperature, internal heat gains, solar gains, ventilation; it generally depends on climatic conditions of each country.In this study, we perform simulations to study more conditioning variants to determine the appropriate solution to the energy level. We compare the energy consumption required to heat and to cool the habitat to a set temperature equal to 20°C, 24°C, respectively, according to different suggested solutions. The study concerns the energy simulation in three different geographical sites.

The aim is to obtain a comfortable temperature in winter (20°C) and a lowering of the temperature from the outside in summer (24°C), therefore; it is considered that there is a heating system and ventilation and air-conditioning -HVAC- installed in the office to ensure the heating and cooling of the office under study. The two functions of heating and cooling are simplified treatments applied to the ambient air in the habitat. They are provided by two types of heat exchangers called heating and cooling coils. Both types of coils use air as a coolant. The physical characteristics of this fluid are shown in the following table:

TABLE IV
*PHYSICAL CHARACTERISTICS OF HEAT TRANSFER FLUID*

| | Unit | Heating coil | Cooling coil |
|---|---|---|---|
| **Temperature** | °C | 50 | 13 |
| **Absolute Humidity** | Kg $H_2O$/Kg air | 0,015 | 0,010 |

The criteria affecting energy efficiency, severe climatic data (different sites), design constraints and guidance will be incorporated into this study

## III.     RESULTS AND DISCUSSION

The study concerns the following parameters:

### A.  Effect of climate on annual energy consumption

Algeria has three main climatic zones: Mediterranean, Continental and Saharan Fig 3. The Mediterranean climate is characterized by a mild climate in winter and hot and humid in summer with slow variations in temperature between seasons and low fluctuations between day and night. The continental climate is characterized by hot weather in summer and cold in winter with large variations in temperature between seasons. The Saharan climate is characterized by a warm climate throughout the year but with very strong fluctuations in temperature between day and night.
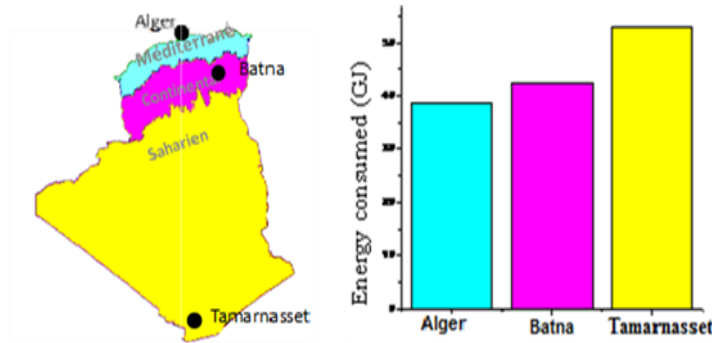


Fig 3: Energy consumption in climatic zones of Algeria

The energy consumption of the same building mentioned in the three climate zones is given in Fig 3. In Saharan climate (Tamarnasset) the building consumes more energy than in the continental climate (Batna) and even more than in the Mediterranean climate (Algiers). In fact, total consumption, in heat, air conditioning and power in the climate of the city of Tamarnasset is estimated 52,96GJ, in the continental climate, the consumption is 42,37GJ. Finally in the Mediterranean climate, the building consumes 38,56GJ.

According to Fig 4 we notice that the consumed electric load is constant, the same operating conditions for lighting, in the three zones because in this study we are just interested in the internal temperature change of the area that directly affects the heating and cooling load. For example in the case of Batna which is characterized by a continental climate, we notice that the heating and cooling load is almost similar. On the contrary Tamarnasset is situated in the Sahara which is a very hot climate, which results in a very dominant cooling load with 49.01 GJ compared to the heating load which is estimated by 0.21 GJ.
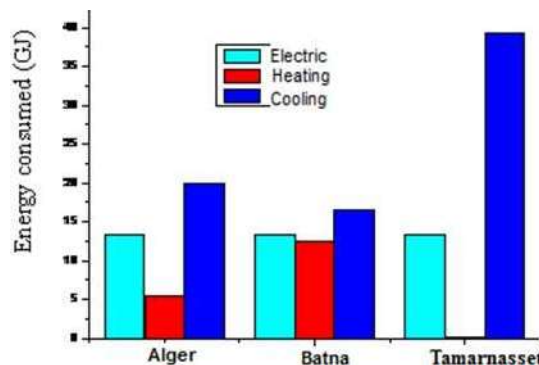


Fig 4: Energy consumed by load type in three areas

*B. Effect of thermal insulation on the annual energy consumption*

The envelope of the building acts as a thermal barrier since the analysis of studies concerning the design of buildings show the tendency to reduce energy needs through optimization of the envelope.

The comparison examines two scenarios for the envelope of an office. In scenario 1 (building materials shown in Table 1 and 2), without thermal insulation and the glazing is simple. In scenario 2 (the envelope is equipped with a thermal insulation Polyurethane (E= 0.05m, $\square$=35Kg/m³, $\square$=0.0245 W/ m K et $C_p$=1404 j. kg⁻¹. k⁻¹) and the glazing is double. Fig 5 indicates that the total energy consumed by the insulated office (scenario 2) in Algiers is evaluated by 33.56GJ by contrast; the non-insulated office (scenario 1) consumes 38.65 GJ annually. Thus, the insulation of the office allows to reduce the total consumption of 5.1GJ, comparing to non-insulated office. This difference of 13.20% is due primarily to the increase in the total resistance of the opaque and glazed surfaces. As well as the cities of Batna and Tamarnasset; the integration of thermal insulation reduces the annual energy consumption nearly by 24.42% and 7.45% respectively.
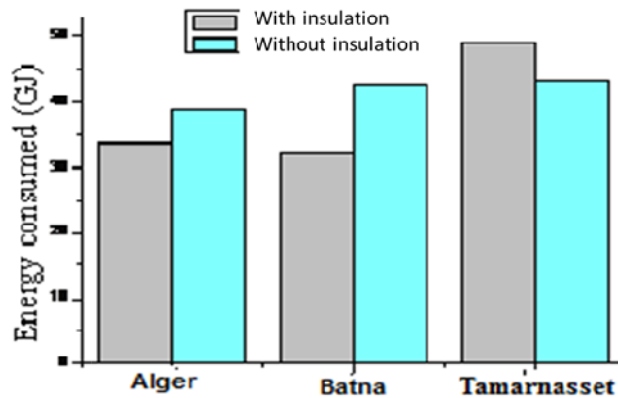


Fig 5: Effect of the thermal insulation on the energy consume

To study the effect of thermal insulation in winter and summer, the study concerns the case of the city of Batna. Fig 6 A-B represents the evolution of the heating and cooling load of the building for the months of the year. We find that the integration of the insulation reduces the heating load in winter and also in spring and autumn. In summer it is noted that the thermal insulation also reduces the cooling load , by contrast, in spring and autumn it helps increase the cooling load as shown in Fig 6-B.
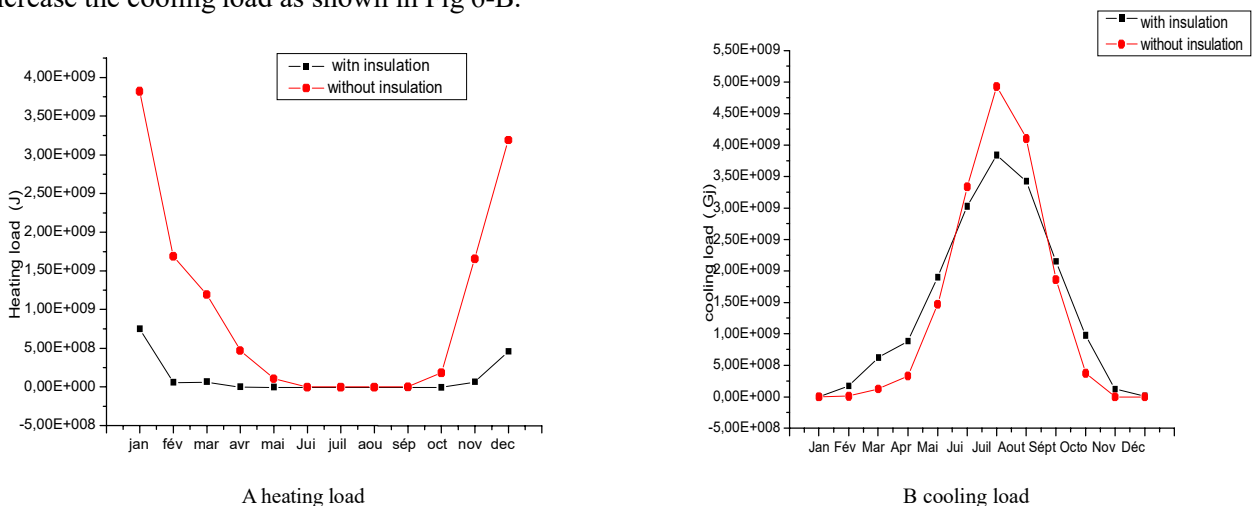


A heating load



B cooling load

Fig 6 A-B: Effect of the insulation on the evolution of the heating and cooling load

*C.  Effect of the wall thickness on the annual energy consumption*

In this case we evaluate the effect of different thicknesses of Brick on the annual energy consumption of the building located in Batna. Several values of thickness were verified in this study. The results show the relationship between different thicknesses and the annual energy consumption, it indicates that the greater the  thickness increases, the lesser the energy consumption decreases. In fact, increasing the thickness of the shell helps  increase the thermal resistance of the latter, thus it makes it possible to reduce the heat losses to the outside and also the annual energy consumption of the building.

Fig 7 shows the influence of the thickness of  walls  on  the  energy  consumption  of  the  office  under  study. This graph shows that the increase of the thickness of walls allows a significant reduction in the annual energy consumption of the building.
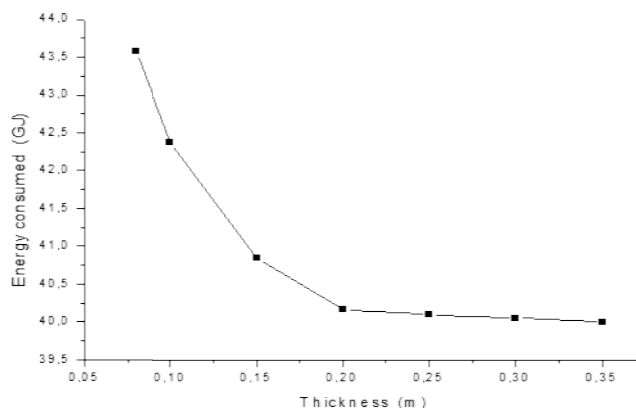


Fig 7: Effect of the thickness on the energy consumption

The optimization of the wall thickness helps slightly lower the demand of energy in the building. The wall (with brick 0.10m thick) corresponds to the high value of energy consumption. The wall (with brick 0.20 m thick) permits an energy performance improvement of the building. The more the thickness increases from 0.20 m, the energy consumption remains insensitive. Therefore, we can say that the ideal thickness of the wall (brick with 0.20m thick) and for economic reasons also is that of 0.20 m brick.

## IV.    CONCLUSIONS

This work studied the energy of buildings. This is a first step in the development of knowledge and skills  to design energy-efficient of buildings. By simulation using EnergyPlus software, we considered the case of a single architecture building. It is a desk in one piece occupied by 4 people. We examined the effects of the envelope structure (building materials and exterior wall thicknesses) on the annual energy consumption in terms of heating, cooling and electricity. We also studied the energy behavior of the building in three sites, geographies and climates very different: Algiers, Batna and Tamanrasset.

The simulation results showed that a wrong choice of the material of the building envelope can increase energy consumption in Tamanrasset because the materials are not suitable for this climate. Thus, the integration of thermal insulation to the desktop reduces the total energy consumption by 25% in the conventional climate.

## REFERENCES

[1]  Wang, L., J. Gwilliam, and P. Jones, Case study of zero energy house design in UK. Energy and buildings, 2009. 41(11): p. 1215-1222.

[2]  ADEME. Agence de l'Environnement et de la Maitrise de l'Energie. L'efficacité énergétique dans l'Union européenne. www.ademe.fr

[3]   Anh Dung TRAN LE, 2010. Etude des transferts hygrothermique dans le béton de chanvre et leur application du bâtiment. Thèse de doctorat. Université de Reims Charmpagne-Ardenne.

[4]   Laponche, Bernard, Mathieu Richard, Sophie Attali, and Webmestre Global Chance. "Les Politiques D'efficacité Énergétique De L'union Européenne–Global Chance." (2022).

[5]   APRUE, consommation Energétique Finale de L'Algérie, 2017. Available: http www.aprue.org.dz

[6]   EnergyPlus Calculations, Available: http www.enegyplus.gov

[7]   Missoum, M, A Hamidat, L Loukarfi, and K Abdeladim. "Impact of Rural Housing Energy Performance Improvement on the Energy Balance in the North-West of Algeria." *Energy and Buildings* 85 (2014): 374-88.

[8]   Nicolas MOREL, Edgard GNANSOUNOU, 2009. Energétique du bâtiment. École Polytechnique Fédérale de Lausanne.

[9]   Fatima Zohra CHAFI, 2010. Développement d'un modèle zonale pour la simulation thermo aéraulique des bâtiments multizones. Thèse de doctorat. Université du Québec

[10]  Leen PEERES, Richard de DEAR, Jan HENSEN, William D'HAESELLER, 2009. Thermal comfort in residential buildings: Comfort values and scales for building energy simulation. Applied Energy, v. 86 (09) 772-780

# Modelling under Proteus of a Photovoltaic System

Mourad Talbi[#1], Abdelmajid Zairi[*2], Fehri Krout[#3]

[#]*Laboratoire de Maîtrise de l'Energie Eolienne et de Valorisation Energétique des Déchets (LMEEVED),*

*Laboratoire de Nanomatériaux et Systèmes pour Energies Renouvelables (LaNSER), Centre de Recherches et de Technologies de l'Energie de Borj Cedria*

*Hammam Lif, B.P N°95 2050, Tunisia*

[1]talbi1969@yahoo.fr

[3]fehry_krout@yahoo.fr

[*]*Laboratoire Photovoltaïque, Centre de Recherches et de Technologies de l'Energie de Borj Cedria*
*Hammam Lif, B.P N°95 2050, Tunisia*

[2]zairi.zairi73@gmail.com

*Abstract*— **In this paper, the modelling of a Photovoltaic (PV) system is performed under Proteus. This PV system is composed by a PV Module, a DC-DC boost converter and a load that can resistive or inductive (a DC Motor) or capacitive (Battery). This DC-DC boost converter is controlled by a Maximum Power Point Tracking (MPPT) command by employing an Incremental Conductance (IC) one. Also, this DC-DC boost converter is controlled via Pulse Width Modulation (PWM) generated from the used Arduino uno which is modelled via Proteus. The Simulation results show the efficiency of the MPPT controller (IC) in tracking the MPP and this in case where the climatic conditions are unchanging or changing over time.**

*Keywords*— **PV Module, Proteus, DC-DC Converter, IC, PWM**

## I. INTRODUCTION

Solar energy is clean, inexhaustible and free as one of the most important renewable energies. The application of Photovoltaic (PV) system becomes more and more largely, the principal application of PV systems is in either stand-alone or grid-connected configurations [1]. Solar PV generation is an important form of solar energy employment, it is one of the most promising power generation technologies due to restrictions from raw materials and application environment. There are two major technical difficulties of PV generation systems in the application. Firstly, the conversion efficiency of electric power generation is low. In general, laboratory cell effectiveness is approximately 18–20% and the commercial cell efficiency is about 13–18%. Secondly, the output power of PV cellsis influenced by the radiance and ambient temperature. To overcome these problems, we should track the maximum power point of the PV cells' output power. Consequently, this ameliorates the effectiveness of the PV power generation system, reducing the cost of power production. The power output of any PV module is a function of environmental variables such as insolation (incident solar radiation), temperature, shading (from cloud cover and trees) and load conditions [2]. Although, irradiance and temperature conditions are the prime variables. Consequently, the current-voltage (I-V) characteristics and the power-voltage (P-V) characteristics of solar modules are influenced by the inrradiance and temperature levels. The output current and hence the output power increase linearly with insolation while the output voltage and hence the output power decreases with increasing temperature. These two environmental variables change constantly throughout the day and consequently provide rise to the intermittency and variability associated with the generation of energy by solar modules. Though, the PV module owns a single operating point where the values of the current and voltage of the module result in a Maximum Power output [2, 3, 4]. Figures 1 and 2 illustrate such an operating point for the I-V and P-V characteristics.
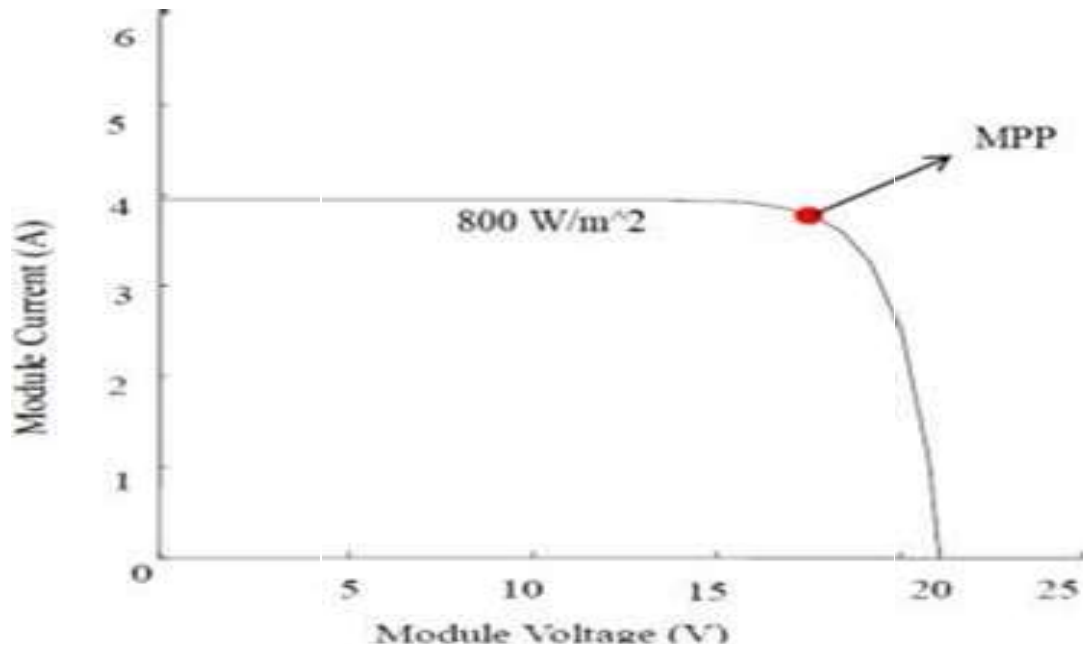
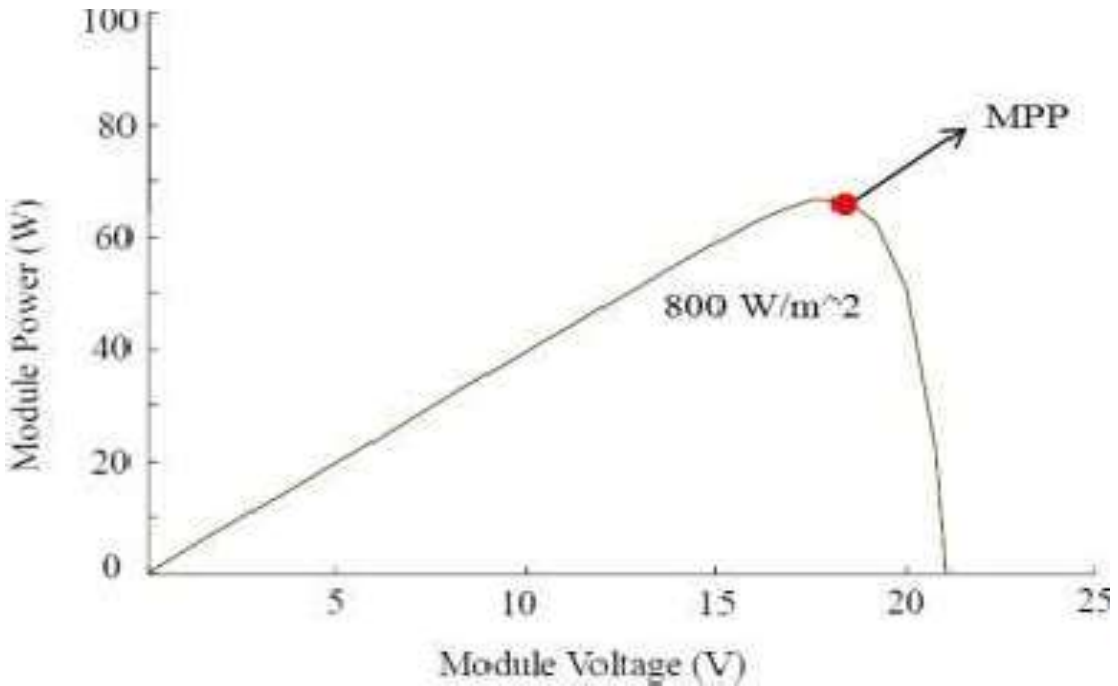Fig. 1. The $I - V$ Characteristic of a PV Module, on which is marked by red color the MPP at $800\,W/m^2$ [1]



Fig. 2. The $P - V$ Characteristic of a PV Module, on which is marked by red color the MPP at $800\,W/m^2$ [1]

As it is shown in these Figures, such a Maximum Power Point (MPP) occurs at the knee of the curve. At this point, the module produces the maximum power from the source to its load [4]. Ensuring that the PV module operates at this desired MPP and hence at the highest effectiveness, requires a robust control strategy to track this ever-changing point [5, 6]. This tracking task is often implemented using maximum power point tracking (MPPT) control algorithm-several of which exist in the literature [7, 8]. The extraction of this maximum power is often done in conjunction with a power conditioning unit (DC-DC or DC-AC converters) as the interface between the PV modules and the system electrical load [2, 9]. Such a power conditioning unit, moreover to ensuring operation at the

MPP, should also garantee the regulation of the output voltage and current irrespective of load and input voltage variations. In this paper, we perform the modelling and Real-Time Implementation of a Photovoltaic (PV) System. The latter includes a PV panel, a DC-DC boost converter and resistive load. The rest of this paper is organized as follows: in section 2 we will detail the modelling the PV system under Proteus and Labview. In section 3, we will detail the real-time implementation of this modelled PV system using Arduino uno. In section 4 we will present results and discussion and we will conclude in section 5.

## II. THE MODELLING UNDER PROTEUS OF THE PV SYSTEM

In this section we will detail the modelling of a PV system. This modelling is performed under ISIS (Protues) and Labview. In Figure 3, is illustrated the modelling of this PV system. The latter includes a PV panel, a DC-DC boost converter and resistive load. This DC-DC boost converter is controlled by a Maximum Power Point Tracking (MPPT) controller using Perturb and Observe (P&O) or Incremental Conductance (IC) algorithm. Also, this DC-DC boost converter is controlled via the Pulse Width Modulation (PWM).
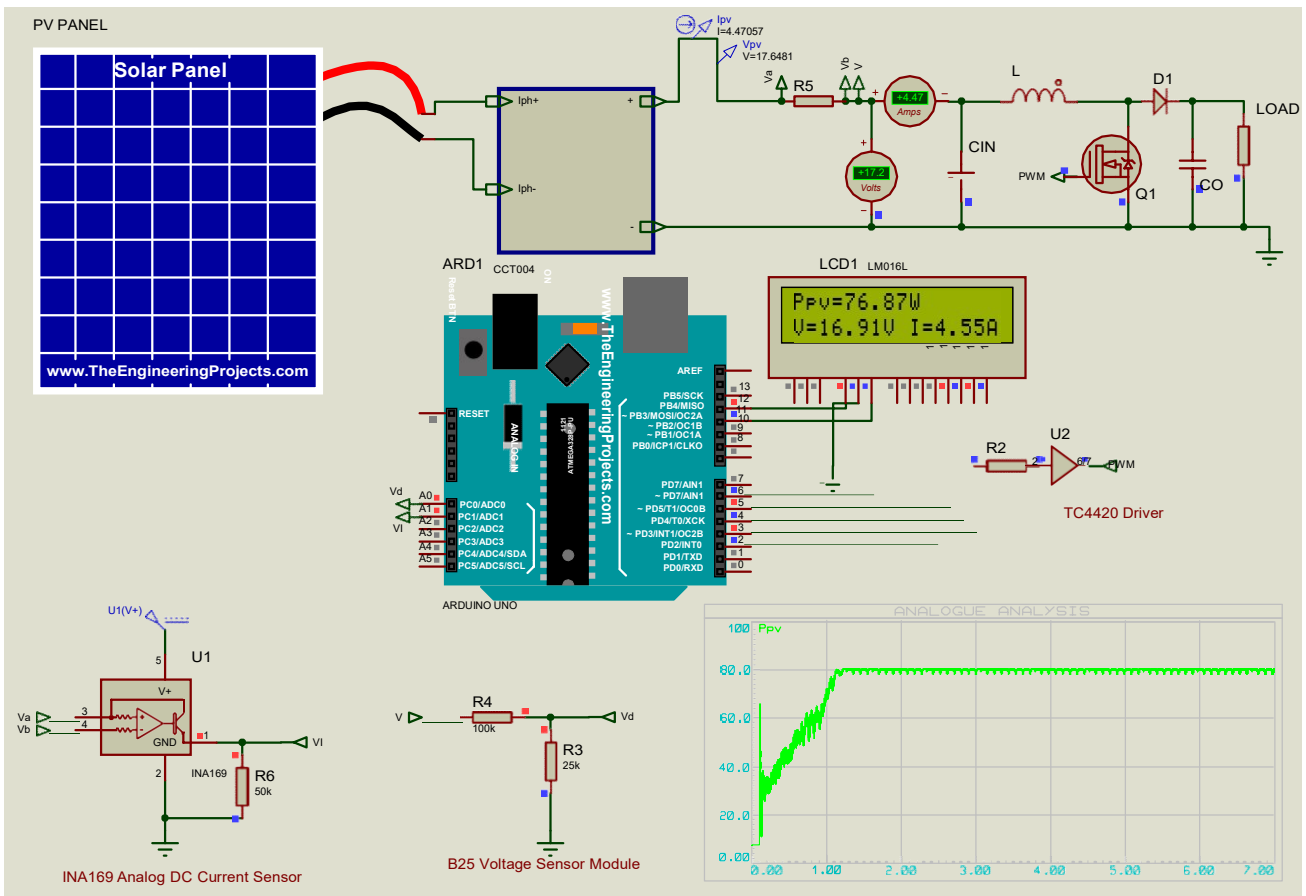


Fig. 3. Modelling of a PV System under Proteus

As illustrated in Fig. 3, this modelling uses the model of the Arduino Uno card and the Current Sensor and the Voltage Sensor. In Fig. 3, is also illustrated the curve of the temporal variation of the Power delivered by the used PV panel.

### A. The Incremental Conductance controller

In this section we will deal with one conventional Maximum Power Point Tracking (MPPT) controller which is applied here in our PV system (Fig. 3). This MPPT controller is the Incremental Conductance (IC) and its flowchart is given at Fig. 4.
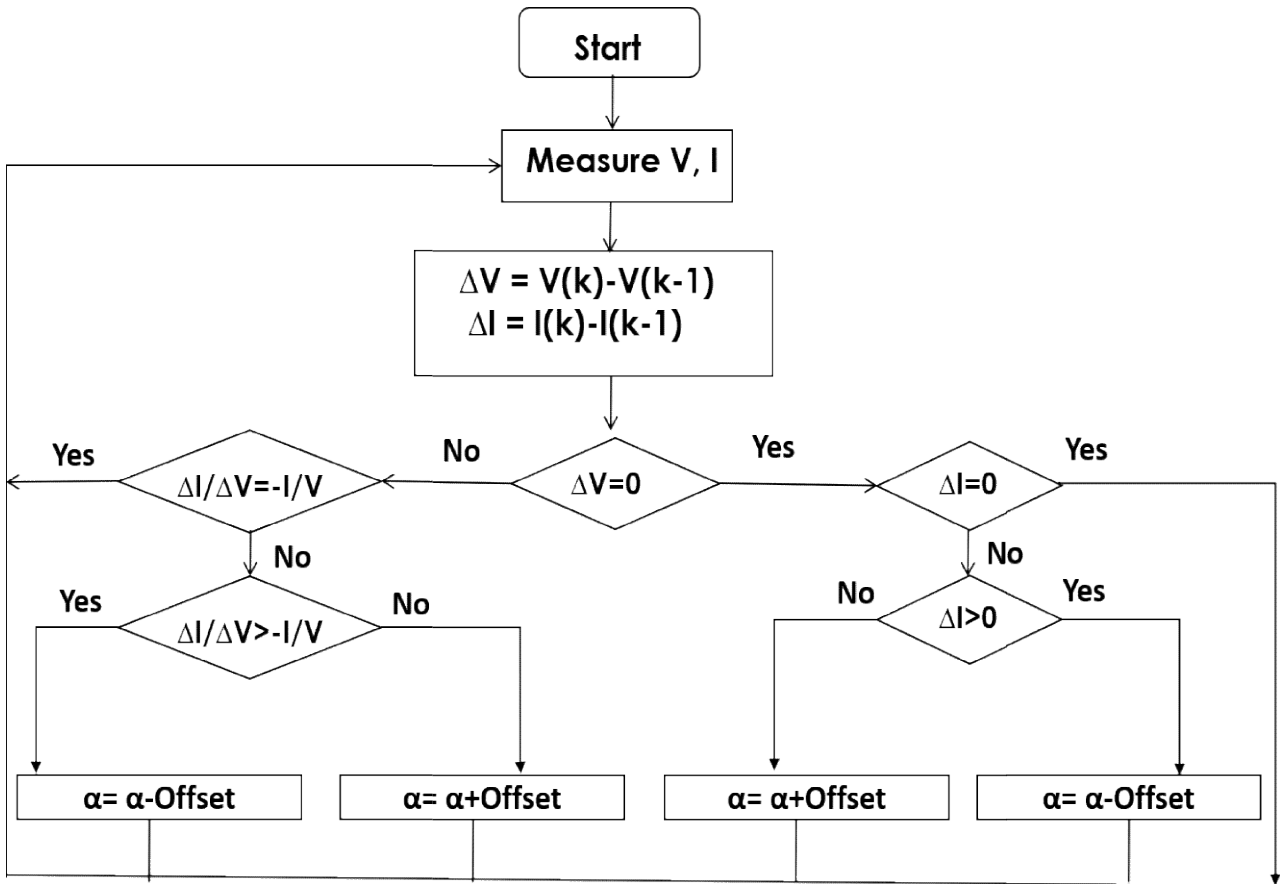
Fig.4. The Flowchart of the used IC Command [10]

### III. THE MODELLING UNDER PROTEUS OF THE PV SYSTEM

In this work we will present the different results obtained from simulations of our PV System modelled under Proteus (which is illustrated at Fig. 3). In Fig. 5, the P-V and I-V Characteristics are illustrated.



(a)                                                                                      (b)
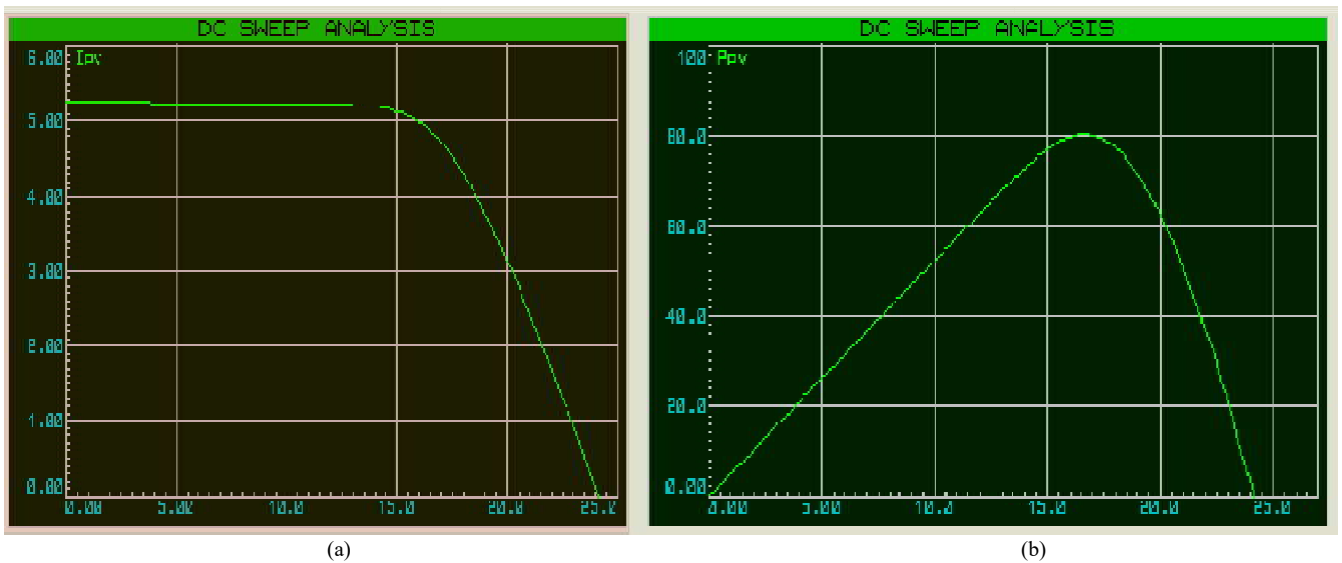
Fig.5. (a) P-V Characteristic, (b) I-V Characteristic

As illustrated in Fig.5 (b), the maximum of the Power provided by the PV panel used in our PV system (Fig. 3), is equal to 80 Watt. Fig.6. illustrates the curve of temporal variation of the Power provided by the PV Panel used in our PV system (Fig. 3).
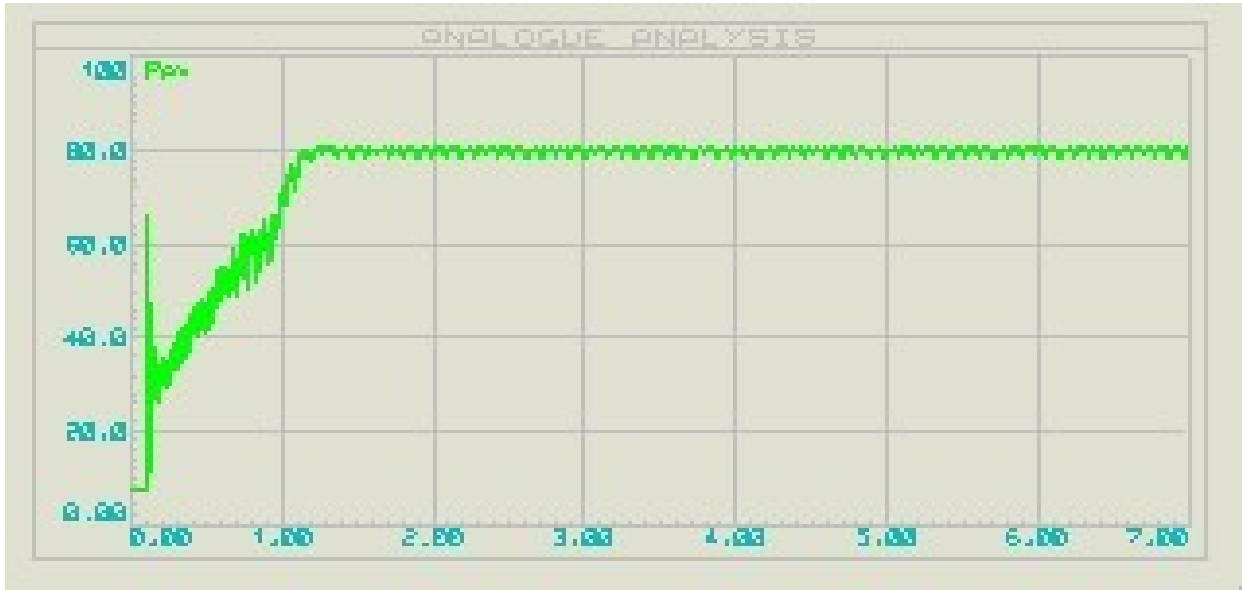


Fig.6. Curve of Temporal Variation of the Power provided by the PV Panel used in the modelled PV system (Fig. 3). This curve is obtained in Standard Conditions (T = 25ºC and G= 1000 Watt/m²)

According to Fig.6, we have oscillations around the maximum power (80 Watt) provided by the PV panel used in our PV system (Fig. 3). Consequently, the IC controller permit to track efficiently the MPP (Maximum Power Point).

Fig.7. illustrates the curve of temporal variation of the Power provided by the PV Panel used in our PV system (Fig. 3). This curve is obtained in case where the insolation takes the value G1= 1000 Watt/m2 and then the value G2 =364 Watt/m2 after a period of time. Consequently, we have two values of the maximal power provided by the PV panel used in our PV system (Fig. 3). These values are respectively 80 Watt in case of STC (T=25ºC and G1= 1000 Watt/m²) and 34.2 Watt in case where: T=25ºC and G2 = 364 Watt/m².



Fig.7. Curve of Temporal Variation of the Power provided by the PV Panel used in the modelled PV system (Fig. 3). This curve is obtained in case where the insolation takes the value G1= 1000 Watt/m2 and then the value G2 =364 Watt/m2 after a period of time

According to Fig.7, we have oscillations around the maximum power (80 Watt) provided by the PV panel in case of STC (T=25ºC and $G_1$= 1000 Watt/m$^2$) and after a period of time, we have oscillations around the maximum power (34.2 Watt) in case where we have (T=25ºC and $G_1$= 364 Watt/m$^2$, Consequently, the IC controller permit to track efficiently the MPP (Maximum Power Point).

## IV. CONCLUSIONS

In In this paper, the modelling of a Photovoltaic (PV) System is performed under Proteus. This PV system is composed by a PV Module, a DC-DC boost converter and a load that can resistive or inductive (a DC Motor) or capacitive (Battery). This DC-DC boost converter is controlled by a Maximum Power Point Tracking (MPPT) command by employing an Incremental Conductance (IC) one. Also, this DC-DC boost converter is controlled via Pulse Width Modulation (PWM) generated from the used Arduino uno which is modelled via Proteus. The Simulation results show the efficiency of the MPPT controller (IC) in tracking the MPP and this in case where the climatic conditions are unchanging or changing over time.

## REFERENCES

[1] Ali Moghassemi, Shayan Ebrahimi, Javad Olamaei. MPPT and Current Mode Control Methods for PV Modules: A Review and A New Multi-Loop Integrated Method. Signal Processing and Renewable Energy. June 2020, (pp. 1-22).

[2] M. Veerachary. Power Tracking for Nonlinear PV Sources with Coupled Inductor SEPIC Converter. IEEE Trans. Aerospace & Electronics Systems, vol. 40, no. 3, pp. 1019-1029, 2005.

[3] M. A. Danandeh, S. M. Mousavi G. Comparative and Comprehensive Review of Maximum Power Point Tracking Methods for PV Cells. Renewable and Sustainable Energy Reviews, vol. 82, no.3, pp. 2743-2767, 2018.

[4] K. N. Hasan. Control of Power Electronic Interfaces for Photovoltaic Power Systems. M.S thesis, Department of Electrical Engineering, University of Tasmania, Hobart, Australia 2009.

[5] S. Jianping, L. Xiaozheng. A New MPPT Control Strategy. Proc. Intl Conf. on Mechatronic Science, Electric Eng. & Computer (MEC), pp. 239-242, 2011.

[6] B. Liu, S. Duan, F. Liu, P. Xu. Analysis and Improvement of Maximum Power Point Tracking Algorithm Based on Incremental Conductance Method for Photovoltaic Array. Proc. 7th Intl Conf. on Power Electronics & Drives Systems, pp. 637-641, 2007

[7] T. Esram, P. L. Chapman. Comparison of Photovoltaic Array Maximum Power Point Tracking Techniques. IEEE Trans. Energy Conversion, vol. 22, no. 2, pp. 439-449, 2007.

[8] M. K. Hossain, M. H. Ali. Overview on Maximum Power Point Tracking (MPPT) Techniques for Photovoltaic Power Systems. International Review of Electrical Engineering (IREE), vol. 8, no. 4, pp. 1363-1378, 2013.

[9] R. Faranda, S. Leva. Energy Comparison of MPPT Techniques for Photovoltaic Systems. WSEAS Trans. Power Systems, vol. 3, no. 6, 446-455, 2008

[10] Saad Motahhir, Abdelilah Chalh, Abdelaziz El Ghzizal, Aziz Derouich. Development of a low-cost PV system using an improved INC algorithm and a PV panel Proteus model Journal of Cleaner Production Volume 204, 10 December 2018, Pages 355-365

# Evaluation of Ingestion Effective Dose in Drinking Bottled Mineral Water in Morocco by Gross Alpha and Gross Beta Activity Concentrations

M. Laassiri[1]*, H. Ait Bouh[2], N. Ziad[3], J. Naouli[2], A. Laissaoui[2]

[1]*Faculty of Sciences, Ibn Tofail University, Kenitra, Morocco.*
[2]*Centre National de l'Energie, des Sciences et des Techniques Nucléaires (CNESTEN), B.P.1382 R.P., 10001 Rabat, Morocco.*
[3]*Ecole Nationale des Sciences Appliquées, Ibn Tofail University, Kenitra, Morocco.*

* *lassirimeriem@gmail.com (corresponding author)*
*haitbouh@gmail.com*
*nziad19@yahoo.fr*
*naouli@cnesten.org.ma*
*laissaoui@cnesten.org.ma*

**Abstract**
While most Moroccan people have access to safe drinking water, many prefer the perceived purity and potential health benefits of bottled mineral water. It is acceptable to assume that some natural radionuclides will be present in trace concentrations in drinking water, such as mineral water that has been bottled. Contaminants in water may not always indicate that it poses a health danger. This work utilized the ISO 11704:2018 method to determine the gross alpha and gross beta activity concentrations of 13 commercially bottled mineral waters obtained from Moroccan markets through Liquid Scintillation Counting (LSC). Although gross alpha and gross beta activity concentrations varied significantly between samples, they were all below the World Health Organization's recommended values of 0.5 and 1 Bq.L$^{-1}$ for drinking water quality. Gross alpha and Gross beta activities are used to evaluate the annual effective dose of radionuclides in mineral water, which complies with the total indicative dose set at 0.1 mSv.yr$^{-1}$.

**Keywords**: Bottled mineral waters, Liquid Scintillation Counting (LSC), gross alpha and gross beta activity concentrations, annual effective dose.

## I. INTRODUCTION

Natural mineral waters contain large amounts of minerals: magnesium, calcium and sodium and, because they are often extracted from very deep aquifers, they show higher loads of natural radionuclides leached from the surrounding bedrock [1]. The natural radioactivity in water is in direct relation to the geological nature of the land they cross, the contact time (water age), the temperature, the solubility of the elements encountered, etc. The levels of all radionuclides emitting alpha or beta radiation, in drinking mineral water may be assessed by measurement of the gross alpha and gross beta activities. These total activity measurements can be made quickly and cost-effectively, and detailed isotope analysis is only required if the maximum acceptable values of the total activities are exceeded [2].

The increasing use of bottled mineral water in Morocco, especially for children of lactation age, makes it necessary to consider it as an important element for human life. The presence of high level of radioactivity in drinking water sources provides potential health dangers for the population. Hence, it is important to assess the levels of gross alpha and gross beta activity in water sources to ensure the safety of water. Liquid scintillation counting (LSC) is

one of the most important laboratory methods to determine the radioactivity of low energy radionuclides in liquid sample especially water.

## II. GROSS ALPHA and GROSS BETA ACTIVITY CONCENTRATIONS

To monitor the radioactivity of bottled mineral waters sold in the Moroccan market we use the Moroccan norm ISO 11704. The Moroccan norm is a Method of determining of gross alpha and beta activity in drinking water, is based on international standards. Monitoring gross alpha and beta activity include all forms of water samples with a dry residue less than $5g.L^{-1}$. According to the Moroccan norm, the maximum allowed value is $0.1 \ Bq.L^{-1}$ for gross alpha activity and $1 \ Bq.L^{-1}$ for gross beta activity. 13 brands of bottled natural mineral waters most consumed in Morocco were purchased and brought to the laboratory. Seven of them are produced locally through the exploitation of spring and underground waters across the country, while six are imported brands from France, Spain and Italy. The ISO 11704:2018 method was used in this work for determining gross alpha and gross beta activities in bottled drinking waters using thermal pre-concentration and Liquid Scintillation Counting (LSC). LSC has become in recent years a reference method for radiological assessment of drinking waters in several countries since it provides relatively high sensitivity, simple sample preparation and lower counting time and costs [3]. The radionuclides of concern are generally nonvolatile below 80°C. Some gaseous or volatile radionuclides, such as radon, will not be detected by standard gross activity. The pretreatment of the samples is carried out by measuring these three factors: the dry residue the pH and the conductivity. The TDS were determined in all samples by evaporation to dryness and weighting the residue, Table 1.

TABLE 1
THE RESULT OF GROSS ALPHA AND BETA ACTIVITY CONCENTRATIONS OBTAINED FOR 13 BOTTLED MINERAL WATER SAMPLES

| Sample | TDS (mg.L$^{-1}$) | pH | Conductivity($\mu$S.cm$^{-1}$) |
|---|---|---|---|
| **1** | 397 | 7.881 | 590 |
| **2** | 186 | 7.988 | 266 |
| 3 | 435 | 7.686 | 626 |
| 4 | 249 | 7.937 | 292 |
| 5 | 480 | 7.707 | 634 |
| 6 | 186 | 6.915 | 284 |
| 7 | 2078 | 7.327 | 2020 |
| 8 | 345 | 7.514 | 539 |
| 9 | 1084 | 7.605 | 1096 |
| 10 | 429 | 7.400 | 225 |
| **11** | 141 | 7.998 | 612 |
| **12** | 167 | 8.259 | 180 |
| **13** | 345 | 7.114 | 470 |

TDS: Total dissolved solids.

Gross alpha and gross beta activity concentrations exhibited significant variabilities among samples (Table 2). In fact, the gross alpha and gross beta activities remain low, with a slight increase in the gross alpha activities compared to the gross beta activities. For the samples 5 and 11, a little high in the gross beta activity compared to the gross alpha activities for the samples 1, 2, 4, 6, 8, 12 and 13 and below the detection limits for the other samples (3, 7, 9 and 10). The gross alpha and gross beta activity concentrations show low variability between samples ranging from 0.060 to 0.132 $Bq.L^{-1}$ for gross alpha and 0.087 to 0.151 $Bq.L^{-1}$ for gross beta activities.

TABLE 2
GROSS ALPHA AND GROSS BETA ACTIVITY CONCENTRATIONS FOR 13 ANALYZED BOTTLED MINERAL WATERS.

| Sample | $A_\alpha$Tot (Bq.L$^1$) | $\Delta(A_\alpha$Tot) | $A_\beta$Tot(Bq.L$^1$) | $\Delta(A_\beta$Tot) |
|---|---|---|---|---|
| 1 | < 0.038 | --- | < 0.054 | --- |
| 2 | < 0.027 | --- | 0.088 | 0.008 |
| 3 | < 0.062 | --- | < 0.089 | --- |
| 4 | 0.060 | 0.012 | 0.096 | 0.014 |
| 5 | 0.132 | 0.017 | < 0.103 | --- |
| 6 | < 0.078 | --- | 0.151 | 0.008 |
| 7 | < 0.461 | --- | < 0.661 | --- |
| 8 | 0.070 | 0.014 | 0.098 | 0.015 |
| 9 | < 0.208 | --- | < 0.298 | --- |
| 10 | < 0.059 | --- | < 0.085 | --- |
| 11 | 0.063 | 0.013 | < 0.085 | --- |
| 12 | < 0.051 | --- | 0.087 | 0.016 |
| 13 | < 0.053 | --- | 0.089 | 0.027 |

$A_{\alpha Tot}$ and $A_{\beta Tot}$: Gross alpha and gross beta activity concentrations, $\Delta$: their incertitude at 1-σ.

## ANNUAL EFFECTIVE DOSE due to the INGESTION

The calculation of the annual effective dose due to the ingestion of mineral water is based on taking into account the most pessimistic prediction in which the overall alpha and beta activities are assumed to come from the radionuclides $^{210}$Po and $^{228}$Ra, because these radionuclides have the highest effective dose coefficients. Thus, the calculation formula to evaluate the annual effective dose (DEA) is as follows [4-5]:

$$DEA = [A_\alpha * CF(^{210}Po) + A_\beta * CF(^{228}Ra)] \times R.$$

$A_\alpha$: the overall alpha activity (Bq.L$^{-1}$), $A_\beta$: the overall beta activity (Bq.L$^{-1}$), R: the rate of annual consumption.

The following table (table 3) shows the results of the annual effective dose of 13 water samples.

TABLE 3
THE ANNUAL EFFECTIVE DOSE DUE TO THE INGESTION OF RADIONUCLIDES IN MINERAL FOR ADULT, CHILD AND INFANT.

| Samples | Adult Dose (mSv.yr$^{-1}$) | Child Dose (mSv.yr$^{-1}$) | Infant Dose (mSv.yr$^{-1}$) | Inference |
|---|---|---|---|---|
| 1 | < DL | < DL | < DL | safe |
| 2 | 0.04 | 0.02 | 0.01 | safe |
| 3 | < DL | < DL | < DL | safe |
| 4 | **0.10** | 0.05 | 0.03 | safe |
| 5 | **0.12** | 0.06 | 0.03 | safe |
| 6 | 0.07 | 0.04 | 0.02 | safe |
| 7 | < DL | < DL | < DL | safe |
| 8 | **0.11** | 0.06 | 0.03 | safe |
| 9 | < DL | < DL | < DL | safe |
| 10 | < DL | < DL | < DL | safe |
| 11 | 0.06 | 0.03 | 0.01 | safe |
| 12 | 0.04 | 0.02 | 0.01 | safe |
| 13 | 0.04 | 0.02 | 0.01 | safe |

DL: Detection Limit

10 water samples dose results were lower than the WHO recommended value, which is 0.1 mSv.y$^{-1}$. However, the samples 4,5 and 8 were equal to this value.

While the results indicate that the majority of the water samples meet the quality standard with respect to annual effective dose, continued monitoring is essential to ensure that water quality remains within acceptable safety limits.

## CONCLUSION

This study utilized the Moroccan norm method to determine measurement of the gross alpha and gross beta activity concentrations of 13 commercially bottled mineral waters obtained from Moroccan markets through Liquid Scintillation Counting (LSC).Gross alpha and gross beta activity concentrations were all below the World Health Organization's recommended values for drinking water quality. The values have been found to lie between minimum <LLD and maximum $0.211\pm0.015$ and $0.151\pm0.008$ Bq.L$^{-1}$ respectively. The annual effective dose due to the ingestion of radionuclides in mineral water and based on total alpha and total beta activities for adults, child and infant shows a respect with the total indicative dose set at 0.1 mSv.yr$^{-1}$. The studied bottled mineral water samples are acceptable for consumption and these comply with WHO recommendations for drinking water.

However, continued commitment to monitoring mineral water is necessary to meet public health standards regarding potential radiological risks associated with its consumption. This practice helps identify any deviations from safety thresholds and allows for timely intervention to maintain water quality at levels that pose minimal risks to consumers.

## ACKNOWLEDGEMENT

## REFERENCES

[1]  G. Wallner, T. Jabbar, "*Natural radionuclides in Austrian bottled mineral waters*". J Radioanal Nucl Chem. 2010, 286,329–334.

[2]  Ministry of Health. *Guidelines for Drinking-water Quality Management for New Zealand*. 2013. Third edition. 729 p.

[3]  M. Palomo, M. Villa, N. Casacuberta, A. Peñalver, F. Borrull, C. Aguilar, "*Evaluation of different parameters affecting the liquid scintillation spectrometry measurement of gross alpha and beta index in water samples*". Appl. Radiat. Isot. 2011,69, 1274–1281.

[4]  O.O. Galadima, M.D. Ayagi, R. Rebecca, U. Rilwan, M.A. Dauda, "*Analysis and Assessment of Gross Alpha and Beta in Drinking Water of Some Selected Areas of Gashua, Yobe State, Nigeria*" . The Journal of Advances in Theoretical & Computational Physics, 2022. 5, 3 p.

[5]  O.J. Okunola , M.O.A. Oladipo, T. Aker , O.B. Popoola, "*Risk assessment of drinkable water sources using gross alpha and beta radioactivity levels and heavy metals*". The Journal of Heliyon 2020. 6, 4 p.

[6]  E. Botezatu, O. Iacob, A. Aflorei, G. Elisei, O. Căpitanu, "*Natural radioactivity of some mineral waters and population doses*". The Journal of Preventive Medicine 2001,9(3), 3-14.

[7]  S. Sarvajayakesavalu, D. Lakshminarayanan, J. George, S.B. Magesh, K.M. Anilkumar, G.M. Brammanandhan, A. Chandrasekara, M. Ravikumar, "*Geographic Information System mapping of gross alpha/beta activity concentrations in ground water samples from Karnataka, India: a preliminary study*". Groundwater for Sustainable Development, 2018, 6, 164-168.

[8]  H.V. Duong, H.L. Le, D.T. Nguyen, N.M. Vu, T.H. Duong, M. Hegedűs, A. Peka, T. Kovács, "*Gross alpha/beta activity concentrations in spa and mineral waters in North Vietnam*". Journal of Radioanalytical and Nuclear Chemistry, 2020, 326, 1511–1517.

[9]  ISO 9696. *Water quality: measurement of gross alpha activity in non-saline water—thick source method*. International Organization for Standardization, Geneva 8. 2007.

[10] ISO 9697. *Water quality: measurement of gross beta activity in non-saline water*. International Organization for Standardization, Geneva 9. 2008.

[11] ISO 10704. *Water quality: measurement of gross alpha and gross beta activity in non-saline water—thin source deposit method*. International Organization for Standardization, Geneva. 2009.

[12] ISO 10704, 2009. *Water quality: measurement of gross alpha and gross beta activity in non-saline water-thin source deposit method*. International Organization for Standardization, Geneva.

[13] UNSCEAR. *United Nations Committee on the Effects of Atomic Radiation, Sources and Effects of Ionizing Radiation*. Report to the General Assembly with Scientific Annexes, Annex B. United Nations: New York, NY, USA, 2008; Volume 1.

[14] WHO. World Health Organization, guidelines for drinking water quality. Volume 1: Recommendations, 3rd Edition 1st Addendum to vol. 1, Geneva. 2006.

Conférence Internationale sur l'Ingénierie de l'Environnement et l'Ecologie (IEE-2024)
Proceedings of Engineering & Technology-PET-Vol 89

# Effects of litter size and age on plasma glucose and total proteins of lactating goat living in arid environment

Kamilia Henna[1, 2,*], Arezki Kheddache[3, 2], Yamina Zatra[4, 2], Zaina Amirat[2], Farida Khammar[2], Salima Charallah, [2]

[1]*Department of Biology, Faculty of Sciences - University of M'hamed Bougara Boumerdes (FS UMBB) (INIM), Boumerdes 35000*
[2]*Department of Biology and Physiology of Organisms, Faculty of Biological Sciences, University of Sciences and Technology Houari Boumediene (USTHB), BP 32 El-Alia, Algiers, Algeria*
[3]*Department of Biology, Faculty of Biological Sciences and Agronomic Sciences, Mouloud Mammeri University, 15000 Tizi-Ouzou, Algeria*
[4]*Department of Biology, Faculty of Nature and Life Sciences, University of Blida 1, 09000, Algeria*

*  k.henna@univ-boumerdes.dz
   hennakamilia@gmail.com

*Abstract*— **Saharan goats are among the indigenous breeds raised in the Algerian Sahara  desert.  Several ecophysiological and metabolic studies have shown the physiological characteristics of this breed allowing it to survive in the extreme conditions of arid climates. Several studies have also shown in goats that litter size and age of the lactating female affect energy metabolism biomolecules such as glucose (GLU) and total proteins (TP). The purpose of this study is to demonstrate the effect of litter size and age on the plasma level of GLU and TP. Blood samples were taken from the jugular vein at 8:00 a.m. before feed intake in young ( 2 years aged, n=11), old (6 to 8 years aged, n=3), single litter (n=11) and double litter (n=3) goats reared at the Béni Abbès research station (30 ° 07 'N., 2 ° 10' O.), located in southwest Algeria. The plasma determination of GLU and TP is carried out by a direct enzymatic colorimetric method. The statistical tests used are Student's t and Mann-Whitney in GraphPad Prism. The results show that the glycaemia of goats aged 6 to 8 years and that of double litters is higher (P >0.05) than that of goats aged 2 years and that at single litter. While, the mean proteinemia of young and old goats is not significantly different (P>0.05). Similarly, mean proteinemia of single and double litter goats is not significantly different (P<0.05). Furthermore, this study deserves to be supplemented by the dosage of thyroid hormones and estrogens to better clarify the endogenous determinism of these variations.**

*Keywords*— **Age, Glucose, Total proteins, Litter size, Lactation, Saharan Goat**

## I. INTRODUCTION

Indigenous goats play a crucial role in arid agricultural zones where the Saharan populations depend on them for livelihood. Several ecophysiological and metabolic studies have demonstrated their adaptive physiological characteristics to arid areas. Indeed, in these animals, the reduction of water  turnover  and glomerular filtration rates is observed [1], and high levels of placental pregnancy-associated glycoproteins are produced,  which maintain gestation [2]. Furthermore, blood metabolic profile is used to predict the emergence of some metabolic disorders, energy metabolism, and nutritional and health status in animals [3]. The indicators of BMP are mainly the hematochemical parameters, which are influenced by various factors, such as breed, age [4], gender [5], season [6] and reproductive status [7].
Recently,  the influence of age and litter size on metabolic status of lactating multiparous goats was investigated [8, 9]. However, there is a lack of information concerning the data of hematochemical parameters during lactation period in the Saharan breed. This study was designed to determine the impact of age and litter size on GLU and TP secretions in our breed.

## II. MATERIALS AND METHODS

### A. ETHICAL APPROVAL

The animal experiment was approved by the Ethical Committee of the Algerian Higher Education and Scientific Research (Executive Decrees No. 04-82 and No. 10-90) and agreed by the Algerian Association of Sciences in Animal Experimentation (AASEA, agreement number 45/DGLPAG/DVA.SDA.14) of the University of Science and Technology HouariBoumediene, of Algiers.

### B. ANIMALS AND MANAGEMENT

Fourteen healthy multiparous goats (*Capra hircus*), 2-8 years old, weighing 19.6±4.03 kg, were used. Animals were kept in the sheepfold of the Béni-Abbès experimental station located in the Algerian Sahara Desert (30°07′N., 2°10′W.; elevation 497 m). The cli-mate of this region is classified among the hottest anddriest in Algeria, where ambient temperature can reach 47°C in the summer. The annual rainfall recorded is 18 mm in autumn and winter. During the breeding sea- son (autumn), the females were naturally mated with a fertile buck; in the spring, all pregnant goats gave birth to 16 kids, including seven males and nine females. The dams were also healthy from any mammary gland infections (mastitis and udder edema) and incidences of metabolic disorders, such as milk fever, displacement of the abomasum, fatty liver syndrome, and ketosis. The kids permanently stayed with their mothers and were weaned at the age of 3 months. The dams were fed twice daily with a ration of 0.6 kg/ goat of forage cereals and 0.6 kg/goat of barley supplemented with dates and *Aristida pungens* (known in Arabic as "drinn") throughout the experimental periodand green alfalfa during the first postpartum (PP) days. Water and stones to lick were available *ad libitum.*

### C. BLOOD SAMPLING AND BIOCHEMICAL ASSAYS

Blood samples were collected from the external jugular vein at 08:00 a.m. before feeding. All animals were sampled weekly for 12 weeks of lactation. The blood samples were stored in lithium heparin for glucose (GLU) and total protein (TP) assays. The samples were centrifuged at 3000×g for 15 min at 4°C. The decanted sera and plasma were stored in Eppendorf microtubes at −20°C until analysis.

The serum metabolites were analyzed using an automated clinical chemistry analyzer (Bio  lis 24i Premium Tokyo Boeki Medisys Inc. Japan) and a spectrophotometer. Bioassay kits (Biomaghreb, Tunisia) were used to assess GLU, Plasma TPs were measured using an auto analyzer (Pentra C200. Horiba, France) and a commercial kit (ABX Pentra TP CP, France). Enzymatic colorimetric methods were used to assess plasma GLU and TP.

## III. RESULTS AND DISCUSSION

### A. EFFECTS OF LITTER SIZE AND AGE ON SERUM GLUCOSE

The results show that the glycaemia of goats aged 6 to 8 years and that of double litters is higher  than  that of goats aged 2 years ($3.17 \pm 0.25$ vs $3.00 \pm 0.08$ mmol/L; $P > 0.05$) and that at single litter ($3.31 \pm 0.33$ vs $2.99 \pm 0.08$ mmol/L) (Fig.1). This can be explained by the fact that young goats have to cover their nutritional needs for growth, maintenance and lactation, whereas old goats which have completed their development, including that of the mammary gland, use their energy only for provide maintenance and lactation functions [10,11]. Similarly, glycaemia is higher in goats with double litters than in those with single litters; indicating a higher energy demand in twin goats during this period to ensure fetal growth [12, 13].
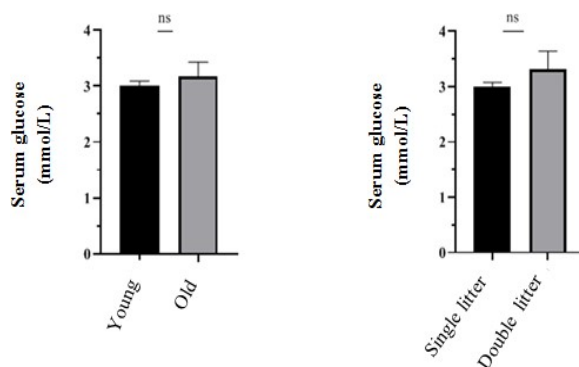


Fig. 1 Effects of litter size and age on plasma glucose of lactating  goat

*B. EFFECTS OF LITTER SIZE AND AGE ON PLASMA TOTAL PROTEINS*

The mean proteinemia of young and old goats is not significantly different ($51.72 \pm 0.56$ g/L *vs* $51.31 \pm 1.17$ g/L, $P>0.05$, respectively). Similarly, mean proteinemia of single and double litter goats is not significantly different ($51.80 \pm 0.44$ *vs* $50.68 \pm 2.58$ g/L, respectively, $P<0.05$) (Fig.2).
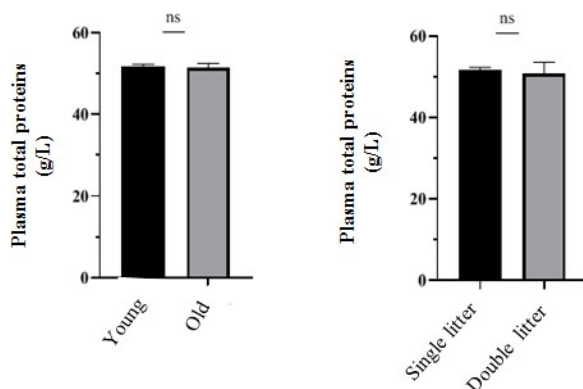


Fig. 2 Effects of litter size and age on plasma total proteins of lactating goat

## VI. CONCLUSION

This study showed that lactation period is critical physiological stages because most metabolic changes occur during this period. Therefore, through our results, circulating metabolic parameters will help breeders and veterinarians for the best management of reproduction to improve production in indigenous Saharan goats. Furthermore, this study deserves to be supplemented by the dosage of thyroid hormones and estrogens to better clarify the endogenous determinism of these variations.

## ACKNOWLEDGMENTS

## REFERENCES

*[1]* N. Silanikove, "Renal excretion of urea in response to changes in nitrogen intake in desert (black Bedouin) and non-desert (Swiss Saanen) goats". *Comp. Biochem. Physiol.A Comp. Physiol.*, Vol. 79(4), pp. 651-654. 1984

[2] S. Charallah, Z. Amirat, J. Sulon, F. Khammar, and J.F. Beckers, "Pregnancy-associated glycoprotein and progesterone concentrations during pregnancy failure in Bedouin goat from the Southwest of Algeria". *Reprod. Domest. Anim.*, Vol. 45(6). pp. 231-238. 2010

[3] Z. Antunović, J. Novoselec, H. Sauerwein, M. Speranda, M. Vegara, and V. Pavic, "Blood metabolic profile and some of hormones concentration in ewes during different physiological status". *Bulg. J. Agric. Sci.*, Vol. 17(5), pp. 687-695. 2011

[4] Z. Antunović, K. Novaković, Ž. Klir, V. Šerić, B Mioč, M. Šperanda, M. Ronta, and J. Novoselec, "Blood metabolic profile and acid-base status of Istrian goats a critically endangered Croatian goat in relation to age". *Vet. Arhiv*, Vol. 90(1), pp. 27-38. 2020

[5] B. Habibu, M. Kawu, T. Aluwong, and H. Makun, "Influence of seasonal changes on physiological variables, haematology and serum thyroid hormones profile in male Red Sokoto and Sahel goats". *J. Appl. Anim. Res.*, Vol. 45(1), pp. 508-516. 2017

[6] N.L. Ribeiro, R. Germano-Costa, E.C. Pimenta-Filho, M.N. Ribeiro, and R. Bozzi, "Effects of the dry and the rainy season on endocrine and physiologic profiles of goats in the Brazilian semi-arid region". *Ital. J. Anim. Sci.*, Vol. 17(2), pp. 454-461. 2018

[7] J. Madan, S.Sindhu, and M.K. Rose, "Changes in plasma biochemical parameters and hormones during transition period in Beetal goats carrying single and twin fetus".*Vet. World.*, Vol. 13(6), pp. 1025-1029. 2020

[8] L. L. Souza, E. G. Moura, and P. C. Lisboa, "Litter size reduction as a model of overfeeding during lactation and its consequences for the development of metabolic diseases in the offspring". *Nutrients*, Vol. 14(10), pp. 2045. 2022

[9] J. L. P. Xavier, D. X. Scomparin, C. C. Pontes, P. R. Ribeiro, M. M. Cordeiro, J. A. Marcondes, and S. Grassiolli, "Litter size reduction induces metabolic and histological adjustments in dams throughout lactation with early effects on offspring". *An Acad Bras Cienc.*, Vol. *91*, pp. e20170971. 2019

[10] A. Boudebza, N. Arzour-Lakhel, M.C. Abdeldjelil, A.L. Dib. N. Lakhdara, H. Benazzouz, and C. Benlatreche, "Blood biochemical parameters in Ouled Djellal ewes in the periparturient period". *Der. Pharma. Chemica.*, Vol. 8 (18), pp. 406-410. 2016

[11] R. Cepeda-Palacios, M.G. Fuente-Gómez, J.M. Ramírez-Orduña, A. García-Álvarez, X. Llinas-Cervantes, and C. Angulo, "Effects of pregnancy and post-kidding stages on haematochemical parameters in cross-bred goats." *J. Appl. Anim. Res.*, Vol. 46 (1), pp. 269-273. 2018

[12] M.S. El-Tarabany, T.M. Abdel-Hamid, O.A. Ahmed-Farid, K.M .Al-Marakby, "Characterization of progesterone profile, physiological responses, milk composition and blood biochemical and hematological indices at the early stage of lactation in goats". *Biol. Rhythm Res.*, Vol. 50 (4), pp. 647-657. 2019

[13] Z. Antunović, K. Novaković, Ž. Klir, V. Šerić, B. Mioč, M. Šperanda, M. Ronta, J. Novoselec, "Blood metabolic profile and acid-base status of Istrian goats a critically endangered Croatian goat in relation to age". *Vet. Arhiv.*, Vol. 90 (1), pp. 27-38. 2020

# Biogas production from textile waste

Ibtissem Hraiech [#1], Sihem Belkhiria [#1], Abdelmajid Jemni[#1]

*# Laboratory of Studies of Thermal Systems and Energy, University of Monastir*

*LR99ES31, 5019, Monastir, Tunisia*

`ibtissemhraiech@gmail.com-Sihem_belkhiria@yahoo.fr-abdelmajid.jemni@enim.rnu.tn`

*Abstract*—**An examination of the procedure for fermenting textile waste to create biogas is provided in this study. Therefore, it is essential to study the various fermentation process reactions as well as the various factors affecting the anaerobic digester's performance in order to assess a methanization unit producing biogas. A paste and liquid sludge mixture was put into the digester. The study showed that, over the course of 21 days, textile sludge can produce biogas by mesophilic fermentation at a maximum pressure of 2 bar.**

*Keywords*— **Fermentation – biogas – Digester – Textile waste – Pressure**

## I. INTRODUCTION

An inventive method of waste management and the creation of renewable energy is the biogas production from textile waste. Textile waste can include a wealth of organic materials that are appropriate for anaerobic digestion, a process that turns organic matter into biogas. This includes scraps, damaged fabrics, and end-of-life clothing.

The role of wastewater treatment plants is to eliminate the pollution contained in domestic effluents, before their release into the natural environment. If the water, at the end of treatment, is effectively purified, the initial pollution is partly stored and concentrated in the sludge resulting from the various stages of water treatment. This sludge is then considered as recoverable waste, which must be eliminated while respecting certain regulatory constraints.

The production of sludge is increasingly difficult to manage. This pushes governments to seek technological solutions to reduce it in the same way as the management of other types of waste.

One of the effective and less expensive technologies allowing the treatment of the organic fraction of this waste is anaerobic digestion (bio-methanization), which consists of a biological degradation, in the absence of oxygen, of the organic matter into a mixture of methane (CH4) and carbon dioxide (CO2) called `biogas'. Thanks to anaerobic digestion, waste becomes a source of wealth. This technology becomes essential in the process of reducing waste volumes and producing biogas, which is a renewable energy source that can be used in the production of electricity and heat.

Alternatives to manage the polluting potential include strategies to reduce textile waste and extend product life, such as renting and mending clothing, the second-hand market, and reprocessing processes for the creation of new or original items [1]. Fast fashion, on the other hand, has advanced along a business model that creates enormous quantities of apparel and trends at low prices [2], frequently with poor quality. Due to their poor quality, textiles can only be used for energy recovery, which is at the bottom of the waste management hierarchy, as specified by Directive 2008/98/EC [3].

Anaerobic digestion (AD) is a widely used biotechnology that has shown to be an efficient green waste management solution by lowering the risk of contamination and generating biogas, which is used as electricity. Using AD in the textile sector can help with water reuse and waste use as a resource for sustainable energy production. However, if AD is used as the only strategy, the variety of chemicals, organic pollutants, and recalcitrant compounds (such as polyacrylates, phosphonates, alkyl phenol ethoxylates, chloroform, heavy metals, and cotton-based recalcitrant material [4]) present difficulties and lower the degradation efficiency [5].

According to a number of studies, applying pretreatments can help enhance the degradability of organic matter while also increasing the yield of biogas [5,6,7,8] and removing harmful chemicals and colors from wastewater and solid waste in aqueous solutions [9, 5]. The chemical composition of the waste affects the effectiveness of pretreatments, which can be chemical, physical, biological, or mixtures of these [10].

Physical pretreatments, such as heat, mechanical force, irradiation, and ultrasound, cause cell disruption [11]. As a result, by decreasing the particle size, the organic matter's contact surface is enhanced, which makes microbial

attack easier [12]. Physical pretreatments are advantageous because no hazardous compounds are produced, but some methods (such as heat) can raise energy expenditures to the point where they are not practical on a wide scale [12]. Chemical pretreatments, such as acid, alkali, and organic solvents, work by rupturing chemical bonds in intricate structures, which causes the cell to inflate internally and increase its surface area [13].

Chemical methods are more frequently used than biological and physical pretreatments because they are extremely effective in breaking down complicated materials [13]. However, they need to be handled carefully because harmful compounds may arise depending on the chemical reagents used. Certain chemical pretreatments, like nitric acid (HNO3), hydrochloric acid (HCl), and sulfuric acid (H2SO4), can cause metal to corrode and fail, further damaging operational equipment [14,15,16].14, 15, and 16. Enzymes, fungus, bacteria, microbial consortia, and other biological pretreatments work in concert with microbial metabolism to hasten the breakdown of organic materials [12]. Wu et al. [18] numerically examined a 3-dimensional model of biogas production. The model is based on the principles of conservation of mass, energy, species transport and chemical reactions. The simulation results showed that biogas production is sensitive to variation in the concentration of organic matter and fermentation time. Jurgensen et al. [19] proposed a dynamic approach for improving biogas production. The numerical model used is a statistical model for single reactor technology. The simulation results showed good agreement with the experimental studies. Lubken et al. [20] modeled the energy balance of anaerobic digestion for the case of livestock manure. The simulation method is hard ADM1 base. The simulation results made it possible to calculate the production of biogas and methane as well as the energy produced. Using a pilot-scale reactor, the authors demonstrated the usefulness of using the dynamic energy balance model. Gebremedhin et al. [21] presented a numerical model based on the principles of energy conservation. This model is used to calculate the daily, monthly and annular energy demand during the fermentation process. Hill [22] presented a numerical model for the analysis of the kinetics of methane fermentation. The model is based on two criteria: the maximum volumetric methane productivity or the maximum daily methane production. Indeed, the concentration of volatile solids, the fermentation time and temperature are the main factors in determining the maximum daily methane production. Sokolenko et al. [23] studied the evolution of energy during the fermentation process in the liquid and gas phase. The results showed that the concentration of carbon dioxide increases in the mass transfer phase and decreases upon reaching the saturation pressure of the liquid phase.

Opwis et al. [24] developed an innovative technology for the production of energy from textile wastewater. The results showed that the proposed semi-industrial system produces a large amount of biogas. Rajendran et al. [25] studied the economic and experimental evaluation of a new biogas digester. The influential materials used are municipal solid waste. The results showed that the proposed domestic digester has economic and environmental benefits. Control parameters such as temperature, pressure, sludge concentration, climatic parameters and mechanical agitation are the factors to be optimized. Indeed, Guo et al. [26] developed a digital thermal model to investigate optimal temperature and organic matter conditions. Galanakis et al. [27] studied the effect of pressure and temperature during the fermentation process. The results showed the sizing of the bioreactor is limited by the hydrostatic pressure.

Preventing the introduction and production of toxic chemicals encourages the development of an ecologically sound AD system. Additionally, even at full scale, the application of biological approaches is highly attractive due to the reduced energy and capital costs when compared to physical and chemical pretreatments [15, 17].

To boost the production of biogas, prior research has involved pretreating waste textiles that contain high crystalline cellulose and cellulosic blend fibers in a batch assay [28], [29]. Furthermore, two-stage testing procedures were never used on textile wastes.

During the anaerobic digestion process, only part of the organic matter is completely degraded, the rest is an excellent fertilizing agent for agricultural land. Waste textiles, which are primarily made of cotton and viscose fibers, have a large potential for producing various biofuels, including biogas, because of their cellulose content [30].

As part of this research project, the process of anaerobic digestion of activated sludge from the textile wastewater treatment plant for biogas production was considered. This is an applied research partnership between our research laboratory (LESTE) and the Société Industrielle de Textile SITEX. The recovery of textile waste contributes on the one hand to preserving the environment and on the other hand to producing ecological, green and sustainable energy.

This study presents an analysis of the process of fermenting textile waste to produce biogas. Thus, to assess a methanization unit producing biogas, one must research the various fermentation process reactions as well as the various factors influencing the anaerobic digester's performance [31, 32]. Through the concentrations of various

reagents and products, the numerical model tracks the evolution of the reactions that occur, allowing us to examine the effects of various biological control parameters and system performance.

## II. EXPERIMENTAL DEVICE

In this study we are interested in a mesophilic methanisation in an anerobic digester. Thus, mesophilic methanization means that the digester is maintained at a temperature approximately equivalent to that of the human body: between 35 and 40°C. This is the most widespread operation, whether for agricultural or industrial installations. Among the advantages of mesophilic fermentation, we can cite:

* Optimal temperature: Mesophilic bacteria thrive at moderate temperatures, usually between 20°C and 45°C. This temperature range is easier to maintain in fermentation reactors, reducing energy costs associated with heating or cooling.

*Flexibility of the substrate: Mesophilic bacteria can tolerate a greater variety of organic substrates. This implies that they can produce biogas by fermenting a range of organic materials, including food waste, yard waste, and textile waste.

*Fermentation Speed: Bacteria that are thermophilic (which grow best at higher temperatures) typically grow at a slower rate than mesophilic bacteria. This typically translates to shorter retention periods in fermentation reactors, enabling the generation of biogas more quickly.

*Lower maintenance costs: Fermentation systems employing mesophilic bacteria can often require less maintenance and be easier to manage than those using thermophilic bacteria because of their lower operating temperature and tolerance to a wider variety of substrates.

Anaerobic digestion is a complex process. The principle is as follows: organic waste is stored in a cylindrical and airtight tank called a "digester" or "methanizer" in which it is subjected to the action of micro-organisms (bacteria) in the absence of oxygen, the digester used is shown in this figure: it is a cylindrical stainless steel digester with a radius R = 45 cm and a height of 60 cm. A digester made up of two coaxial cylindrical enclosures is proposed. The sludge will be placed in the inner cylinder. To ensure its homogenization, an agitator is installed. It is driven by an electric motor with a power of approximately 2.2 kW. À It eliminates any type of decantation at the bottom of the digester. The free space between the two coaxial cylinders serves as a bath filled with hot water, the temperature of which is controlled by a thermostatically controlled bath. A pressure sensor installed inside the digester installed on an acquisition card and a microcomputer allowing the monitoring of the gas pressure generated during the fermentation reaction. The temperature control is done by installing two thermocouples inside the digester and near its wall,


Fig. 1 Experimental device

Thus, a mixture of paste sludge (75 kg) and liquid was placed in the inner cylinder of the anaerobic digester (Figure 2).

Fig 2 textile sludge liquid (a) and paste (b)

To prevent textile sludge from decantation, an electric motor-powered agitator is put inside the digester. A pressure sensor (0 bar -16 bar) was installed inside the digester to control the pressure of the gas generated during the fermentation process. Two thermocouples were installed, one inside the digester and the other near the wall, to control the temperature. These sensors are installed on an acquisition card connected to a microcomputer, allowing the temporal evolution of pressure and temperature to be visualized.

## III. EXPERIMENTAL STEPS

Anaerobic fermentation can be used to produce biogas from textile waste, both in liquid and paste form. Despite not being thought of as a source of substrate for biogas production, textiles frequently contain organic materials that, in anaerobic environments, can be broken down by microorganisms to produce biogas. This is how it might function:

*Textile waste needs to be pretreated before it can be used in anaerobic fermentation. This applies to waste that is liquid (such as wastewater from dyeing or washing operations) or paste (such as rags and unusable clothing). In order to improve the specific surface area and make it easier for microorganisms to access the substrates, this may entail grinding, fragmentation, or other pretreatment techniques.

*Microorganism inoculation: The textile waste that has been pretreated is subsequently put into an anaerobic fermentation reactor. To start the fermentation process, cultures of mesophilic bacteria or other anaerobic microorganisms are added to the reactor.

*Anaerobic fermentation: The organic matter in textile waste is broken down by microorganisms in a fermentation reactor. Volatile fatty acids, alcohols, and other intermediate products can be produced from the polymers of cellulose, lignin, and other organic compounds found in textiles. Anaerobic microorganisms then break these compounds down into biogas, primarily methane ($CH_4$) and carbon dioxide ($CO_2$).

*Biogas production and utilization: The fermentation reactor's waste product, biogas, is collected and can be used to generate fuel, electricity, or heat. Additionally, it can be refined to create biomethane of a commercial grade that can be introduced into the natural gas grid.
Residue Management: After fermentation, the remaining fermented residue, often called digestate, can be used as a fertilizer or amendment for agricultural soils due to its high nutrient content.

## IV. MATHEMATICAL MODEL

The biological reactions involved in methanization are complex but overall we can identify three main stages: hydrolysis and acidogenesis: the complex organic chains (proteins, lipids, polysaccharides) are transformed into

simpler compounds (fatty acids, peptides, amino acids); acetogenesis: the products of acidogenesis are converted into acetic acid; methanogenesis: acetic acid is transformed into methane and carbon dioxide,

We employed the COMSOL 5.6 software to examine the fermentation processes occurring in the digester. The following is a list of the two fundamental chemical reactions that constitute methanogenesis:

$C_2H_4O_2 => CO_2 + CH_4$      (eq. 1)

$CO_2 + 4H_2 => 2H_2O + CH_4$      (eq. 2)

Mass transfer equation: to evaluate the different concentrations of reagents and products during methanization we used the Arrhenius law:

$$K^f = A^f \left(\frac{T}{T_{ref}}\right)^{nf} \exp\left(-\frac{E^f}{R_g T}\right) \quad \text{(eq. 3)}$$

Where:

Af: direct frequency factor

nf: direct temperature exponent

Ef: direct activation energy

Tref =1 K

## V. NUMERICAL RESULTS

COMSOL 5.6 was used to examine the fermentation process occurring in the digester.

This figure 3 illustrates variation in molar concentration of different constituents of textile sludge during the fermentation reaction. It should be emphasized that the amount of biogas generated mainly depends on the amount of organic matter present, in particular the amount of acetic acid.
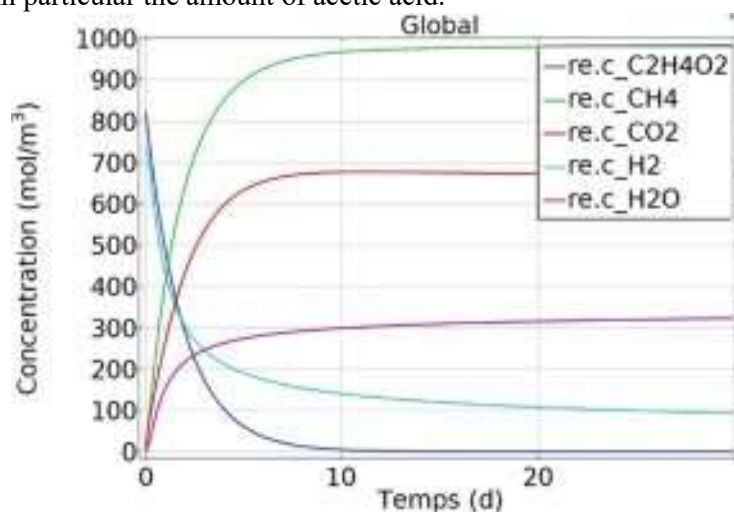


Fig 3 Molar concentration of reactants and products of textile sludge fermentation

The amount of biogas generated mainly depends on the amount of organic matter present, particularly the amount of acid.

The results of the heat balance for mesophilic (35 °C) conditions are shown in Figure 4. This figure shows that 88% of the total heat required was used to compensate for heat losses through the digester's walls (Qd) and raise the sludge's temperature to that of the digester (Qi). In actuality, heat transfer through the digester walls loses 63% of the total heat required for digestion (Qd ). Therefore, to guarantee the digester's best performance, thermal insulation needs to be applied to its walls. It should be mentioned that the amount of heat needed depends on the outside temperature of the digester as well.

In fact, when the temperature difference between the digester's interior and exterior decreases, Qd and Qi values also decrease, thereby lowering the overall heat requirement. Thus, another 33 kJ is obtained.
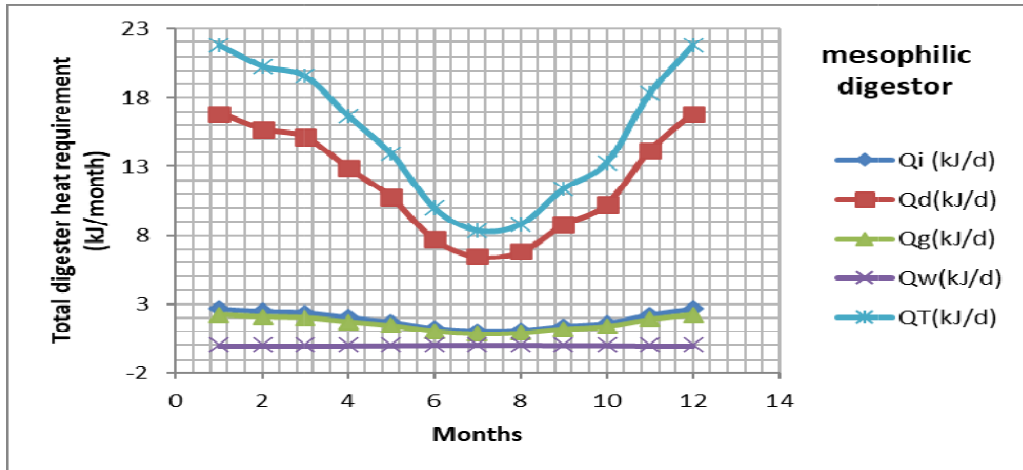
Fig 4 Evolution of the monthly heat balance during the mesophilic fermentation process

With:

Qi: heat loss inside the digester

Qd: heat loss near the wall

HQ: heat loss during gas extraction

Qw: heat loss during evaporation

QT: total heat loss

Thermal insulation must therefore be applied to the walls of the digester to guarantee optimal operation.

## VI. EXPERIMENTAL RESULTS

- Temperature control

Many processes in a variety of industries, such as the production of biogas, chemicals, food, and pharmaceuticals, depend heavily on temperature control. Strict adherence to temperature requirements guarantees process effectiveness, safety, and high-quality products.

Temperature plays an essential role since methanogenic bacteria are particularly sensitive to temperature variations. The fermentation process should be carried out with a maximum variation of $\pm 1°C$.
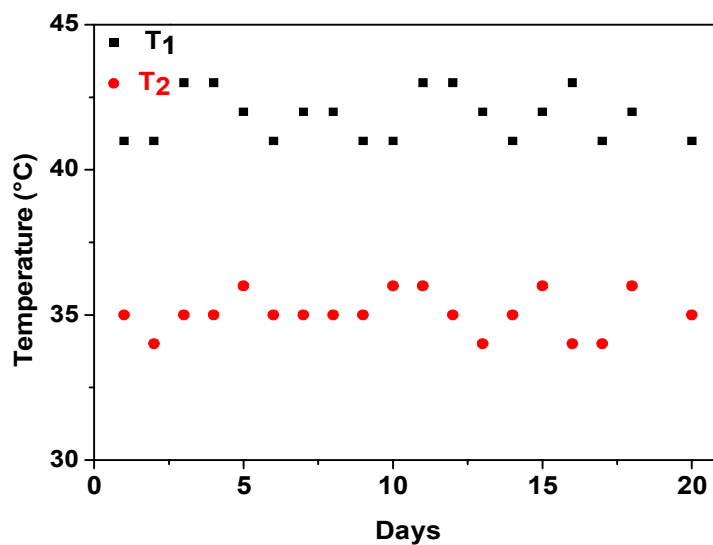


Fig 5 Temperature control

The internal temperature is practically uniform (35°C -36°C), it is a mesophilic fermentation characterized by a moderate temperature.

- Pressure sensor calibration

Let's now move on to the presentation of some experimental results. We must start with the calibration of the pressure sensor to ensure the accuracy and reliability of the measurements, calibration of pressure sensors is an essential step in ensuring accurate and dependable pressure sensor measurements: calibration generally consists of applying known pressures and comparing the output values display by the quad (voltage) to the corresponding input values. Adjustments are made until the output exactly matches the input. The adjustment curve is shown in Figure 6.
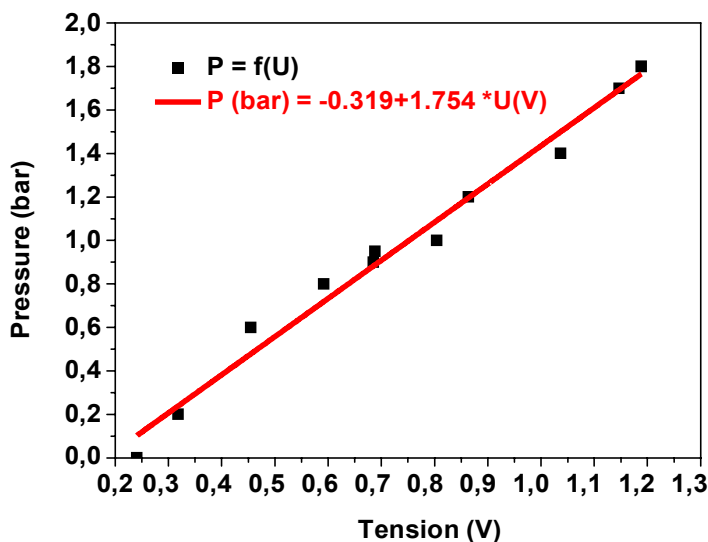


Fig 6 Pressure sensor calibration curve

- Daily production of gas pressure

The quantity of gas produced or the pressure level sustained within a particular system over a 24-hour period is referred to as the daily production of gas pressure. In many industries, such as manufacturing, utilities, and oil and gas, measuring daily gas production or pressure is essential because it affects production processes, safety, and efficiency.

The daily evolution of the pressure inside the digester is shown schematically in figure 7.

The variation in pressure tells us directly about the quantity of biogas produced and subsequently its concentration, We notice that the production of biogas begins from the 7th day with slow kinetics.
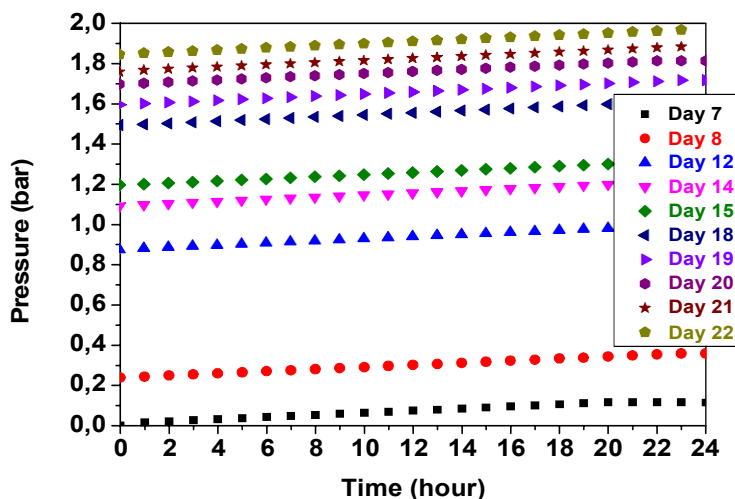


Fig 7 Gas pressure produced during fermentation for each day

- Biogas production kinetics

The study of the rate at which biogas is produced during anaerobic digestion is known as "biogas production kinetics." This process is usually represented mathematically, with key factors influencing gas production over time being described in relation to one another. Anaerobic digestion process optimization, gas yield prediction, and the design of effective biogas production systems all depend on an understanding of the kinetics of biogas production. Biogas production kinetics are shown in Figure 8.
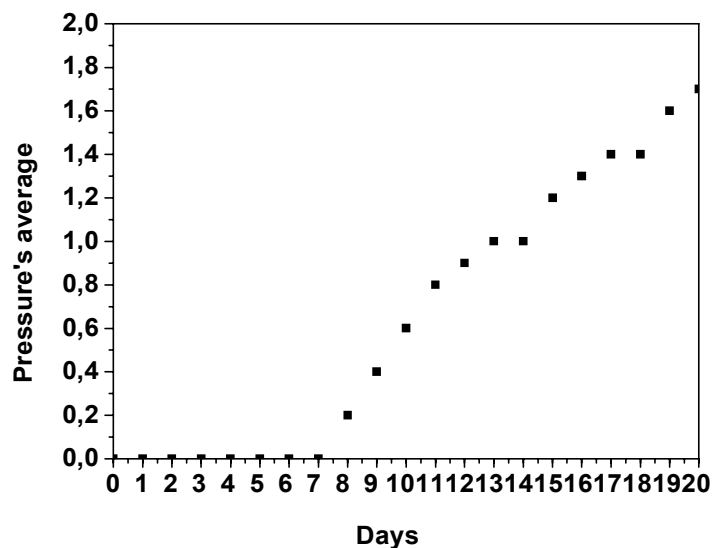


Fig 8. Biogas production kinetics

## VII. CONCLUSIONS

A study of the fermentation of textile sludge for biogas production in an anaerobic digester was carried out: a mixture of liquid sludge and paste was introduced into the digester. Although biogas production from textile waste can present specific challenges due to the nature of the materials, it also offers an opportunity for waste valorization and renewable energy production from unconventional sources.

This article looks at the numerical simulation of textile wastewater's anaerobic fermentation process. The outcomes demonstrated that spontaneous fermentation reactions can occur in a direct manner in ambient temperature.

The results showed that textile sludge is capable of producing biogas via mesophilic fermentation with a maximum pressure of 2 bar during a stay of 21 days.

The evolution of the biogas concentration during mesophilic fermentation shows that the quantity of biodegradable organic matter in the sludge affects the volume of biogas produced as well as the fermentation time required.

The evolution of the internal pressure of the digester is proportional to the quantity of biogas generated.

## REFERENCES

[1]    1.Piribauer, B.; Bartl, A. Textile Recycling Processes, State of the Art and Current Developments: A Mini Review. Waste Manag. Res. J. A Sustain. Circ. Econ. 2019, 37, 112–119. [Google Scholar] [CrossRef] [PubMed]
[2]    Niinimäki, K.; Peters, G.; Dahlbo, H.; Perry, P.; Rissanen, T.; Gwilt, A. The Environmental Price of Fast Fashion. Nat. Rev. Earth Environ. 2020, 1, 189–200. [Google Scholar] [CrossRef] [Green Version]
[3]    European Parliament, Council. Directive 2008/98/EC of the European and of the Council of 19 November 2008 on Waste and Repealing Directives. 2008. Available online: http://www.fao.org/faolex/results/details/es/c/LEX-FAOC083580/ (accessed on 24 April 2021).
[4]    Chen, Y.; Cheng, J.J.; Creamer, K.S. Inhibition of Anaerobic Digestion Process: A Review. Bioresour. Technol. 2008, 99, 4044–4064. [Google Scholar] [CrossRef] [PubMed]

[5]   Apollo, S.; Onyango, M.S.; Ochieng, A. Integrated UV Photodegradation and Anaerobic Digestion of Textile Dye for Efficient Biogas Production Using Zeolite. Chem. Eng. J. 2014, 245, 241–247. [Google Scholar] [CrossRef]

[6]   Gonzalez, A.; Hendriks, A.T.W.M.; van Lier, J.B.; de Kreuk, M. Pre-Treatments to Enhance the Biodegradability of Waste Activated Sludge: Elucidating the Rate Limiting Step. Biotechnol. Adv. 2018, 36, 1434–1469. [Google Scholar] [CrossRef] [Green Version]

[7]   Chen, L.; Qin, Y.; Chen, B.; Wu, C.; Zheng, S.; Chen, R.; Yang, S.; Yang, L.; Liu, Z. Enhancing Degradation and Biogas Production during Anaerobic Digestion of Food Waste Using Alkali Pretreatment. Environ. Res. 2020, 188, 109743. [Google Scholar] [CrossRef]

[8]   Anacleto, T.M.; Oliveira, H.R.; Diniz, V.L.; de Oliveira, V.P.; Abreu, F.; Enrich-Prast, A. Boosting Manure Biogas Production with the Application of Pretreatments: A Meta-Analysis. J. Clean. Prod. 2022, 362, 132292. [Google Scholar] [CrossRef]

[9]   Prabakar, D.; Manimudi, V.T.; Mathimani, T.; Kumar, G.; Rene, E.R.; Pugazhendhi, A. Pretreatment Technologies for Industrial Effluents: Critical Review on Bioenergy Production and Environmental Concerns. J. Environ. Manag. 2018, 218, 165–180. [Google Scholar] [CrossRef]

[10]  Mustafa, A.M.; Poulsen, T.G.; Xia, Y.; Sheng, K. Combinations of Fungal and Milling Pretreatments for Enhancing Rice Straw Biogas Production during Solid-State Anaerobic Digestion. Bioresour. Technol. 2017, 224, 174–182. [Google Scholar] [CrossRef] [PubMed]

[11]  Orlando, M.Q.; Borja, V.M. Pretreatment of Animal Manure Biomass to Improve Biogas Production: A Review. Energies 2020, 13, 3573. [Google Scholar] [CrossRef]

[12]  Abraham, A.; Mathew, A.K.; Park, H.; Choi, O.; Sindhu, R.; Parameswaran, B.; Pandey, A.; Park, J.H.; Sang, B.I. Pretreatment Strategies for Enhanced Biogas Production from Lignocellulosic Biomass. Bioresour. Technol. 2020, 301, 122725. [Google Scholar] [CrossRef] [PubMed]

[13]  Amin, F.R.; Khalid, H.; Zhang, H.; Rahman, S.; Zhang, R.; Liu, G.; Chen, C. Pretreatment Methods of Lignocellulosic Biomass for Anaerobic Digestion. AMB Express 2017, 7, 72. [Google Scholar] [CrossRef] [Green Version]

[14]  Pellera, F.M.; Santori, S.; Pomi, R.; Polettini, A.; Gidarakos, E. Effect of Alkaline Pretreatment on Anaerobic Digestion of Olive Mill Solid Waste. Waste Manag. 2016, 58, 160–168. [Google Scholar] [CrossRef]

[15]  Thompson, T.M.; Young, B.R.; Baroutian, S. Advances in the Pretreatment of Brown Macroalgae for Biogas Production. Fuel Process. Technol. 2019, 195, 106151. [Google Scholar] [CrossRef]

[16]  Montgomery, L.F.R.; Bochmann, G. Pretreatment of Feedstock for Enhanced Biogas Production. IEA Bioenergy 2014. Available online: https://www.ieabioenergy.com/wp-content/uploads/2014/02/pretreatment_web.pdf (accessed on 13 November 2021).

[17]  Brémond, U.; de Buyer, R.; Steyer, J.P.; Bernet, N.; Carrere, H. Biological Pretreatments of Biomass for Improving Biogas Production: An Overview from Lab Scale to Full-Scale. Renew. Sustain. Energy Rev. 2018, 90, 583–604. [Google Scholar] [CrossRef]

[18]  B. Wu, E.L. Bibeau et K.G. Gebremedhin, Three-dimensional numerical simulation model of biogas production for anaerobic digesters, CANADIAN BIOSYSTEMS ENGINEERING, volume 51, 2009.

[19]  L. Jürgensen, E. A. Ehimen, J. Born et J. B. Holm-Nielsen, Dynamic biogas upgrading based on the Sabatier process: Thermodynamic and dynamic process simulation, Bioresource Technology, pages, 2014.

[20]  M. Lubken, M. Wichern, M. Schlattmann, A. Gronauer et H. Horn, Modelling the energy balance of an anaerobic digester fed with cattle manure and renewable energy crops, WATER RESEARCH, volume 4, pages 4085 – 4096, 2007.

[21]  K. G. Gebremedhin, Biogas Production Model for Plug-Flow Anaerobic Digesters, ASABE Annual International Meeting, 2006.

[22]  D. T. Hill et C. L. Barth, A Dynamic Model for Simulation of Animal Waste Digestion, Water Pollution Control Federation, volume 49, pages 2129-2143, 1977.

[23]  A. Sokolenko, O. Shevchenko, I. Maksymenko, K. Vasylkivskyi, Energy transformations in processes of anaerobic fermentation, Ukrainian Food Journal, volume 7, pages 273-280, 2018.

[24]  K. Opwis, T. Mayer-Gall, J. S Gutmann, C. Dammer, T. Titscher, A. Nickisch-Hartfiel, O. Grün, C. Spurk, C. Schloderer, A. Köppe, C. Dörfler et H. Bachus, Semi-industrial production of methane from textile wastewaters, Energy, Sustainability and Society, volume 2, pages 1-6, 2012.

[25]  K. Rajendran, S. Aslanzadeh, F. Johansson et M. J. Taherzadeh, Experimental and economical evaluation of a novel biogas digester, Energy Conversion and Management, volume 74, pages 183–191, 2013.

[26]  J. Guo, R. Dong, J. Clemens et W. Wang, Thermal modelling of the completely stirred anaerobic reactor treating pig manure at low range of mesophilic conditions, Journal of Environmental Management, volume 127, pages 18-22, 2013.

[27]  C. M. Galanakis, C. Kordulis, M. Kanellaki, A.A. Koutinas, A. Bekatorou et A. Lycourghiotis, Effect of pressure and temperature on alcoholic fermentation by Saccharomyces cerevisiae immobilized on c-alumina pellets, Bioresource Technology, volume 114, pages 492–498, 2012.

[28]  A. Jeihanipour, K. Karimi, C. Niklasson, M.J. Taherzadeh,A novel process for ethanol or biogas production from cellulose in blended-fibers waste textiles Waste Management, 30 (2010), pp. 2504-2509

[29]  A. Jeihanipour, K. Karimi, M.J. Taherzadeh,Enhancement of ethanol and biogas production from high-crystalline cellulose by different modes of NMO pretreatment,Biotechnology and Bioengineering, 105 (2010), pp. 469-476

[30]  K. Rajendran, G. Balasubramanian;High rate biogas production from waste textiles.School of Engineering, University of Borås, Borås (2011)

[31]  López-Jiménez, P.A., Escudero-González, J., Martínez, T.M., Montanana, V.F., Gualtieri, C.: Application of CFD methods to an anaerobic digester: the case of Ontinyent WWTP, Valencia, Spain. J. Water Process Eng. 7, 131–140 (2015).

[32]  Wu, B., Bibeau, E.L.: Development of 3-D anaerobic digester heat transfer model for cold weather applications. Trans. ASABE 49, 749–757 (2006).